POLITECNICO DI MILANO

Scuola di Ingegneria Industriale e dell'Informazione

Corso di Laurea Magistrale in
Ingegneria Matematica

Modular Energies for Crystal Elasto-Plasticity and

Structural Phase Transformations

Relatore: Prof. Paolo Biscari (Politecnico di Milano)

Correlatore: Prof. Giovanni Zanzotto (Università di Padova)

Tesi di Laurea di:

Clara Patriarca Matr. 883651

Politecnico di Milano:
www.polimi.it

Scuola di Ingegneria Industriale e dell'Informazione:
www.ingindinf.polimi.it

Contents

List of Figures

Sommario

Lo scopo di questo lavoro è proporre un modello di potenziali elastici di deformazione per cristalli bidimensionali con l'obiettivo di prevedere fenomeni elastoplastici così come trasformazioni di fase martensitica sia di tipo ricostruttivo che distorsivo. In particolare, poichè l'effetto memoria di forma si manifesta nell'ambito delle trasformazioni di fase di quest'ultimo tipo, uno dei modelli proposti è adatto a predirne l'insorgere.
Sono proposti modelli di tipo variazionale non lineare di energie di deformazione invarianti rispetto all'azione del gruppo di simmetria globale $GL(2,\mathbb{Z})$. Queste funzioni sono concepite tramite la teoria classica delle forme modulari sul semipiano di Poincaré, che appare come l'ambiente più opportuno dove costruire densità di energia che esibiscano l'invarianza tipica dei reticoli cristallini bidimensionali. Il lavoro si conclude con la validazione numerica di tali modelli teorici tramite l'implementazione di un codice a elementi finiti.

Abstract

The purpose of this work is modelling a class of strain energy functions for two-dimensional crystals in order to predict elasto-plasticity phenomena together with martensitc phase transitions both of the reconstructive and weak type, with the particular intention of forecasting the manifestation of shape-memory effect. It proposes nonlinear variational models consisting of strain energies invariant under the global symmetry group $GL(2,\mathbb{Z})$. These functions are conceived by exploiting the classical theory of modular forms on the Poincaré half-plane, which appears as a the suitable framework to construct energy densities exhibiting the correct invariance of two-dimensional lattices. Finally, the work comprehends the numerical validation of the theoretical proposals through the implementation of a finite-elements code.

Introduction

Crystalline solids provide an archetypal example of how microscopic symmetry may influence and even determine the material response of macroscopic systems. The ordered richness of their microstructure can be transparently represented by a lattice and it enables the material to display bizarre phenomena as the shape-memory effect or superelasticity. Both these effects exhibit in the context of martensitic phase tranformations. Theselatter are solid to solid transformations which imply cooling the crystal down from some high temperature very rapidly. The abrupt change in temperature prevents the atoms to diffuse and allows for a new distorted microstructure to generate.

Martensitic phase tranformations can be reversible under certain hypotheses; in this case the new martensite microstructure disappears upon reheating and the inital austenite phase is recovered. Reversibility is precisely what connotes the behavior of Nitinol as other smart alloys which preserve the memory of their original underformed shape and retrieve it when suitably heated. These alloys are known as shape-memory alloys (SMA).

Figure 1 on page 3 schematically illustrates the response of these alloys upon temperature variations and deformation. The material is initially in the austenite phase (a); as it is cooled, the phase transformation happens and austenite turns into martensite (b). However this tranformation occurs with no macroscopic change in shape. Such a distinctive event, which takes the name of *self-accommodation*, finds explanation in the crystallographic symmetry differences of the lattices underlying the two phases. Since, by defintion, austenite phase has a greater symmetry than martensite phase, during the transformation it encounters the possibility to transmute into multiple *symmetry-related variants* of martensite. Different regions of the crystal tranform to different variants; the coherent mixture of the variants precisely allows for the absence of a net change in shape. The material then reacts to the following deformation by rearranging the variants and preserving their symmetry rather than distorting the lattice. Indeed, as the variants are symmetry-related they have the same strain energy (this concept will be clarified in the first chapter) while distorsion would imply an energy cost. As a further consequence we also obtain that when the load is released the confuguration (c) is preserved as it did not imply any change in energy from (b). Finally, there being a unique variant of austenite, each variant of martensite transforms back to austenite upon reheating and the original initial configuration in (a) is recovered as if the material drew directly from the memory shielded during the process.

Most shape-memory alloys manifest the ability to recover large strains also under isothermal conditions; this phenomenon is known as superelasticity or pseudoelas-

ticity. Figure 2 on the next page displays the associated stress-strain hysteresis due to the loading-unloading process. The material is now completely in its austenitic state as the temperature is kept constant above the martensitic transformation value. When a mechanical load is applied, the material initially undertakes an elastic behavior (segment OA) until it appereantly yields and undergoes a large deformation (AB). However, we must speak about apparent yield because the segment AB in fact represents a process of tranformation from austenite to *stress-induced martensite*, which is triggered when reaching a critical load. After a certain amount of deformation, the material recovers an elastic behavior (segment BC), which coincides with the elastic response of the now-martensite phase. At last, after releasing the load, the martensite phase being unstable at the considered temperature the deformation is completely reabsorbed.
On the other hand, irreversible martensitic phase tranformations imply abandoning elasticity and exploring the plastic domain, which characterizes the more common industrial process of *quenching* exploited to harden steel for instance.
The difference in reversibility can be explained in light of the simmetry properties of the lattice underlying the crystalline material. In a reversible tranformation the symmetry group of the initial austenitic phase and the final martensitic phase are included in a common finite symmetry group; this implies a symmetry-breaking process which takes the name of *weak* martensitic phase tranformation. This group-subgroup relation allows to restrict the domain of the energy of the transformation to a neighbourhood of the reference configuration. This neighbourhood does not contain arbitrarly large deformations, hence the tranformation occurs with no plasticity.
When this hypothesis does not hold we label the transformation as *reconstructive*: we cannot single out a similar neighbourhood hence the material experiences unbounded distorsions which create defects in the lattice that make the transformation irreversible.
In this thesis we investigate the modelling of martensitic phase transformations both of the weak and reconstructive type through general classes of strain-energy functions obeying the symmetries of the two-dimensional crystal lattices. These functions are conceived within the framework of the classical theory of modular forms on the Poincaré half-plane.
The germ of this approach is due to Parry (1998). On the one hand he devised an injection between the strain space and the Poincaré half-plane, which fully warrants the use of this space as the domain of the strain energy functions. Furthermore, the Dedekind Tessellation of this domain proves to be a limpid representation of the constraints imposed by the symmetry of two-dimensional lattices on the energy landscape.
On the other hand, he first suggests exploiting modular functions in order to construct a class of strain energies obeying these constraints. The most representative among modular functions is the *Klein's Invariant J*, which after some manipulations emerges as to be the essential building brick to conceive proper potentials. Even though Parry conceived the original and blooming intuition, the final explicit expressions of the energies were never provided.
This thesis adopts the mentioned approach by retracing the necessary manipulations to obtain an explicit class of strain energy functions characterized in such a manner;

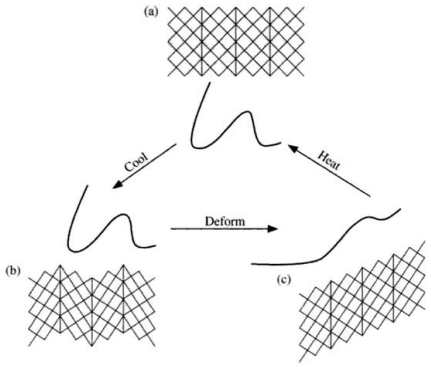

Figure 1: The shape-memory effect. Here an exemplifying piece of wire in Nitinol recovers the deformation to which it was subjected while cold upon reheating. In (a) it is represented the initial austenite phase. In (b) we can observe the multiple symmetry-related variants of martensite that rearrange after the deformation (c). No net change in shape has occurred between (a) and (b). Taken from Battacharaya (2004)

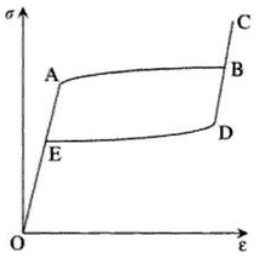

Figure 2: The superelastic stress-strain curve. Taken from Battacharaya (2004)

this path was mainly travelled by E.Arbib in his Master's Thesis "Modular order parameters in non linear elasticity" (2016). The main purpose of our work is to exploit this class of functions in order to model martensitic phase transformations. We present the precise outline of the work in the following lines.

Outline

The thesis follows this structure:

In the first chapter we retrace the theoretical path to obtain a general class of energy densities exhibiting the correct invariance of two dimensional lattices. This path was defined in the work done by E. Arbib in his Master's Thesis "Modular order parameters in non linear elasticity" (2016).

In the second chapter we exhibit and analyze an explicit expression of a strain-energy function modelling reconstructive martensitic phase transformations. This chapter together with the third one represents the original theoretical contribution of this work.

In the third chapter we tackle the modelling of weak martensitic phase tranformations. In particular, we propose an explicit expression of an energy density devised to predict shape-memory effect and superelastic behavior.

In the fourth chapter we discuss the results of the numerical analysis on the potential devised in the second chapter. In particular, we explore the predictions of this model on the behavior of a two-dimensional crystalline body undergoing plastic deformations. This chapter contains the original numerical results of the work.

Chapter 1

Modular order parameters in non Linear crystal elasticity

In this chapter we mainly travel through the work done up to the present around the possibility of exploiting modular forms in order to devise strain energy functions. Parry (1998) first proposes this strategy, after suitably identifying the strains space with the Poincaré half-plane $\mathcal{H}$. His thought and line of research are used by E. Arbib in his Master's thesis "Modular order parameters in non linear elasticity" (2016). His work represents the point of departure of this work, by rendering a general class of strain energy functions for planar crystals. These potentials are devised through the classical theory of modular forms on the Poincaré half-plane, which provides a complete conceptual framework to obtain energy densities exhibiting the correct invariance of two-dimensional lattices. This thesis' work spontaneously stems from that of Arbib with the intent to exploit this class of functions in order to model both reconstructive and weak phase tranformations, especially aiming at portraying the behavior of shape-memory alloys.
In the first section we recreate the theoretical skeleton to build such potentials, while the second section discloses the essential steps that finally bring to the explicit forms of the strain energy functions.

1.1 Continuum theory of crystalline solids

This section is devoted to develop a continuum theory of crystalline solids, which demands to contemplate the presence of the realm of lattices at the microscopic level.
Subsection (1.1.1) covers a review of lattices and their symmetry. Then we introduce the classical action of the group $GL(2,\mathbb{Z})$ on the space of lattice metrics, which also provides a classification of planar simple lattices. Afterwards it is given a fundamental domain for this action. Finally, by introducing the "Ericksen-Pitteri Neighborhoods" it is possible to quantitatively differentiate weak and reconstructive martensitic transformations. Some representative examples of phase tranformations are presented in the final part of the subsection.
In subsection (1.1.2) we introduce the link between the lattices and the continumm by using the Cauchy-Born hypothesis, which allows for the formulation of the strain

energy function in terms of the lattice metric. In this subsection we discuss the properties that the energy must satisfy. Finally, it is presented an explicit expression for the volumetric part of the energy.
The whole section draws heavily from the work of Parry (1998), Battacharya (2004), Conti, Zanzotto (2004), Pitteri, Zanzotto (2001) and Arbib (2016).

1.1.1 Crystallography of 2D simple lattices

A 2D simple lattice is an infinite and discrete subset of $\mathbb{R}^2$, given by

$$\mathcal{L}(\mathbf{e}_i) = \left\{\mathbf{x} = v^i\mathbf{e}_i \quad v^i \in \mathbb{Z}, \quad i = 1,2\right\} \tag{1.1}$$

where the sum over repeated indices is understood. The independent vectors $\{\mathbf{e}_1, \mathbf{e}_2\}$ are the lattice basis.
We define the *metric* $\mathbf{C}$ of the lattice basis $\{\mathbf{e}_i\}$ to be the 2×2 symmetric and positive-definite matrix with components

$$C_{ij} = \mathbf{e}_i \cdot \mathbf{e}_j \tag{1.2}$$

where symmetry is a direct consequence of scalar product symmetry while the relation $\|\mathbf{v}\|^2 = \mathbf{v}.\mathbf{C}\mathbf{v}$ where $\mathbf{v} = v_1\mathbf{e}_1 + v_2\mathbf{e}_2$ proves the metric to be positive-definite. All lattice metrics can be collected in the space $\mathrm{Sym}^+(\mathbb{R}^2)$ of positive-definite symmetric 2×2 matrices. $\mathrm{Sym}^+(\mathbb{R}^2)$ is a 3D cone, defined by the conditions $C_{11} > 0$ and $C_{12}^2 < C_{11}C_{22}$, within the space $\mathbb{R}^3$ with coordinates C_{11}, C_{12}, C_{22}.
Given a 2D simple lattice, the basis and the metric that generate it are not uniquely determined. Two bases $\{\mathbf{e}_1, \mathbf{e}_2\}$ and $\{\mathbf{f}_1, \mathbf{f}_2\}$ generate the same lattice if and only if

$$\tilde{\mathbf{e}}_j = m_{ij}\mathbf{e}_i \quad \mathbf{m} = (m_{ij}) \in GL(2,\mathbb{Z}) \tag{1.3}$$

where $GL(2,\mathbb{Z})$ is the group of 2×2 invertible matrices with integral entries and determinant ± 1. Hence $GL(2,\mathbb{Z})$ is the "global symmetry group" of 2D simple lattices, because each lattice determines its bases up to a tranformation in this group. The action (1.3) of this group reflects on the metrics of the associated bases through this relation

$$\tilde{\mathbf{C}} = \mathbf{m}^T\mathbf{C}\mathbf{m} \tag{1.4}$$

Hence (2.4) naturally defines the action of $GL(2,\mathbb{Z})$ on $\mathrm{Sym}^+(\mathbb{R}^2)$.
If $\mathbf{C}$ is the metric associated to the basis $\{\mathbf{e}_i\}$, we can identify the finite subgroup of $GL(2,\mathbb{Z})$ collecting the matrices $\mathbf{m}$ which leave the metric invariant under the action (1.4)

$$\begin{aligned} L(\mathbf{e}_i) = &\{\mathbf{m} \in GL(2,\mathbb{Z}) : m_{ij}\mathbf{e}_i = \mathbf{Q}\mathbf{e}_j, \mathbf{Q} \in \mathcal{O}(2)\} \\ &\left\{\mathbf{m} \in GL(2,\mathbb{Z}) : \mathbf{C} = \mathbf{m}^T\mathbf{C}\mathbf{m}\right\} = L(\mathbf{C}). \end{aligned} \tag{1.5}$$

$L(\mathbf{e}_i)$ is called "lattice group" or "arithmetic holohedry" and it gives the integral representation of the elements of the point-group symmetry of the corresponding lattice. This latter is the set of rotations that map the lattice back to itself.
The change of basis (1.3) for the same lattice transforms the lattice group through the conjugacy relation in $GL(2,\mathbb{Z})$:

$$L(m_{ji}\mathbf{e}_j) = \mathbf{m}^{-1}L(\mathbf{e}_i)\,\mathbf{m} \quad \forall \mathbf{m} \in GL(2,\mathbb{Z}). \tag{1.6}$$

Therefore a given lattice $\mathcal{L}(\mathbf{e}_i)$ determines an entire conjugacy class of lattice groups in $GL(2,\mathbb{Z})$. Furthermore, an orthogonal transformation does not change the lattice group:

$$L(\mathbf{Q}\mathbf{e}_i) = L(\mathbf{e}_i) \quad \text{if} \quad \mathbf{Q} \in \mathcal{O}(2). \tag{1.7}$$

In light of (1.5) and (1.6) we can define a classification criterium for 2D simple lattices: two lattices $\mathcal{L}(\mathbf{e}_i)$ and $\mathcal{L}(\mathbf{e}'_i)$ are said to have the same "Bravais type" if

$$L(\mathbf{e}'_i) = \mathbf{m}^{-1} L(\mathbf{e}_i)\mathbf{m} \quad \text{for some} \quad \mathbf{m} \in GL(2,\mathbb{Z}) \tag{1.8}$$

i.e. they are associated to the same conjugacy class in $GL(2,\mathbb{Z})$. Analogously, we can subdivide the cone $\mathrm{Sym}^+(\mathbb{R}^2)$ of lattice metrics. A classical result in 2D yields five Bravais types in $\mathrm{Sym}^+(\mathbb{R}^2)$ denominated *oblique, rectangular, rhombic, hexagonal* and*square*.
Through the notion of a lattice group, we can give a precise definition of reconstructive tranformations. The definition of weak tranformations will be discussed later because it requires further notions. Consider a linear map T that defines a tranformation of a lattice $\mathcal{L}(\mathbf{e}_i)$ onto the lattice $\mathcal{L}(\mathbf{f}_i)$, whose basis vectors is $\mathbf{f}_i = T\mathbf{e}_i$. The tranformation T is said to be reconstructive when the group generated by the union of the lattice groups of the initial and final bases, i.e. $L(\mathbf{e}_i) \cup L(\mathbf{f}_i)$, in $GL(2,\mathbb{Z})$ is infinite. Notice that this definition does not depend on the choice of the lattice basis, because the basis change also reflects on the target lattice: $\tilde{\mathbf{e}}_j = m_{ij}\mathbf{e}_i$ is mapped by T onto $\tilde{\mathbf{f}}_j = m_{ij}\mathbf{f}_i$. Then each of the lattice groups change by conjugacy by (1.6). Hence the cardinality of the generated group is still infinity:

$$L(\tilde{\mathbf{e}}_i) \cup L(\tilde{\mathbf{f}}_i) = \mathbf{m}^{-1}\left(L(\mathbf{e}_i) \cup L(\mathbf{f}_i)\right)\mathbf{m} \tag{1.9}$$

We now define a *fundamental domain* for the action (1.4) to be a subset of $\mathrm{Sym}^+(\mathbb{R}^2)$ such that each $GL(2,\mathbb{Z})$ orbit (that is, each Bravais lattice) in $\mathrm{Sym}^+(\mathbb{R}^2)$ has one and only one element in that subset. A simply connected fundamental domain in 2D is given by

$$\mathcal{D} = \left\{ \mathbf{C} \in \mathrm{Sym}^+(\mathbb{R}^2), \quad 0 < C_{11} \le C_{22}, \quad 0 \le C_{12} \le \frac{C_{11}}{2} \right\}. \tag{1.10}$$

The fundamental domain $\mathcal{D}$ is subdivided into six connected subsets, which are obtained for five lattice types (see Fig. 1.1 on the following page and Fig. 1.2 on page 9). Indeed, the rhombic lattice type is itself partitioned into two connected subparts, one for "skinny" rhombi where one between the two diagonals is shorther than the side and one for "fat" rhombi whose diagonals are both longer than the side. The fundamental domain $\mathcal{D}$ together with its symmetry-related copies $\mathbf{m}^T\mathcal{D}\mathbf{m}$, where $\mathbf{m} \in GL(2,\mathbb{Z})$, upholster the entire space $\mathrm{Sym}^+(\mathbb{R}^2)$.

We now want to properly define weak tranformations, as we did for reconstructive tranformations. The action (1.4) of the group $GL(2,\mathbb{Z})$ on the space of lattice metrics $\mathrm{Sym}^+(\mathbb{R}^2)$ describes the global symmetry of planar lattices. This group includes both rotations and large shears comparable to plastic deformation and slip. However, alloys tipically exhibiting the shape-memory effect show very little

Crystal system (International Symbol)	Lattice type (International Symbol)	Fixed set	Lattice group (up to inversion)
oblique (2)	oblique ($p2$)	$0 < C_{11} < C_{22}$ $0 < C_{12} < \frac{C_{11}}{2}$	$\begin{pmatrix} 1 & 0 \\ 0 & 1 \end{pmatrix}$
rectangular ($2mm$)	rectangular ($p2mm$)	$0 < C_{11} < C_{22}$ $C_{12} = 0$	$\begin{pmatrix} 1 & 0 \\ 0 & 1 \end{pmatrix}, \begin{pmatrix} -1 & 0 \\ 0 & 1 \end{pmatrix}$
	rhombic or centered–rectangular ($c2mm$)	Fixed set I $0 < C_{11} = C_{22}$ $0 < C_{12} < \frac{C_{11}}{2}$	$\begin{pmatrix} 1 & 0 \\ 0 & 1 \end{pmatrix}, \begin{pmatrix} 0 & 1 \\ 1 & 0 \end{pmatrix}$
		Fixed set II $0 < C_{11} < C_{22}$ $0 < C_{12} = \frac{C_{11}}{2}$	$\begin{pmatrix} 1 & 0 \\ 0 & 1 \end{pmatrix}, \begin{pmatrix} 1 & 1 \\ 0 & -1 \end{pmatrix}$
square ($4mm$)	square ($p4mm$)	$0 < C_{11} = C_{22}$ $C_{12} = 0$	$\begin{pmatrix} 1 & 0 \\ 0 & 1 \end{pmatrix}, \begin{pmatrix} 0 & -1 \\ 1 & 0 \end{pmatrix}, \begin{pmatrix} -1 & 0 \\ 0 & 1 \end{pmatrix}, \begin{pmatrix} 0 & 1 \\ 1 & 0 \end{pmatrix}$
hexagonal ($6mm$)	hexagonal ($p6mm$)	$0 < C_{11} = C_{22}$ $0 < C_{12} = \frac{C_{11}}{2}$	$\begin{pmatrix} 1 & 0 \\ 0 & 1 \end{pmatrix}, \begin{pmatrix} 0 & -1 \\ 1 & 1 \end{pmatrix}, \begin{pmatrix} 1 & 1 \\ 1 & 0 \end{pmatrix}, \begin{pmatrix} -1 & 0 \\ 1 & 1 \end{pmatrix}, \begin{pmatrix} 1 & 1 \\ 0 & -1 \end{pmatrix}, \begin{pmatrix} 0 & 1 \\ 1 & 0 \end{pmatrix}$

Figure 1.1: The five Bravais types of 2D simple lattices, their intersection with the fundamental domain $\mathcal{D}$, with the corresponding lattice groups (only one element of the pair $(\mathbf{m}, -\mathbf{m})$ is tabulated). Taken from Conti, Zanzotto (2004).

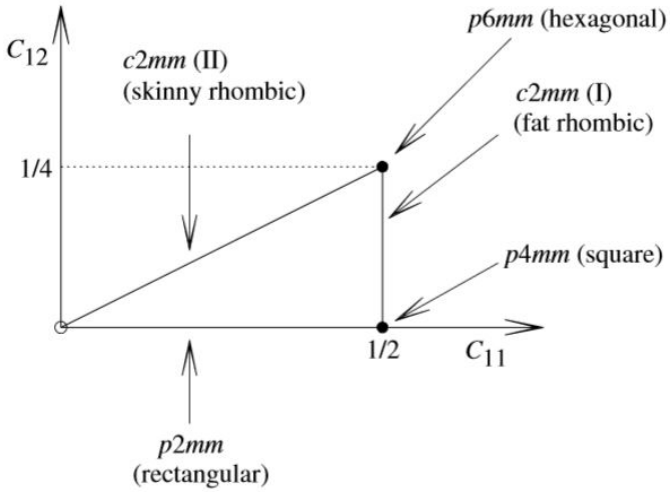

Figure 1.2: The two-dimensional intersection of the fundamental domanin $\mathcal{D}$ in (1.10) with the plane $C_{11} + C_{22} = 1$ (metrics with trace 1), projected on the plane (C_{11}, C_{12}). Taken from Conti, Zanzotto (2004).

plastic deformation and slip. Hence, when modeling weak tranformations, whose a particular manifestation is precisely shape-memory effect, we seek to construct a theory where we consider deformations of the lattice large enough to include elastic deformations, but sufficiently moderate to exclude lattice shears associated with slip and plasticity. Within suitable so-called "Ericksen-Pitteri neighborhoods" (EPNs) in $\mathrm{Sym}^+(\mathbb{R}^2)$ we have to precisely consider action and invariance only by appropriate lattice subgroups of $GL(2,\mathbb{Z})$.
Given any lattice metric $\mathbf{C}_0$, an open neighborhood $\mathcal{N}$ of $\mathbf{C}_0$ in $\mathrm{Sym}^+(\mathbb{R}^2)$ is an EPN if the following properties hold

1. $\forall\, \mathbf{m} \in L(\mathbf{C}_0)$, $\mathbf{C}$ implies $\mathbf{m}^T\mathbf{C}\mathbf{m} \in \mathcal{N}$ or, equivalently, $\mathbf{m}^T\mathcal{N}\mathbf{m} = \mathcal{N}\, \forall\, \mathbf{m} \in L(\mathbf{C}_0)$

2. if for some $\mathbf{m} \in GL(2,\mathbb{Z})$ there is $\mathbf{C} \in \mathcal{N}$ such that $\mathbf{m}^T\mathbf{C}\mathbf{m} \in \mathcal{N}$, then $\mathbf{m} \in L(\mathbf{C}_0)$ or, equivalently, $\mathbf{m}^T\mathcal{N}\mathbf{m} \cap \mathcal{N} = \forall \mathbf{m} \in GL(2,\mathbb{Z}) \setminus L(\mathbf{C}_0)$

Every $\mathbf{C}_0 \in \mathrm{Sym}^+(\mathbb{R}^2)$ has a nonempty EPN. This set includes distorsions that break the symmetry of the lattice: the second property guarantees that, given a EPN $\mathcal{N}_{\mathbf{C}_0}$ associated to the metric $\mathbf{C}_0$, any $\mathbf{C}$ is mapped outside $\mathcal{N}_{\mathbf{C}_0}$ if $\mathbf{m}$ does not belong to $L(\mathbf{C}_0)$. Hence, the symmetry does not increase in $\mathcal{N}_{\mathbf{C}_0}$. Finally, the EPNs allow to formalize the notion of a weak tranformation as a phase change completely taking place within one such neighboord. The metrics of the initial, final, and any intermediate states belong to a single EPN, thus their symmetry groups are all included in the symmetry group of the neighboord's center. In particular shape memory effect requires a further specification, i.e. an austenite whose symmetry is cubic and consequently a martensite whose symmetry is a subgroup of the cubic. However our vocabulary being two-dimensional as well as our context, if we choose the austenite to be represented by a square lattice then the martensite exhibits at

most either a rectangular, rhombic or oblique symmetry.
In order to obtain an explicit criterium to differentiate between reconstructive and weak tranformations, we want to give a quantitative determination of EPNs. We report a result taken from Conti, Zanzotto (2004), which describes the construction of maximal EPNs starting from a given "good enough" fundamental domain. Maximal EPNs are EPNs not strictly contained in any other open EPN.
Given a fundamental domain $\mathcal{D}$ whose boundary as measure zero (as (1.10)) and a fixed metric $\mathbf{C}_0 \in \mathcal{D}$, let

$$\Omega = \left\{ \mathbf{m}^T \mathbf{C}\, \mathbf{m} : \mathbf{m} \in L(\mathbf{C_0}), \mathbf{C} \in \mathcal{D} \right\}. \tag{1.11}$$

Then, the inner part Ω_0 of the set Ω is a maximal EPN of $\mathbf{C_0}$.
Definition (1.11) implies constructing Ω by taking each metric in the fundamental domain and applying to it a tranformation that appears as a rotation when applied to the central metric $\mathbf{C}_0$.
Given this definition, every orbit has at least one representative element in the closure of the maximal EPN Ω_0. This representative element is in general not unique, as each orbit in $\mathrm{Sym}^+(\mathbb{R}^2)$ must have as many elements in an EPN $\mathcal{N}(\mathbf{C}_0)$ as it is dictated by the local symmetry given the lattice group of the central metric $L(\mathbf{C}_0)$. However, not every orbit can have a representative in Ω_0. This is the case, for instance, of the hexagonal lattices orbit when $\mathbf{C}_0$ has a square symmetry: as square and hexagonal metrics have symmetry groups with no finite common supergroup, the hexagonal lattice lies on the boundary of Ω, which is not included in Ω_0.
We now want give some explicit examples of maximal EPNs in 2D, always considering as reference Conti, Zanzotto (2004). In order to do that we represent any $\mathbf{C} \in \mathrm{Sym}^+(\mathbb{R}^2)$ by means of the three coordinates C_{11}, C_{12}, C_{22}, with $C_{ii} > 0, C_{12}^2 < C_{11}C_{22}$. Then, considering only the metrics with trace 1 (i.e. the section of the cone $\mathrm{Sym}^+(\mathbb{R}^2)$ on the plane $C_{11} + C_{22} = 1$, given through coordinates C_{11} and C_{12} ,$0 < C_{11} < 1$ and $|C_{12}| < C_{11}^{1/2}(1 - C_{11})^{1/2}$) amounts to giving each element of $\mathrm{Sym}^+(\mathbb{R}^2)$ up to a rescaling. On this plane, the trace of the fundamental domain $\mathcal{D}$ in (1.10) has a particularly simple form: it is the triangle with vertices $S = (1/2, 0), H^+ = (1/2, 1/4)$ and $(0, 0)$, this latter not being included in $\mathcal{D}$ (see Fig. 1.2 on the preceding page). The trace of $\mathrm{Sym}^+(\mathbb{R}^2)$ on the plane $C_{11} + C_{22} = 1$ is covered by copies of $\mathcal{D}$ by means of the action (1.4)(see Fig. 1.3 on page 12).
Given this representation, we can describe some examples of maximal EPNs on $\mathrm{Sym}^+(\mathbb{R}^2)$. A maximal EPN for the square metric $S = (1/2, 0)$ is the open rhombus centered on S, composed by the four copies of $\mathcal{D}$ obtained through the action of the lattice group $L(S)$ on $\mathcal{D}$; there are two distinct hexagonal metrics on the boundary as Fig. 1.4 on page 12 shows. On the other hand, considering as a central metric $\mathbf{C}_0$ the hexagonal metric $H^+ = (1/2, 1/4)$ a maximal EPN is an open triangle containing six copies of $\mathcal{D}$, with three distinct square metrics on its boundary. For the least symmetrical oblique metric a maximal EPN coincides with the inner part of the appropriate copy of $\mathcal{D}$, as its lattice group contains just the identity tensor; for a rhombic or rectangular metric, a maximal EPN is composed by two copies of $\mathcal{D}$ whose common boundary contains the given metric.

This picture yields the proper theoretical framework to characterize the differences between weak or symmetry-breaking phase tranformations and reconstructive phase tranformations.
Let us consider the instructive exampe of a weak square-to-rhombic transition: this involves the parent square metric $S = (1/2, 0)$ and two product rhombic metrics $R^{\pm} = (1/2, \pm r)$ with $0 < r < 1/4$ where the choices $\pm$ indicate the two rhombic metrics belonging to an EPN of S. These rhombic metrics play the role of two "variants" of martensite that are obtained when rotating the greater symmetry lattice, austenite, through a rotation in its lattice group (in this case $L(S)$) and then tranforming it. In the homogeneous configuration with metric S the basis vectors of the lattice are orthogonal: $r = \mathbf{e}_1 \cdot \mathbf{e}_2 = 0$; when the lattice is tranformed to one of the configurations $R^{\pm}$, the implied distorsion breaks the orthogonality relation $r = 0$, but leaves the basis vectors of equal length. This tranformation is weak precisely because, for not too large r, the metrics involved do not exit from the maximal EPN of S (we speak about "twinning" when the deformation is piecewise homogeneous and it implies generating a configuration involving both the variants $R^{\pm}$). When the system is forced to tranform back to the square phase, which plays the role of austenite, we expect it to go back to the metric S, because moving in the direction of any other square metric is energetically not convenient as these are "far away" from (that is, they are not in any EPN containing) the metrics $S, R^{\pm}$. Hence, there is one and only one variant of austenite. This reasoning is the basis of the mathematical theory which models reversible phase changes, whose manifestation is the shape-memory effect. Shape-memory alloys tipically exhibts twinning planes of martensite crystals in their so-called "self-accomodated" structure, as the literature quoted in the introduction of this chapter extensively explains.
On the other hand, a failure of the assumption about the existence of a unique variant of austenite leads to an infinite variants of both austenite and martensite, as the next example proves. Let us suppose that the homogeneous lattice configuration is tranformed from S to one or both variants $H^{+} = (1/2, \pm r)$, with $r = 1/4$; the strain is in this case so large that the deformed system with metric H^{+} has actually gained full hexagonal symmetry. This is precisely the phenomenology of reconstructive tranformation (which cannot be weak because the metrics $S, H^{\pm}$ cannot all belong to a single EPN). Also in this case there can be twinning and the formation of a microstructure in the tranformed lattice if this latter involves both the variant H^{+} and H^{-}. However, when tranforming back to the square phase, neglecting elastic interations the cells, in the configuration H^{+} have in principle equal chances of going to any of the three neighboring square metrics$S_1 = S = (1/2, 0), S_2 = (1/3, 1/3)$ or $S_3 = (2/3, 1/3)$; likewise for H^{-}. After a tranformation cycling the sample can thus be found to have an underlying lattice corresponding to four square metrics different from S_1. This generates defects which can be either localized (interstitials, vacancies) or long range (dislocations), making the reconstructive phase changes irreversible.
Both tranformations will be explicitely modelled in the next chapters.

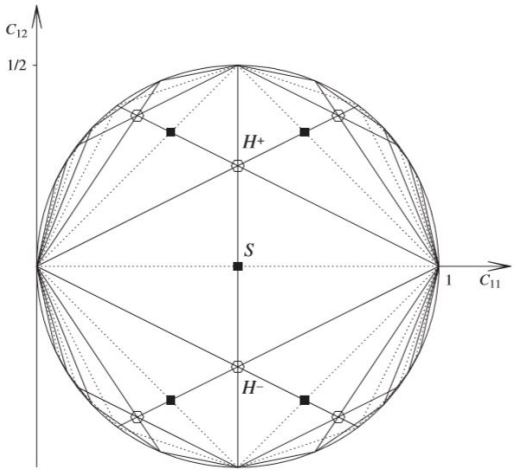

Figure 1.3: Section of the space $\mathrm{Sym}^+(\mathbb{R}^2)$ on the plane $C_{11} + C_{22} = 1$. The $GL(2,\mathbb{Z})$-related copies of $\mathcal{D}$ in Fig. 1.2 on page 9 fill $\mathrm{Sym}^+(\mathbb{R}^2)$. The full squares and empty hexagons indicate a few metrics with square and hexagonal symmetry, respectively. The dotted lines represent the rectangular metrics, the solid lines the rhombic metrics. The dense open set of the other points represents the generic oblique lattice metrics. Taken from Conti, Zanzotto (2004).

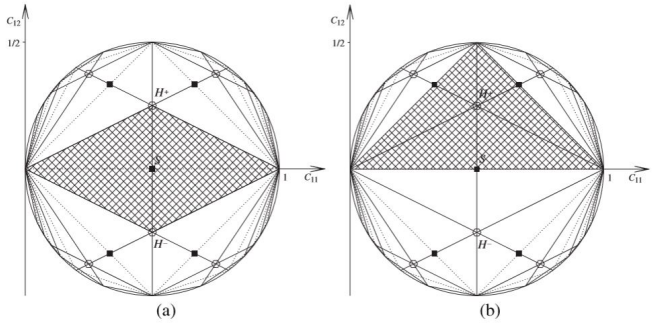

Figure 1.4: Examples of maximal EPNs on $\mathrm{Sym}^+(\mathbb{R}^2)$, indicated as hatched areas for a square-lattice metric on the left and for an hexagonal-lattice metric on the right. Taken from Conti, Zanzotto (2004).

1.1.2 Lattice-Continuum link: Energy density in crystalline solids

The objective of this part is to link the lattice picture to the continuum picture, in order to list the properties that the any class of energy densities for crystalline solids should respect. These properties are the driving forces that led to formulate the energetic model which will be presented in the next section, hence it is essential to present them.
First and foremost we review the Cauchy-Born hypothesis, which dictates how the deformation of lattice relates to the continuum body. Consider a crystalline body in a 2D setting that occupies a region Ω in the reference configuration. Let us assume that at each point $\mathbf{x} \in \Omega$ there is a 2D simple lattice with lattice vectors $\{\mathbf{e_i^o}(x)\}$. Now deform the body with some deformation $\mathbf{y}(\mathbf{x})$ such that the deformation gradient is $\mathbf{F}(\mathbf{x})$. The Cauchy-Born hypothesis states that the lattice follows the overall strain of the medium, hence the lattice vectors $\{\mathbf{e_i^o}(x)\}$ also deform according to the deformation gradient:

$$\mathbf{e_i}(\mathbf{x}) = \mathbf{F}(\mathbf{x})\, \mathbf{e_i^o}(\mathbf{x}). \tag{1.12}$$

Since we choose with homogeneous reference configurations, $\{\mathbf{e_i^o}\}$ is independent of $\mathbf{x}$.
This hypothesis provides the crucial linkage between macroscopic and microscopic world that alllows to formulate the energy density in terms of the lattice metric $\mathbf{C}$. The energy density is a function that depends on the the deformation gradient $\mathbf{F}$ and possibly on external parameters, such as the temperature ϑ, since it describes the stored energy density related to the deformation at a certain temperature. In general, it needs to satisfy two properties. The first one is known as *frame-indifference* and it requires that a rigid body rotation or a change of the observer does not change the energy:

$$\sigma(\mathbf{QF}, \vartheta) = \sigma(\mathbf{F}, \vartheta) \quad \forall \vartheta \in \mathbb{R}^+ \quad \forall \,\text{rotation}\, \mathbf{Q}. \tag{1.13}$$

This property can be directly expressed by changing the dependence of the energy through the tensor $\mathbf{C} = \mathbf{F}^T\mathbf{F} = \mathbf{C}^T > 0$. This tensor is known as *right Cauchy-Green deformation tensor* and it is rotation-indipendent. Indeed $\mathbf{C} = \mathbf{U}^2$ where $\mathbf{U}$ is the positive-definite symmetric right stretch tensor that stems from the polar decomposition of $\mathbf{F} = \mathbf{R}\,\mathbf{U}$ ($\mathbf{R}$ is a orthogonal rotation tensor, which is excluded from $\mathbf{C}$). Hence the strain energy can be defined as a function $\sigma = \sigma(\mathbf{C}, \vartheta)$: $\mathrm{Sym}^+(\mathbb{R}^2)\times\mathbb{R}^+ \to \mathbb{R}$. If we define the lattice metric associated with the current configuration $C_{ij} = \mathbf{e}_i \cdot \mathbf{e}_j$, the Cauchy-Born hypothesis yields:

$$C_{ij} = \mathbf{F}\mathbf{e}_i^o \cdot \mathbf{F}\mathbf{e}_j^o = \mathbf{e}_i^o\, \mathbf{F}^T\mathbf{F}\, \mathbf{e}_j^o = (\mathbf{F}^T\mathbf{F})_{ij}. \tag{1.14}$$

Equation (1.14) transparently displays that the energy can be interpreted to be dependent on the lattice metric because of the invariance with respect to galilean tranformations. Also, the lattice metric represents the right Cauchy-Green strain tensor in terms of the basis of the reference configuration provided that it is a orthonormal basis.
The second property that the energy must respect is *material symmetry*, which states that the free energy density does not depend on the choice of lattice vectors,

as long as they orginate equivalent lattices. In other words, this state function ought to identify the different basis representation of the same lattice. We can express this invariance in terms of metrics by the action (1.4):

$$\sigma(\mathbf{C},\vartheta)=\sigma(\mathbf{m}^T\mathbf{C}\mathbf{m},\vartheta)\quad\forall\vartheta\in\mathbb{R}^+\quad\forall\mathbf{C}\in\mathrm{Sym}^+(\mathbb{R}^2),\quad\forall\mathbf{m}\in GL(2,\mathbb{Z}).\quad(1.15)$$

Conventionally the strain energy is split into a convex volumetric part σ_v penalizing the departure of $\det\mathbf{C}$ from 1, plus a distortive term σ_d, which depends on the unimodular strain $\bar{\mathbf{C}}=(\det\mathbf{C})^{-1/2}\mathbf{C}$:

$$\sigma(\mathbf{C},\vartheta)=\sigma_v(\det\mathbf{C},\vartheta)+\sigma_d(\frac{\mathbf{C}}{\sqrt{\det\mathbf{C}}},\vartheta).\quad(1.16)$$

Notice that the volumetric part of the energy already satisfies (1.15), because $\det\mathbf{C}$ retains automatically the required invariance property. For the volumetric part of the energy,we adopt an expression ensuring an infinite energy penalty both to unbounded expansions and to increasing compressions. Temporarily neglecting the thermal effects, the volumetric part is

$$\sigma_v(\det\mathbf{C})=\nu\left(\det\mathbf{C}-\log\left(\det\mathbf{C}\right)\right)\quad(1.17)$$

where ν is a positive coefficient. Expression (1.17) is suitable first and foremost because it has a unique minimum for $\det\mathbf{C}=1$. On the other hand, deformations involving $\det\mathbf{C}=0$ are hindered because σ_v would diverge supporting the physical intuition. However, in most applications $\det\mathbf{C}$ remains close to 1 hence we settle for an alternative expression $\sigma_v(\det\mathbf{C})=\nu(\det\mathbf{C}-1)^2$.
We can easily incorporate the effect of the temperature in (1.17), which indulges volume expansion:

$$\sigma_v(\det\mathbf{C},\vartheta)=\nu\left(\det\mathbf{C}-\alpha\frac{\vartheta}{\vartheta_0}\log\left(\det\mathbf{C}\right)\right).\quad(1.18)$$

where α labels the volumetric thermal expansion coefficient. Expression (1.18) finds its minimum at $\det\mathbf{C}=\alpha\frac{\vartheta}{\vartheta_0}$, which is an increasing function of the temperature as required.
Next sections are devoted to the discussion of a general class of functions for the distorsive part.

1.2 A class of strain energy functions for 2D crystalline materials

The second section of this chapter is devoted to constructing of a class of strain energy functions that exploits the classical theory of modular forms on the Poincaré half-plane.
The first subsection tackles the problem of changing the setting for the distorsive part of the energy (see (1.16)) to the Poincaré half-plane $\mathcal{H}$, which parametrizes the strain space because of the existing relation between $\mathcal{H}$ and the space of metrics $\mathrm{Sym}^+(\mathbb{R}^2)$. It is then investigated the action of $GL(2,\mathbb{Z})$ on $\mathcal{H}$, for which

it is necessary to introduce the *Mobius tranformations*. The Dedekind tessellation candidly translates the action of $GL(2,\mathbb{Z})$ on $\mathcal{H}$ by covering it with mutually congruent copies of the fundamental domain. This new approach is due to Parry (1998), from which subsection (1.2.1) draws.
The follwing subsections (1.2.2) and (1.2.3) mainly summarize the original work done by E. Arbib in his Master's thesis "Modular order parameters in non-linear elasticity" (2016). First, it is introduced the class of *modular functions*, which suitably responds to most part of the requirements imposed on the strain energy function. Among these functions, the most representative is *Klein's invariant J*. The subsection unfolds around the implications of choosing J to construct the energy. Finally subsection (1.2.3) presents the final forms of strain potentials with a unique minimizer in the fondamental domain $\mathcal{D}$, which are suitable models for crystal plasticity phenomena.

1.2.1 The parametrization on the Poincaré half-plane $\mathcal{H}$

The Poincaré half-plane $\mathcal{H}$ is the subset of $\mathbb{C}$ given by

$$\mathcal{H} = \{z = x + i\,y \in \mathbb{C} \,:\, y > 0\}\,. \tag{1.19}$$

As the work unfolds, we will analogously call it upper-complex half plane. It is endowed with the metric tensor

$$\begin{bmatrix} \frac{1}{y^2} & 0 \\ 0 & \frac{1}{y^2} \end{bmatrix} \tag{1.20}$$

which can be rewritten in the form $(ds)^2 = ((dx)^2 + (dy)^2)/y^2$. (1.20) is the usual Euclidean metric tensor (the identity tensor) scaled by the positive factor $1/y^2$, which tends to infinity when the point approaches the line $y = 0$. This metric makes it a model of hyperbolic geometry, since it does not obey Euclid's parallel postulate. It can be shown that geodesics are modeled by straight vertical lines and half-circles whose origin is on the axis $y = 0$.
Parry (1998) established a surjective correspondance between the cone $\mathrm{Sym}^+(\mathbb{R}^2)$ and the Poincaré half-plane $\mathcal{H}$ by associating to any metric $\mathbf{C} \in \mathrm{Sym}^+(\mathbb{R}^2)$ the complex number

$$\hat{z}(\mathbf{C}) = \frac{C_{12}}{C_{11}} + i\,\frac{\sqrt{\det \mathbf{C}}}{C_{11}} \in \mathcal{H}. \tag{1.21}$$

The function $\hat{z}(\mathbf{C})$ is surjective because one can easily check that $\hat{z}(\mathbf{C}) = \hat{z}(\mathbf{C}')$ if and only if $\mathbf{C}$ and $\mathbf{C}'$ are proportional. In order to make the correspondance also injective, it is sufficient to reduce the space $\mathrm{Sym}^+(\mathbb{R}^2)$ to a two degrees of freedom space by introducing a further constraint on the space of symmetric and positive-definite 2×2 matrices, i.e. $\det \mathbf{C} = 1$. This means changing the domain of $\hat{z}$ to $\mathrm{SPsym}^+(\mathbb{R}^2)$, which precisely denotes the space of symmetric and positive-definite matrices with unitary determinant. The inverse of (1.21) can be explicitely computed by associating uniquely to a point $z = x + i\,y \in \mathcal{H}$ the metric $\mathbf{C} \in \mathrm{SPsym}^+(\mathbb{R}^2)$ defined by

$$\mathbf{C} = \begin{bmatrix} \frac{1}{y} & x/y \\ x/y & \frac{(x^2+y^2)}{y} \end{bmatrix}. \tag{1.22}$$

As (1.4) describes the action of $GL(2,\mathbb{Z})$ on $\mathrm{Sym}^+(\mathbb{R}^2)$, hence also on $\mathrm{SPsym}^+(\mathbb{R}^2)$, this action also naturally reflects on $\mathcal{H}$. We first analyze the action of the subgroup $SL(2,\mathbb{Z})$, which collects the 2×2 invertible matrices with integral entries and positive determinant $+1$ that describe orientation-preserving elements of $GL(2,\mathbb{Z})$. Each $\mathbf{m}\in SL(2,\mathbb{Z})$ induces the following mapping of $z\in\mathcal{H}$

$$\Gamma_{\mathbf{m}}(z)=\frac{m_{22}z+m_{12}}{m_{21}z+m_{11}}\quad\text{where}\quad m_{11}m_{22}-m_{12}m_{21}=1. \tag{1.23}$$

Since

$$\mathrm{Im}(\Gamma_{\mathbf{m}}(z))=\frac{\det\mathbf{m}\,\mathrm{Im}(z)}{|m_{21}z+m_{11}|^2}=\frac{\mathrm{Im}(z)}{|m_{21}z+m_{11}|^2}>0 \tag{1.24}$$

$\Gamma_{\mathbf{m}}$ maps $\mathcal{H}$ to itself. If $\mathbf{m}\in GL(2,\mathbb{Z})\setminus SL(2,\mathbb{Z})$, this is not true because $\det\mathbf{m}=-1$. In this latter case, action (1.23) must be modified so that each $\mathbf{m}\in GL(2,\mathbb{Z})\setminus SL(2,\mathbb{Z})$ induces the following mapping of $z\in\mathcal{H}$:

$$z\mapsto\overline{(\frac{m_{22}z+m_{12}}{m_{21}z+m_{11}})}=\frac{m_{22}\bar{z}+m_{12}}{m_{21}\bar{z}+m_{11}}. \tag{1.25}$$

Action (1.25) can be rewritten as

$$\Gamma_{\tilde{\mathbf{m}}}(\gamma(z))\quad\text{where}\quad\gamma(z)=-\bar{z}\quad\text{and}\quad\tilde{\mathbf{m}}=\begin{bmatrix}m_{11}&m_{12}\\-m_{21}&-m_{22}\end{bmatrix}. \tag{1.26}$$

Hence, if we associate to each matrix $\mathbf{m}\in GL(2,\mathbb{Z})$ the linear fractional tranformation $\Gamma_{\mathbf{m}}(z)=(m_{22}z+m_{12})/(m_{21}z+m_{11})$ the action of $GL(2,\mathbb{Z})$ on $\mathcal{H}$ is

$$\mathbf{m}(z)=\begin{cases}\Gamma_{\mathbf{m}}(z) & \text{if } \det\mathbf{m}=1\\ \Gamma_{\tilde{\mathbf{m}}}(\gamma(z)) & \text{if } \det\mathbf{m}=-1\end{cases}. \tag{1.27}$$

Few words should be spent around the linear tranformations $\Gamma_{\mathbf{m}}(z)$. They belong to the group of *Mobius transformations* $\Gamma:\mathcal{H}\to\mathbb{C}$ of the form

$$\Gamma(z)=\frac{a\,z+b}{c\,z+d} \tag{1.28}$$

where the coefficients a,b,c,d are complex numbers satisfying $ad-bc\neq 0$. Mobius tranformations are rational, analytic in $\mathcal{H}$ and it can be easily proven that they are also bijective (see Arbib (2016)). Furthermore, they are confomal map on $\mathcal{H}$, endowed with the metric $(ds)^2=((dx)^2+(dy)^2)/y^2$. If coefficients are integer, we speak about *unimodular group*; unimodular transformations are isometries on $\mathcal{H}$. They leave the distance between two points in $\mathcal{H}$ invariant and they map geodesics on geodesics.
Thus, action (1.27) generates orbits and fundamental domains on $\mathcal{H}$ coherently with the picture that takes shape on the specular space $\mathrm{SPsym}^+(\mathbb{R}^2)$. The Dedekind tessellation of $\mathcal{H}$ is the product of the action (1.27) (see Fig. 1.5 on page 19). This involves all the $GL(2,\mathbb{Z})$-related mutually congruent (in the sense of the hyperbolic metrics) copies of the fundamental domain, which is the strip

$$\mathcal{F}*=\{z\in\mathcal{H}:|z|\geq 1,0\leq\mathrm{Re}(z)\leq 1/2\}. \tag{1.29}$$

On the other hand, $\mathcal{F}* \cup \gamma(\mathring{\mathcal{F}}*)$ is a fundamental domain in $\mathcal{H}$ for the action of $SL(2,\mathbb{Z})$. Since $\mathcal{F}*$ and $\mathcal{D}$ in (1.10) are in a one-to-one correspondance, we will indifferently call $\mathcal{F}*$ as $\mathcal{D}$ from now onwards. The points in the interior of $\mathcal{D}$ correspond via (1.21) to metrics with trivial symmetry (oblique metrics), while the points that lie on the boundary $\partial\mathcal{D}$ correspond to metrics possessing nontrivial symmetries as it follows: rectangular lattices are points on the imaginary axis, while "fat" and "skinny" rhombic lattices correspond respectively to points $z \in \partial\mathcal{D}$ such that $|z| = 1$ and $\mathrm{Re}(z) = 1/2$. Finally the two maximally symmetric points, which are associated to a square and hexagonal lattice metric, are the two vertices of $\partial\mathcal{D}$, respectively $z = i$ and $z = 1/2 + i\sqrt{3}/2$. These can be obtained applying (1.21) to the metrics at the vertices of (1.10), which are precisely the square metric:

$$S = \begin{bmatrix} 1/2 & 0 \\ 0 & 1/2 \end{bmatrix} \tag{1.30}$$

and the hexagonal metric

$$H = \begin{bmatrix} 1/2 & 1/4 \\ 1/4 & 1/2 \end{bmatrix}. \tag{1.31}$$

All infinitely many copies of each point of the fundamental domain $\mathcal{D}$ can be obtained through a tranformation of the group $GL(2,\mathbb{Z})$. On the other hand, (1.27) guarantees that any of these transformations can be eventually seen as a a proper combination of the Mobius tranformation (1.23) associated to a matrix $\mathbf{m} \in SL(2,\mathbb{Z})$ and the reflection with respect to the imaginary axis $\gamma(z) = -\bar{z}$. Since the modular group associated to $\mathbf{m} \in SL(2,\mathbb{Z})$ is generated by the two tranformations $z \mapsto -1/z$ and $z \mapsto z + 1$, by considering these mappings together with $\gamma(z) = -\bar{z}$ we are equipped with whatever it takes to obtain any $z \in \mathcal{H}$ from each $z \in \mathcal{D}$. For instance, it is worth mentioning that the equivalent square point $z = \zeta = 1/2(i + 1)$ that appears in Fig. 1.5 on page 19 can be obtained by subsequently applying to $z = i$ those three mappings in the following order: $z \mapsto z + 1, \gamma(z)$ and finally $z \mapsto -1/z$. On the other hand, the equivalent square point $i + 1$ can be trivially obtained applying $z \mapsto z + 1$ to i.
Since we will heavily draw on the transformations $z \mapsto z + 1$, $z \mapsto -1/z$ and $z \to \gamma(z) = -\bar{z}$, we ought to specify their physical meaning following the procedure also reported in Arbib (2016).

Let us consider the following mapping $z_0 = x_0 + i\, y_0 \mapsto z_0 + 1$. By setting this transformation in the space $\mathrm{SPsym}^+(\mathbb{R}^2)$ through (1.22) we obtain:

$$\begin{bmatrix} \frac{1}{y_0} & \frac{x_0}{y_0} \\ \frac{x_0}{y_0} & \frac{x_0^2+y_0^2}{y_0} \end{bmatrix} \mapsto \begin{bmatrix} \frac{1}{y_0} & \frac{x_0+1}{y_0} \\ \frac{x_0+1}{y_0} & \frac{(x_0+1)^2+y_0^2}{y_0} \end{bmatrix}. \tag{1.32}$$

The physical meaning of (1.32) can be extrapolated by interpreting this tranformation in terms of the deformation gradient $\mathbf{F}$, whose relation with the metric tensor $\mathbf{C}$ is expressed through (1.14). However, $\mathbf{C}$ neutralizes the effect of the rotation hence the deformation gradients associated to the inital and final metrics of transformation (1.32) are unique up to a rotation. They are:

$$\begin{bmatrix} \frac{1}{\sqrt{y_0}} & \frac{x_0}{\sqrt{y_0}} \\ 0 & \sqrt{y_0} \end{bmatrix} \mapsto \begin{bmatrix} \frac{1}{\sqrt{y_0}} & \frac{x_0+1}{\sqrt{y_0}} \\ 0 & \sqrt{y_0} \end{bmatrix}. \tag{1.33}$$

The resulting $\mathbf{F}$ can be decomposed as:

$$\begin{bmatrix} \frac{1}{\sqrt{y_0}} & \frac{x_0+1}{\sqrt{y_0}} \\ 0 & \sqrt{y_0} \end{bmatrix} = \begin{bmatrix} 1 & \frac{1}{y_0} \\ 0 & 1 \end{bmatrix} \begin{bmatrix} \frac{1}{\sqrt{y_0}} & \frac{x_0}{\sqrt{y_0}} \\ 0 & \sqrt{y_0} \end{bmatrix} \tag{1.34}$$

This expression transparenly shows that $z_0 \mapsto z_0 + 1$ can be interpreted as a simple shear $\mathbf{F} = \mathbf{I} + 1/y_0 \mathbf{i}_1 \otimes \mathbf{i}_2$ applied to a reference configuration whose deformation gradient $\mathbf{F}_0$ is the second one on the right-hand side of (1.34).

Let us consider the mapping living in $\mathcal{H}$ $z_0 = x_0 + i\, y_0 \mapsto -1/z_0 = -x_0/(x_0^2 + y_0^2) + iy_0/(x_0^2 + y_0^2)$. This reflects on $\mathrm{SPsym}^+(\mathbb{R}^2)$ thorugh (1.22) in the following way:

$$\begin{bmatrix} \frac{1}{y_0} & \frac{x_0}{y_0} \\ \frac{x_0}{y_0} & \frac{x_0^2+y_0^2}{y_0} \end{bmatrix} \mapsto \begin{bmatrix} \frac{x_0^2}{y_0} + 1 & -\frac{x_0}{y_0} \\ -\frac{x_0}{y_0} & \frac{1}{y_0} \end{bmatrix}. \tag{1.35}$$

The associated deformation gradients are:

$$\begin{bmatrix} \frac{1}{\sqrt{y_0}} & \frac{x_0}{\sqrt{y_0}} \\ 0 & \sqrt{y_0} \end{bmatrix} \mapsto \begin{bmatrix} \frac{x_0}{\sqrt{y_0}} & -\frac{1}{\sqrt{y_0}} \\ \sqrt{y_0} & 0 \end{bmatrix}. \tag{1.36}$$

The final matrix can be decomposed as:

$$\begin{bmatrix} \frac{x_0}{\sqrt{y_0}} & -\frac{1}{\sqrt{y_0}} \\ \sqrt{y_0} & 0 \end{bmatrix} = \begin{bmatrix} \frac{1}{\sqrt{y_0}} & \frac{x_0}{\sqrt{y_0}} \\ 0 & \sqrt{y_0} \end{bmatrix} \begin{bmatrix} 0 & -1 \\ 1 & 0 \end{bmatrix}. \tag{1.37}$$

Hence the tranformation corresponds to a $\pi/2$-prerotation as it precedes $\mathbf{F}_0$ (which is now the first matrix on the right-hand side of (1.37).

Finally it can be proven through an analogous computation that the mapping $z_0 \mapsto \gamma(z_0)$ corresponds to a reflection with respect to the horizontal axis x which precedes $\mathbf{F}_0$.

1.2.2 Modular functions: The Klein Invariant J

The previous discussion allows to set the construction of an explicit expression for the distorsive part of the strain energy function (see expression (1.16)) in a new domain, which is precisely the Poincaré half-plane $\mathcal{H}$, in light of the existing bijective relation with the space of metrics $\mathrm{SPsym}^+(\mathbb{R}^2)$. Hence $\mathcal{H}$ now parametrizes the strain space and the Dedekind tessellation transparently displays the constraints imposed by simmetry on the material's energy landscape. As a consequence, it emerges that potentials for 2D crystalline materials are closely related to the classical modular functions as follows.
First, by exploting bijection (1.21) we rigorously reformulate $\sigma_d(\bar{\mathbf{C}}, \vartheta)$; we think of it as a function $\varphi : \mathcal{H} \times \mathbb{R}^+ \to \mathbb{R}$ such that

$$\varphi(z, \vartheta) := \sigma_d(\bar{\mathbf{C}}, \vartheta), \text{where } z = \hat{z}(\bar{\mathbf{C}}) = \frac{1}{\bar{C}_{11}}(\bar{C}_{12} + i). \tag{1.38}$$

While the property of frame-indifference is intrinsically satisfied by expressing the energy in terms of the lattice metric (this dependence translates now into the

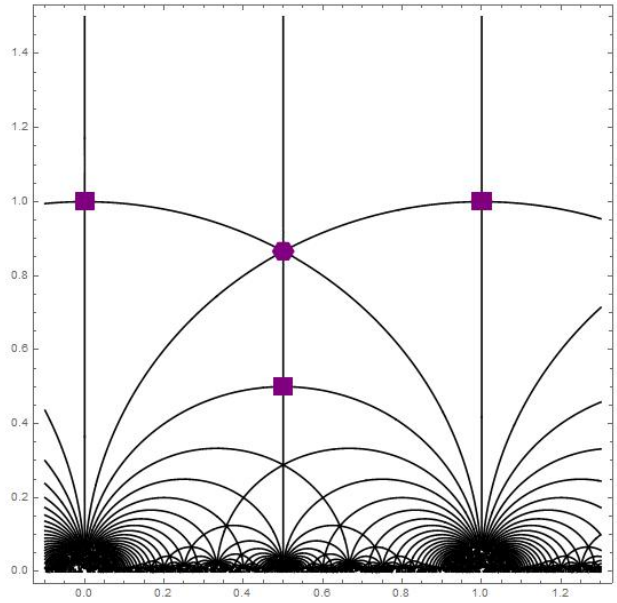

Figure 1.5: The Dedekind tessellation of a portion of the Poincaré half-plane $\mathcal{H}$ generated by the action of the group $GL(2,\mathbb{Z})$. Three equivalent square points (i,$i+1$, and $\zeta = \frac{1}{2}(i+1)$), and one hexagonal point ($\rho = e^{i\pi/3} = 1/2(1+\sqrt{3})$) are indicated.

dependence on $z \in \mathcal{H}$), $GL(2,\mathbb{Z})$-invariance property (material symmetry) must be revised through (1.27) as

$$\begin{cases} \varphi(z,\vartheta) = \varphi(\Gamma_{\mathbf{m}}(z),\vartheta) & \forall \mathbf{m} \in SL(2,\mathbb{Z}), \forall z \in \mathcal{H}, \forall \vartheta \in \mathbb{R}^+ \\ \varphi(z,\vartheta) = \varphi(\Gamma_{\tilde{\mathbf{m}}}(\gamma(z)),\vartheta) & \forall \mathbf{m} \in GL(2,\mathbb{Z}) \setminus SL(2,\mathbb{Z}), \forall z \in \mathcal{H}, \forall \vartheta \in \mathbb{R}^+ \end{cases}. \tag{1.39}$$

Since $\det \tilde{\mathbf{m}} = 1$, the second requirement in (1.39) can be equivalently seen as the composition of a orientation-preserving tranformation and the function $\gamma(z)$. Hence, (1.39) can be rewritten as

$$\begin{cases} \varphi(z,\vartheta) = \varphi(\Gamma_{\mathbf{m}}(z),\vartheta) & \forall \mathbf{m} \in SL(2,\mathbb{Z}), \forall z \in \mathcal{H}, \forall \vartheta \in \mathbb{R}^+ \\ \varphi(z,\vartheta) = \varphi(\gamma(z),\vartheta) & \forall z \in \mathcal{H}, \forall \vartheta \in \mathbb{R}^+ \end{cases}. \tag{1.40}$$

There exists a class of complex-valued functions on the upper half-plane $\mathcal{H}$ that precisely serves the first purpose of (1.40), i.e. $SL(2,\mathbb{Z})$-invariance, known as *modular functions*. These functions are classified stemming from their behavior at infinity. Thus, a further reformulation occurs: $\Phi(K(z),\vartheta) := \varphi(z,\vartheta)$ where $\Phi : \mathbb{C} \times \mathbb{R}^+ \to \mathbb{R}$ and $K : \mathcal{H} \to \mathbb{C}$ is a complex-valued operator on the Poincaré half-plane $\mathcal{H}$ Γ-invariant

$$K(z) = K(\Gamma_{\mathbf{m}}(z)) \quad \forall \mathbf{m} \in SL(2,\mathbb{Z}). \tag{1.41}$$

The second requirement in (1.40) will be discussed later.
Besides the already mentioned properties, the strain energy function has to satisfy

a list of further hypotheses in order to be mathematically and physically consistent. These properties are imparted on the operator K through which the energy is constructed. We now want to list them for good in order to properly justify any prospective choice.

1. $K(z)$ has to be periodic under the action of the group $GL(2,\mathbb{Z})$ on $\mathcal{H}$, as (1.41) already partially expresses for the subgroup $SL(2,\mathbb{Z})$.

2. $K(z)$ has to be one-to-one when restricted to the fundamental domain $\mathcal{D}$, thus it has to have the property of mapping the fundamental domain to the entire complex plane.

3. $K(z)$ has to be holomorphic on $\mathcal{H}$, except at most isolated singularities. Such a regularity is required in order to eventually be able to properly differentiate the strain energy function. On the one hand, stress tensors are computed by conveniently differentiating the strain energy density function. On the other hand, under the hypothesis of small displacements around the equilibrium configuration, by substituting the energy with its second-order Taylor expansion around this position it is possible to derive the linear theory of elasticity from the non-linear framework. Hence the energy has to be sufficiently regular; when moving to the complex context, we directly require holomorfism for the sake of semplicity.

4. $K(z)$ diverges when $z \to i\infty$ with a simple pole at infinity. Therefore, we assign infinite energy to the configurations in the neighbourhood of $z = i\infty$. These are configurations such that one lattice vector length is extremely larger than the other one, i.e. a certain "aspect ratio" of the cells of the lattice diverges. Geometrically, this involves an unbounded distortion of the lattice.

There are not that many functions which satisfy the requirements 1. to 4. In fact, they can all be built up (via rational functions) from the *Klein's invariant* J, which is thus the most representative among modular functions.
We briefly illustrate how it is defined; an extensive discussion upon it can be found in Apostol (1976). Given $\tau \in \mathcal{H}$, let us define:

$$g_2(\tau) = 60 \sum_{\substack{m,n=-\infty \\ (m,n)\neq(0,0)}}^{+\infty} \frac{1}{(m+n\tau)^4} \quad \text{and} \quad g_3(\tau) = 140 \sum_{\substack{m,n=-\infty \\ (m,n)\neq(0,0)}}^{+\infty} \frac{1}{(m+n\tau)^6}. \tag{1.42}$$

These functions are called *invariants*. Through these functions we can define the *discriminant* $\Delta = g_2^3(\tau) - 27\, g_3^2(\tau)$ such that $\Delta(\tau) \neq 0$ for all $\tau \in \mathcal{H}$. Finally the Klein Invariant J is a function $J : \mathcal{H} \to \mathbb{C}$ defined by:

$$J(\tau) = \frac{g_2^3(\tau)}{\Delta(\tau)}. \tag{1.43}$$

As a modular function, the Klein invariant $J(z)$ satisfies property (1.41). Furthermore, it satisfies property 2, 3 and 4. It attains respectively the values 0 and 1 at the vertices $z = e^{i\pi/3} = \rho$ and $z = i$ of $\mathcal{D}$. Boundary points of the fundamental

domain are mapped onto the real axis and $J(z) \to \infty$ also whenever z approaches a rational point on the real axis, which would imply $\sqrt{\det \mathbf{C}}/C_{11} \to 0$ ($\sqrt{\det \mathbf{C}}/C_{11}$ describes again a certain aspect ratio with $\det\mathbf{C}$ finite, hence it is analogously a "large shear" condition).
In light of these considerations, $K = J$. Hereafter we restrict ourselves to the case in which the distorsive part of the energy has a *single* minimizer. This allows us to model crystal plasticity phenomena; we can imagine that the temperature ϑ is fixed and thus we can drop the dependence on this parameter when writing explicit expressions for the energy.
Assuming a defect-free homogeneus reference lattice, with metric $\bar{\mathbf{C}}_0$ such that $z_0 = \hat{z}(\bar{\mathbf{C}}_0)$, to be an energy-minimizing state, the desired convex potential σ_d (see (1.16)) can be now written in terms of $J_0(z) = J(z) - J(z_0)$:

$$\sigma_d(\bar{\mathbf{C}}) = \sigma_d(J_0(\hat{z}(\bar{\mathbf{C}}))). \tag{1.44}$$

The first proposal for the simplest family of energy functions is then spontaneously:

$$\Phi(J_0(z)) = \mu|J(z) - J(z_0)|^2 \tag{1.45}$$

where $\mu > 0$ is an elastic modulus, i.e. a parameter which could be easily measurd experimentally and incorporated into the function. One important remark concerns the presence of the absolute value in this expression. Among the several advantages conveyed when using the Klein Invariant J to lay the foundation of the potential energy, we did not mention the following fact:

$$J(z) = \overline{J(-\bar{z})} \quad \forall z \in \mathcal{H}. \tag{1.46}$$

Hence $\Phi(J(z)) = \Phi(\overline{J(-\bar{z})})$. To have $GL(2,\mathbb{Z})$-invariance, which means satisfying also the invariance with respect to the reflection $\gamma(z) = -\bar{z}$ (see the second requirement in (1.40)), the energy must depend on the square of the imaginary part of $J(z)$ in order to neutralize the undesired effect of the external complex conjugation in (1.46). However, (1.45) complies with this demand only if $\mathrm{Im}(J(z_0)) = 0$, which is the case of a reference minimizer z_0 with non-trivial symmetry ($z_0 \in \partial\mathcal{D}$). Therefore, when $z_0 \in \partial\mathcal{D}$, (1.45) exhibit full $GL(2,\mathbb{Z})$-invariance. When z_0 belongs to the interior of $\mathcal{D}$, (1.45) needs to be suitably modified so as to obtain dependence on $\mathrm{Im}^2(J(z_0))$. This discussion is deferred to the next subsection.
Expression (1.45) gives the first model for a simplest class of $GL(2,\mathbb{Z})$-invariant potentials with pre-assigned minimizers on $\partial\mathcal{D}$. Yet, not all points on $\partial\mathcal{D}$ constitute an admissible choice for the minimizer z_0. Indeed, we will now examine what implications the use of J prompts. As property 4 outlines, we should be able to stem from the strain functions also the whole context of the linear theory of elasticity. This implies that the energy must exhibit a correct positive-definite behavior of linear elasticity for z near the minimizer $z_0 \in \mathcal{H}$ and all its symmetry-related copies, i.e $\sigma(J_0(z)) \approx (z - z_0)^2$. Although J perfectly suits most of the mentioned properties, in this circumstance it flaws. Indeed, up to tranformations in the same $SL(2,\mathbb{Z})$-orbit it holds

$$J'(i) = 0, \quad J'(\rho) = 0, \quad J''(\rho) = 0, \quad J'(z) \neq 0 \, \forall z \notin \{i, \rho\}\,. \tag{1.47}$$

In other words, the two maximally symmetric points corresponding to a square and an hexagonal lattice are the only predetermined stationary points of J forced by modular invariance. Precisely J satisfies $J(z) = J(i) + O(z-i)^2$ as $z \to i$ and $J(z) = J(\rho) + O(z-\rho)^3$ as $z \to \rho$. This property would affect an energy of the form (1.45) (being z_0 a point representing either a square lattice or an hexagonal lattice) by prompting the second derivative of the function to be zero in correspondance with the maximally-symmetric metrics. Hence, (1.45) is not compatible with neither the choice $z_0 = i$ nor $z_0 = \rho$. It can be proven (see Arbib (2016)) that this issue occurs for any Φ that is regular for $z = i$ and $z = \rho$. In order to surmount this obstacle, Zanzotto (unpublished work) proposes the introduction of suitable non-holomorphic complex functions ψ to compose with J so as to eliminate higher-order zeroes of J and not to lose the global regularity of Φ, with $\Phi = \Phi((\psi \circ J)(z))$.
Let us consider the case of $z_0 = i$. To make such functions explicit, we have to precisely impose that i is not a critical point of the function $\psi \circ J$. Hence:

$$\lim_{z \to i} (\psi \circ J)'(z) = \kappa \neq 0 \tag{1.48}$$

which implies

$$\lim_{z \to i} \psi'(J(z)) J'(z) = \kappa \neq 0. \tag{1.49}$$

See Arbib (2016) for the technical requirements on ψ that allow to write expression (1.49). Expression (1.49) suggests that $\psi'(J(z))$ must have a pole of order 1 in i so as to eliminate the first order zero of J. Thus $\psi'(J(z))$ can be written as

$$\psi'(J(z)) = \frac{h_1(z)}{z-i} \quad h_1(z) \,\text{analytical in}\, \mathbb{C},\, h(i) \neq 0. \tag{1.50}$$

Since $J - 1$ has in i a zero of order 2, one can write $J(z) - 1 = (z-i)^2 h_2(z)$, with $h_2(i) \neq 0$ and analytical in $\mathbb{C}$. By conveniently chosing $h_1(z)$ and $h_2(z)$, we are able to write

$$\psi'(J(z)) = \frac{1}{\sqrt{J(z)-1}} \to \psi(J(z)) = \sqrt{J(z)-1} \tag{1.51}$$

up to some non-significant multopling constants.
Applying an analogous argument, we can obtain the result for $z = \rho$: $\psi(J(z)) = \sqrt[3]{J(z)}$. Both $\sqrt{J-1}$ and $\sqrt[3]{J}$ are holomorphic functions on $\mathcal{H}$ on the assumption that the branches of each complex function are properly combined (see Schoeneberg (1974)). Hence, the global regularity of Φ is preserved.
However, a further pitfall occurs. The combination of holomorphism and $SL(2,\mathbb{Z})$-invariance prove to be conflicting with the requirement that $(\psi \circ J)'(i) \neq 0$ where $\psi \circ J : \mathcal{H} \to \mathbb{C}$. Indeed, it holds that if $f : \mathcal{H} \to \mathbb{C}$ is analytic and $SL(2,\mathbb{Z})$-invariant, then $f'(i) = 0$. The proof is straightforward. From $SL(2,\mathbb{Z})$-invariance, it holds:

$$f(z) = f(-\frac{1}{z}) \quad \forall\, z \in \mathcal{H}. \tag{1.52}$$

Notice that the transformation $z \mapsto -1/z$ together with the tranformation $z \mapsto z+1$ generate $SL(2,\mathbb{Z})$. Since f is analytic, we are allowed to differentiate (1.52). We obtain

$$f'(z) = f'(-\frac{1}{z})\,\frac{1}{z^2} \quad \forall\, z \in \mathcal{H} \quad \to \quad f'(i) = f'(i)(-i). \tag{1.53}$$

Hence $f'(i) = 0$. An identical result holds also when considering $z = \rho$ and when restricting the codomain of f to $\mathbb{R}$.
As a consequence, we obtain that we should not try to avoid the properties $J'(i) = 0$ and $J'(\rho) = 0$ by composing it with a ψ function as these properties are in agreement with our request on the energy to be regular and $SL(2, \mathbb{Z})$-invariant.

The last remaining problem deals with the Hessian of the function being 0 whenever we want the energy minimizer to correspond to one of the two maximally-symmetric points $z_0 = i$ or $z_0 = \rho$.
Let us consider the case of $z = i$. Furthermore, we indicate $\psi_1(z) = \sqrt{z-1}$, i.e. the function that we obtained in the previous computations for this case (see (1.51)). In order to avoid critical points predetermination of the function J', it is not sufficient anymore to conveniently combine J with some complex operators. Arbib proposes the introduction of a new regular operator $\omega : \mathbb{C} \to \mathbb{R}$ that is indifferent to the choice of the branches of the $\sqrt{z}$. Under this latter hypothesis it can be proven then that $\omega \circ \hat{\psi}_1 \circ J$ is also regular, where $\hat{\psi}_1$ is a function analogous to ψ_1 that just preserves the principal branch of the square root. Thus, since $\hat{\psi}_1$ is not holomorphic it allows to eliminate the pre-determined critical points without ever discarding $SL(2, \mathbb{Z})$-invariance. One can see that if the operator ω is interpreted as a function from $\mathbb{R}^2$ to $\mathbb{R}$ the condition of indifference to the branches of the square root translates into:

$$\hat{\omega}(x, y) = \hat{\omega}(-x, -y) \quad \forall (x, y) \in \mathbb{R}^2 \tag{1.54}$$

where $\hat{\omega}$ precisely indicates ω when intepreting its domain as $\mathbb{R}^2$. Arbib proves that if such an $\hat{\omega}$ has a minimum in $(0, 0)$ with a positive-definite Hessian, then also the Hessian of $\omega \circ \hat{\psi}_1 \circ J$ is non-zero. Hence, in order to finally construct a strain energy function with a minimum in the square lattice one can select a regular polynomial function $\hat{\omega}$ respecting (1.54) and having a minimum in $(0, 0)$ as

$$\hat{\omega}(x, y) = x^2 + y^2. \tag{1.55}$$

Thus, retrieving formulation (1.38) this energy has the form

$$\varphi(z) = \mu |\sqrt{J - 1}|^2 = \mu |J(z) - 1| \tag{1.56}$$

where $\mu > 0$ is an elastic modulus.
Now we consider the case of $z = \rho$. The $\hat{\omega}$ function has to be determined so as to be regular, with a minimum in $(0, 0)$ and invariant with respect to the branches of the cubic root:

$$\hat{\omega}(x, y) = \hat{\omega}(-\frac{1}{2}x - \frac{\sqrt{3}}{2}y, \frac{\sqrt{3}}{2}x - \frac{1}{2}y) \quad \forall (x, y) \in \mathbb{R}^2. \tag{1.57}$$

A polynomial expression satisfying this property is again (1.55). Thus a simple form of a $GL(2, \mathbb{Z})$-invariant potential with pre-assigned minimizer on the hexagonal lattice is

$$\varphi(z) = \mu |J(z)|^{\frac{2}{3}}. \tag{1.58}$$

1.2.3 Final forms of single minimizers strain potentials

We are now able to summarize expressions (1.45),(1.56) and (1.58) in a unique expression. These energy forms all share the same restriction on the choice of z_0: this must be chosen on the boundary $\partial\mathcal{D}$ of the fundamental domain $\mathcal{D}$. Hence, when a single minimizer in $\partial\mathcal{D}$ is present the simplest functions σ_d can be given by the unified expression

$$\sigma_{d,plast} = \sigma_{d,z_0} = \mu|J(z) - J(z_0)|^{2/\chi(z_0)} \tag{1.59}$$

where $\mu > 0$ is an elastic modulus, and $\chi(z_0)$ is the order of zero of $J(z) - J(z_0)$, near the given z_0. In particular $\chi(z_0) = 1$ if $J'(z_0) \neq 0$, i.e. for all $z_0 \in \partial\mathcal{D}$ except i and ρ, $\chi(z_0) = 2$ if $z_0 = i$ and $\chi(z_0) = 3$ if $z_0 = \rho$. The subscript *plast* has been added precisely to indicate that through (1.59) we can explore crystal plasticity. The modeling of martensitic phase transformations require the re-introduction of the dependence on ϑ. This will be discussed in the next chapters, which also represent the original core of this thesis.
When we introduced expression (1.45) in the last subsection, we remarked that it is possible to suitably modify it in order to obtain dependence on $\mathrm{Im}^2(J(z_0))$, which is the essential condition to ensure full $GL(2,\mathbb{Z})$-invariance when z_0 belongs to the interior of $\mathcal{D}$. Hence, when a single minimizer is present in the interior of $\mathcal{D}$ the simplest function σ_d is given by

$$\sigma_{d,plast} = \sigma_{d,z_0} = \mu\left[\mathrm{Re}^2(J(z) - J(z_0)) + \left(\mathrm{Im}^2(J(z)) - \mathrm{Im}^2(J(z_0))\right)^2\right]. \tag{1.60}$$

In the next chapters we will just make use of the expression (1.59). This expression holds for any z_0 such that $\mathrm{Im}(J(z_0)) = 0$. This condition divides the points depending on their symmetry. While the points on the boundary $\partial\mathcal{D}$ (recall that $\mathrm{Im}(J(z))|_{\partial\mathcal{D}} = 0$) show non-trivial symmetry, those in the interior of the fundamental domain correspond to oblique metrics that are preserved only when undergoing trivial transformations (see Fig. 1.1 on page 8). On the other hand, shape memory effect normally exhibits when the austenite phase presents a square lattice and the martensite phase presents a rhombic or rectangular lattice hence a certain symmetry is always maintained.
The last remark concerns the possibility to rewrite expression (1.59) so as to describe an energy exhibiting square anisotropic elasticities. Since we are considering the case of $z = i$ we can directly consider expression (1.56). This energy can be modified as follows

$$\sigma_{d,sq,aniso} = \mu\,\mathrm{Re}^2\sqrt{J(z) - 1} + \lambda\,\mathrm{Im}^2\sqrt{J(z) - 1} \tag{1.61}$$

where $\lambda > 0$.
On the other hand, it can be proven (see Arbib (2016)) that for any regular function $g : \mathcal{H} \to \mathbb{R}$ $GL(2,\mathbb{Z})$-invariant the Hessian evaluated at $z = \rho$ is always proportional to the 2×2 identity matrix, hence the energy can never exhibits hexagonal anisotropic elasticities. Though, one can proceed in an analogous way as we did for (1.61) for the elastic anistropies when the minimizer z_0 has lower symmetry than square or hexagonal by properly introducing a λ parameter.

Chapter 2

A model for reconstructive phase tranformations

In this chapter we present the first model for a strain energy function with *two* pre-assigned minimizing lattices z_0 and z_1. The model of the energy needs to be able to forecast a discontinuous variation of the equilibrium configurations from z_0 to z_1 and viceversa, according to temperature. Indeed, this is the physical context of martensitic phase transformations, which can be classified as first-order phase transformations.
In accordance with the mathematical hypotheses depicted in the previous chapters, we reduce ourselves to work in the fundamental domain $\mathcal{D}$ and to choose the two minimizers, z_0 and z_1, on its boundary $\partial\mathcal{D}$, so that the corrisponding reference lattices have some non-trivial point-symmetry.
We first explore the relevant case of the two maximally-symmetric points, square and hexagonal lattices; hence, $z_0 = i$ and $z_1 = \rho = e^{i\frac{\pi}{3}}$. The choice of the two maximally-symmetric points as minimizers complies with the representation of reconstructive irreversible tranformations, whose essential hypothesis is the impossibility of including the symmetry group of the parent and product phases in a common finite symmetry group. The symmetry groups of the two maximally symmetric lattices generate the entire global symmetry group of Bravais lattices (see Bhattacharya, Conti, Zanzotto and Zimmer (2004)).
We will just take into account the distorsive part σ_d of the strain energy function because the volumetric part σ_v can be kept as in (1.18). Since we want to describe phase transitions, we now have to consider the dependence on the temperature.
In the first section we discuss the construction of the explicit expression of a potential suitable for the square-to-hexagonal reconstructive tranformation.
In the second section we explore the variation of the character of $z = i$ and $z = \rho$ according to the temperature regime.
In the third section we proceed to probe how the whole energetic landscape varies with respect to the temperature and we analyze the bifurcations of critical points in each temperature regime.
In the fourth and last section we investigate plastic phenomena; in particular the computation of the energy barriers existing between adjacent square equilibrium configurations will be relevant when adressing numerical simulations in the last chapter.

2.1 The simplest model

We are already equipped with a quite rich toolbox to devise a potential that finds rest into square and hexagonal lattices. The most simple idea is to linearly combine the potential with a unique minimum in $z = i$ (expression (1.56)) and the potential with a unique minimum in $z = \rho$ (expression (1.58)), with the help of two parameters:

$$\sigma_d(\bar{\mathbf{C}}, \alpha, \beta) = \alpha|J(\hat{z}(\bar{\mathbf{C}})) - 1| + \beta|J(\hat{z}(\bar{\mathbf{C}}))|^{\frac{2}{3}}. \tag{2.1}$$

The simplicity of this expression is effective because of the favorable properties of the Klein Invarant J, which ensure that the linear combination of two functions with two single and different minimizers proves to be stationary in both these two points as the next subsection will show. This is in general not true. Consider two real functions $f_1, f_2 : \mathbb{R} \to \mathbb{R}$ having a unique minimum in two different points, say $x = 1$ and $x = 2$, as for instance $f_1(x) = (x-1)^2$ and $f_2(x) = (x-2)^2$; the function resulting from the linear combination of f_1 and f_2, $f(x) = \alpha(x-1)^2 + \beta(x-2)^2$, does not have a stationary point neither in $x = 1$ nor in $x = 2$.
Collecting α, we highlight how this expression solely depends on one parameter, which is the ratio $\frac{\beta}{\alpha}$. Indeed, α becomes a coefficient that changes the magnitude of the energy but that does not influence its intrinsic shape:

$$\sigma_d(\bar{\mathbf{C}}, \alpha, \beta) = \alpha(|J(\hat{z}(\bar{\mathbf{C}})) - 1| + \frac{\beta}{\alpha}|J(\hat{z}(\bar{\mathbf{C}}))|^{\frac{2}{3}}).$$

For this reason, we performed the whole analysis considering only one free parameter, fixing one between α and β. As already discussed, one of the required hypothesis on the energy is:

$$\lim_{z \to +i\infty} \varphi(z) = +\infty.$$

Notice that we implied the reformulation of the energy $\varphi(z) := \sigma_d(\bar{\mathbf{C}})$, $\varphi(z) : \mathcal{H} \to \mathbb{R}$ through the bijection $z = \hat{z}(\bar{\mathbf{C}}) : \mathrm{SPsym}(\mathbb{R}^2) \to \mathcal{H}$, where $\mathcal{H}$ is the Poincaré half-plane. This correspondance will be considered as understood as this chapter unfolds. In order to respect this hypothesis α needs to be strictly positive, because it is the coefficient multiplying the dominant term:

$$\sigma_d(\bar{\mathbf{C}}, \alpha, \beta) \sim \alpha|J(\hat{z}(\bar{\mathbf{C}})) - 1| \quad \hat{z}(\bar{\mathbf{C}}) \to +i\infty. \tag{2.2}$$

Hence, we fixed $\alpha = 1$. By emphasizing the dependence on the unique free parameter β, the expression of the energy on which we performed the analysis is:

$$\sigma_{d,rec}(\bar{\mathbf{C}}, \beta) = |J(\hat{z}(\bar{\mathbf{C}})) - 1| + \beta|J(\hat{z}(\bar{\mathbf{C}}))|^{\frac{2}{3}}. \tag{2.3}$$

The subcript *rec* stands for "reconstructive", as we will show that (2.3) models the energy density of a reconstructive martensitic transformation. Hereafter for brevity we avoid indicating the subscripts. Similarly, the dependence on the parameters α and β will not be always explicit even though it is conceptually preserved.
The significance of α and β does not reduce to being the coefficients of the linear combination and to controlling the divergence of the strain energy function. Besides having a mathematical effect, they have a natural physical meaning thanks to the

properties of the Klein invariant J; this latter attains respectively the values 1 and 0 at the vertices $z_0 = i$ and $z_1 = \rho = e^{i\frac{\pi}{3}}$ of $\mathcal{D}$. Therefore α and β are respectively the values of the height of the energy at the points representing the hexagonal lattice and the square lattice:

$$\varphi(i) = \beta \qquad \varphi(\rho) = \alpha = 1. \tag{2.4}$$

Through the variation of the ratio $\frac{\beta}{\alpha}$, it is possible to control the relative heights and to change the optimal configurations. The properties of the temperature are thus discharged on this ratio and, by fixing α, they are ultimately discharged on β. It will be clarified later how β is connected with the temperature.

2.2 The stability of the maximally-symmetric points

Such a simple form of the energy as the one presented ensures easily that the characteristics required to represent a first-order phase transition are respected. The strain energy function must depict the stability exchange between the square and hexagonal lattice configurations as their temporary coexistence in the state of minima.
The only free parameter β rules the character variations of the two maximally-simmetric points. Once again, thanks to the properties of the Klein invariant J, these latter are always stationary points and β just influences the second derivative of the energy, as we are about to show.

For the following computations, we will consider a further reformulation of the energy $\Phi(J(z)) := \varphi(z)$, $\Phi(J(z)) : \mathbb{C} \to \mathbb{R}$, which gives the two rules:

$$\varphi'(z) = \Phi'(J(z))J'(z) \qquad \varphi''(z) = \Phi''(J(z))(J'(z))^2 + \Phi'(J(z))J''(z). \tag{2.5}$$

In order to simplify, we rewrite (2.3) to highlight that it was born from two separate potentials:

$$\varphi(z, \beta) = \varphi_{sq}(z) + \beta\, \varphi_{hex}(z) \tag{2.6}$$

where φ_{sq} is (1.56) and $\varphi_{hex}(z)$ is (1.58).
Applying the first rule of (2.5) to both members of (2.6), the term $J'(z)$ appears. Since $J'(i) = 0, J'(\rho) = 0$,

$$\varphi'(i, \beta) = 0 \qquad \varphi'(\rho, \beta) = 0 \qquad \forall\beta. \tag{2.7}$$

For what concerns the second derivative, we recall that $\varphi_{sq}(z)$ and $\varphi_{hex}(z)$ have a correct positive-definite behavior of linear elasticity respectively in the vicinity of the minimizers i and ρ. Hence:

$$\varphi''_{sq}(z) = \begin{cases} > 0 & \text{if} \quad z = i \\ 0 & \text{if} \quad z = \rho \quad \text{because} \quad J''(\rho) = 0 \end{cases} \tag{2.8}$$

$$\varphi''_{hex}(z) = \begin{cases} \Phi'_{hex}(J(i))J''(i) & \text{if} \quad z = i \quad \text{because} \quad J''(i) \neq 0 \\ > 0 & \text{if} \quad z = \rho \end{cases}. \tag{2.9}$$

We obtain:

$$\varphi''(i, \beta) = \varphi''_{sq}(i) + \beta\, \varphi''_{hex}(i) \tag{2.10}$$

$$\varphi''(\rho, \beta) = \beta\, \varphi''_{hex}(\rho) \tag{2.11}$$

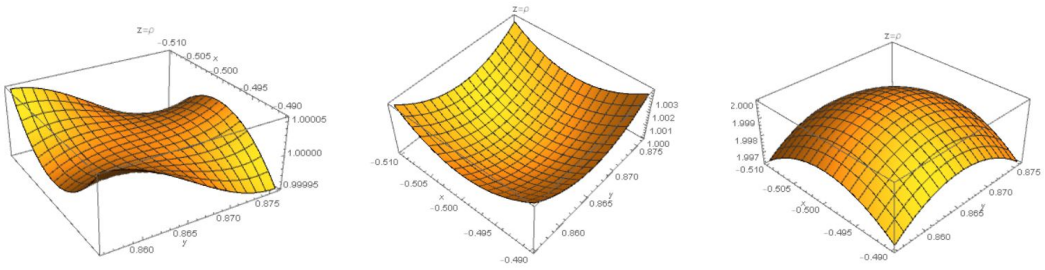

(a) $\beta = 0$ **(b)** $\beta = 2$ **(c)** $\beta = -2$

Figure 2.1: Energy surface in a neighboor of $z = \rho$ for different values of β. For $\beta = 0$, $z = \rho$ is a monkey-saddle. For $\beta = 2$, $z = \rho$ is a minimum. For $\beta = -2$, $z = \rho$ is a maximum.

2.2.1 The hexagonal lattice

We now want to investigate what expressions (2.10) and (2.11) involve. We first focus on (2.11).
The articulation of the strain energy function in a different setting can be exploited again to better express some concepts. The natural identification between Poincaré half-plane $\mathcal{H}$ and

$$\{(x, y) \in \mathbb{R}^2 \quad | \quad y > 0\} \tag{2.12}$$

grants us the right to reformulate the energy through $\hat{\varphi}(x, y, \beta) : \mathbb{R}^2 \times \mathbb{R}^+ \to \mathbb{R}$ such that $\hat{\varphi}(x, y, \beta) := \varphi(z, \beta)$. As a consequence, we also adopt a different vocabulary. As (2.9) expresses, the Hessian of the hexagonal member of the energy evaluated in $z = \rho$ is positive-definite. From (2.11) we thus know that β directly decides on the nature of the hexagonal lattice with its sign. When $\beta > 0$, also the Hessian of the total strain energy function evaluated in $z = \rho$ is positive-definite, which implies that $z = \rho$ is a minimum. On the contrary, when $\beta < 0$, $z = \rho$ turns into a maximum. For what concerns the degenerate case $\beta = 0$, this makes the energy relapse into the case of the square energy and transforms the hexagonal point in a monkey-saddle (see Fig. 2.1) as a direct computation later shows. Indeed, when $\beta = 0$ the energy (2.3) loses the term guaranteeing a correct positive-definite behavior in the vicinity of ρ and modular symmetry forces ρ (and its copies) to be a degenerate critical point with a null Hessian, specifically a monkey-saddle.

2.2.2 The square lattice

We now focus on (2.10). On the square lattice configuration, both the square and hexagonal members of the energy act because the modular simmetry is weaker on $z = i$. The analysis of the Hessian of the energy in $z = i$ returns the following about the dependence on β of its eigenvalues λ_1 and λ_2:

$$\lambda_1(\beta) = \begin{cases} \geq 0 & \text{if} \quad -3/2 \leq \beta \leq 3/2 \\ < 0 & \text{if} \quad \beta < -3/2 \vee \beta > 3/2 \end{cases} \qquad \lambda_2(\beta) > 0 \quad \forall \beta. \tag{2.13}$$

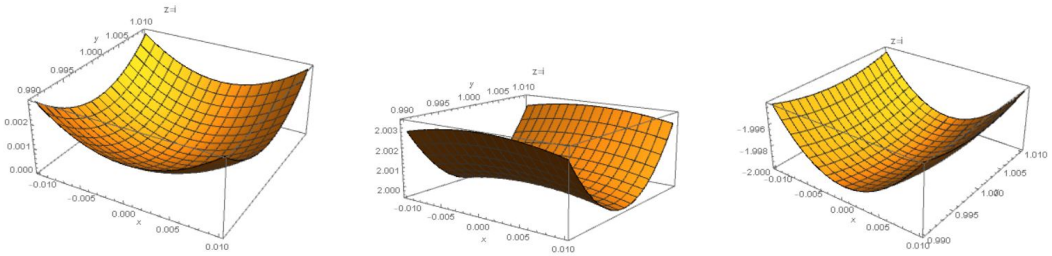

(a) $\beta = 0$ **(b)** $\beta = 2$ **(c)** $\beta = -2$

Figure 2.2: Energy surface in a neighboor of $z = i$ for different values of β. For $\beta = 0$, $z = i$ is a minimum. For $\beta = 2$, $z = i$ is a saddle. For $\beta = -2$, $z = i$ is a saddle.

If we released α from its fixed value, we would obtain that

$$\lambda_1(\beta) = \begin{cases} \geq 0 & \text{if} \quad -3/2\,\alpha \leq \beta \leq 3/2\alpha \\ < 0 & \text{if} \quad \beta < -3/2\alpha \vee \beta > 3/2\alpha \end{cases} \qquad \lambda_2(\beta) > 0 \quad \forall\beta. \tag{2.14}$$

The value $3/2$ is bound to the exponent of the hexagonal energy, which multiplies $\varphi'_{hex}(z)$.
One of the eigenvalues is always positive (see Fig. 2.3 on the next page), hence $z = i$ is never a degenerate critical point for the strain energy function. It is a standard saddle for external values of β with respect to the critical values $\beta_{1,2} = \{-3/2, 3/2\}$ and a minimum for internal values. When β attains its first critical value $\beta = 3/2$, $z = i$ is already a saddle, because the role of minimum is covered by $z = \rho$. When $\beta = -3/2$, $z = i$ is still entrusted with being a point of absolute minimum for the energy, i.e. a minimum; indeed $z = \rho$ is a maximum (see Fig. 2.2). It will be interesting to observe what happens when both $z = i$ and $z = \rho$ are instable.
Thus, the position of the absolute minimum of the strain energy function exhibits a discontinuity with respect to β, which is a thermodynamic variable with a connection to temperature yet to be defined. We can legitimately label the ongoing phenomenon as a first-order phase transition (see Fig. 2.4 on the next page).

2.3 The energetic landscape

Even though the model contains only one free parameter, $z = i$ and $z = \rho = e^{i\pi/3}$ assume several different configurations. The energetic landscape which generates according to the value of β is rather colourful; basins transform into peaks, favorable passages need to be found elsewhere.
If we think about the Poincaré half-plane $\mathcal{H}$ as the domain where the energy landscape develops, it is quite clear that points different to $z = i$ and $z = \rho$ will also represent relevant morphological elements as the elevations change and move. This could be observed already in a 2D-setting as the one of Fig. 2.4 on the following page (observe for instance that when $\beta = -2$ the energy has an other relative minimum beyond the hexagon).
We searched for further stationary points along the geodetic lines connecting

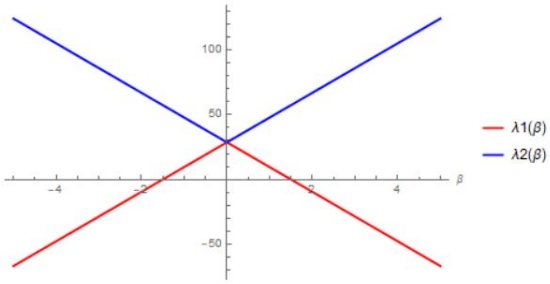

Figure 2.3: Eigenvalues of the Hessian matrix of the strain energy function evaluated in $z = i$. λ_2 is strictly positive $\forall\beta$, while λ_1 is strictly positive for $-3/2 < \beta < 3/2$, which is thus the range of values of β where the energy has a minimum in the square lattice. For external values of β, the Hessian is indefinite (non-degenerate) hence $z = i$ is a standard saddle. We will explicitly prove that both eigenvalues linearly depend on β in subsection 2.3.1.

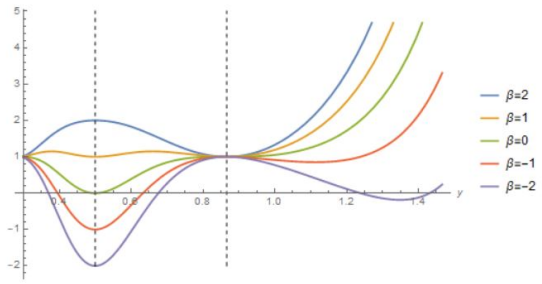

Figure 2.4: Behavior of the strain energy function along the geodetic connecting $z = e^{i\pi/3} = 1/2 + i\sqrt{3}/2$ and $z = 1/2 + i1/2$ for different values of β. $z = 1/2 + i1/2$ represents a square lattice equivalent to i. The x-coordinate is thus fixed, while the y-coordinate changes. Black dashed lines indicate the values of y corresponding to the square and the hexagonal point. This picture represent a first-order phase transitions, restricting β to $\beta \geq \beta_0 = -3/2$. β would be the thermodinamic quantity according to which the equilibrium configurations varies: for $\beta \geq 3/2$ the hexagon is a minimum and the square is unstable, for $0 < \beta < 3/2$ they are both minima (for $1 < \beta < 3/2$ the hexagon is the absolute minimum and the square is a local minimum, viceversa for $0 < \beta \leq 1$), for $-3/2 \leq \beta \leq 0$ the square is a minimum and the hexagon is unstable. When β belongs to the second range, for instance $\beta = 1$, a new stationary point generates between the square and the hexagon; this also happens when β belongs to the third range, for instance $\beta = -1$, but the new stationary point generates between the hexagon and $z = i\infty$. To precisely depict a first-order phase transition we restricted to $\beta \geq -3/2$, because in the fenomenology of this physical event it is not envisaged the new loss of stability of the square lattice for $\beta < -3/2$. This event produces new interesting features discussed later on.

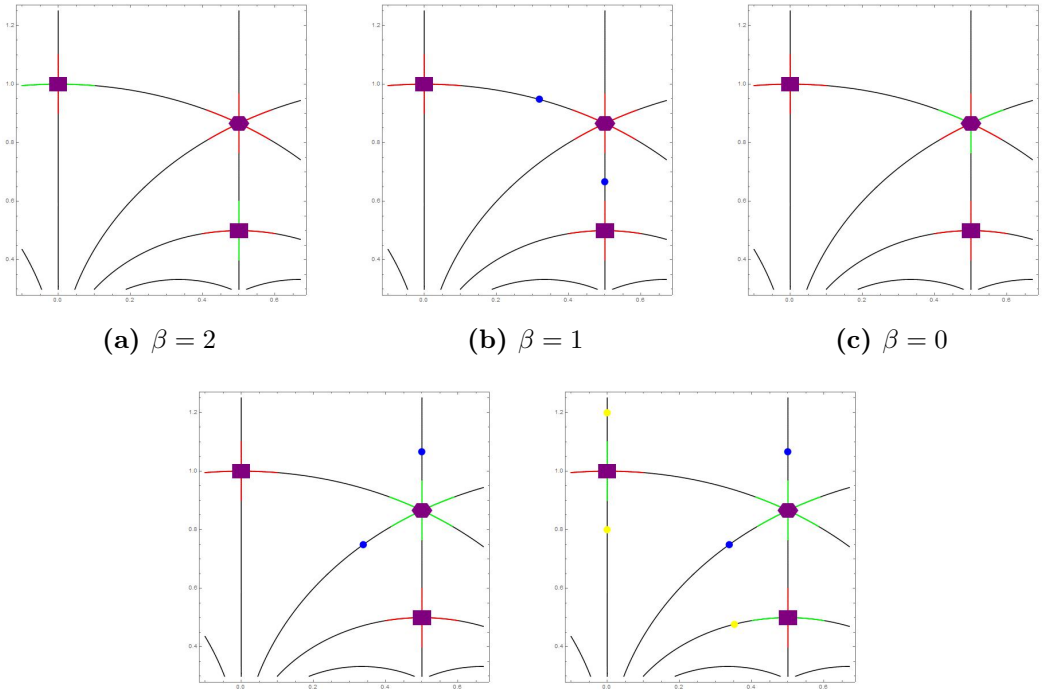

(a) $\beta = 2$ **(b)** $\beta = 1$ **(c)** $\beta = 0$

(d) $\beta = -1$ **(e)** $\beta = -2$

Figure 2.5: A repeated portion of the Poincaré half-plane $\mathcal{H}$. Two equivalent square points ($i, \zeta = 1/2(i+1)$) and one hexagonal point ($\rho = e^{i\pi/3}$) are indicated. Red lines indicate ascent directions, while green lines indicate descent directions. According to the ongoing situation, modified by β, ascent or descent paths leave from ρ, i, ζ. Blue and yellow points represent further stationary points, which correspond respectively to rhombic lattices and rectangular lattices. For instance: in (b) two equivalent stationary points lie on the geodetics connecting the hexagonal point to the square points, as the two ascent directions precisely culminate in a summit.

$z = \rho$ and $z = i$ to the infinity at $z = i\infty$ or at $z = 0$, or those connecting the two maximally-simmetric points themselves (see Fig. 2.5). The geodetic lines respectively connecting i to $z = i\infty$ and ρ to $z = i\infty$ both belong to the fundamental domain $\mathcal{D}$ (see (1.29)). The third part of the boundary of $\mathcal{D}$ precisely connects i to ρ (this can be parametrized as $\{x = \cos\vartheta, y = \sin\vartheta; \vartheta \in [\pi/3, \pi/2]\}$). However, each point on this curve has a suitable copy on the straight segment connecting ζ to ρ:

$$\begin{cases} x = 1/2 \\ y = t \end{cases} \qquad t \in [1/2, \sqrt{3}/2]. \tag{2.15}$$

which can be obtained by subsequently applying the transformations $z \mapsto z + 1$, $\gamma(z)$ and $z \mapsto -1/z$ precisely to this point. The new stationary points are easier to detect by searching on a straight line rather than on a curve; for this reason the research of further stationary points was performed on (2.15).

It turns out that in correspondance with the critical values $\beta_{1,2} = \{-3/2, 3/2\}$ new stationary points bifurcate from the equivalent square points $z = i$, $z = \frac{1}{2}(1+i)$.

This also happens in correspondance with the other critical value $\beta_3 = 0$, crossed by a branch of rhombic unstable lattices generated from the two equivalent hexagonal points $z = \rho = \frac{1}{2}(1 + \sqrt{3})$ and $z = \frac{1}{2}(1 + \frac{\sqrt{3}}{3})$ (this latter can be obtained by applying the usual three transformations in a suitable order) (see Fig. 2.6 on the facing page). Bifurcations will be described more deeply in the following section.
According to $GL(2, \mathbb{Z})$-symmetry, each critical point in the fundamental domain $\mathcal{D}$ has some suitable copies. Even when restricting to a portion of the Poincaré half-plane $\mathcal{H}$ more than one branch of critical points meet each point representing an hexagonal or a square lattice (see Fig. 2.7 on page 34)
In light of these diagrams, we are able to appoint β with a more definite physical meaning. Energy in (2.3) perfectly suits the context of martensitic phase transformations. These latter are solid to solid transformations where the lattice changes abruptly at some temperature. Diminishing the temperature the lattice reaches a less symmetrical condition. The hexagonal configuration of the lattice exhibits more simmetries than the square configuration; diminishing β our model thus exactly depicts the passage to a less symmetrical condition. Hence, β is a growing function of the temperature.

2.3.1 Bifurcations analysis

The aim of this section is to give an insight into the bifurcations of critical points which generate from the maximally-symmetric points $z = \rho$ and the equivalent square points $z = i$, $z = \zeta = \frac{1}{2}(1 + i)$.
In order to describe analitically the behavior of the strain energy function and not to work with modular functions, a good strategy is to restrict the analysis to the neighbourhoods of those three points so that it is possible to characterize the stationary points by studying the Taylor expansion of the strain energy in their neighborhoods. We ought to consider the reformulation of the energy which exploits the identification beteween the Poincaré half-plane $\mathcal{H}$ and $\mathbb{R}^2$ $\hat{\varphi}(x, y, \beta) := \varphi(z, \beta)$.
When considering the neighbourhood of $z = i$, we substitute the energy with its Taylor expansion at the fourth-order precisely around $z = i$. We stopped at the fourth-order because we need to capture the behavior of a pinchfork bifurcation which requires at least a third-order expansion, as the system shifts from one to three fixed points. This can be achieved by expanding around $\varepsilon = 0$ the function $f(\varepsilon) = \hat{\varphi}(\varepsilon u, 1 + \varepsilon v)$, where u and v are the displacements from the position $(0, 1)$ on $\mathbb{R}^2$, equivalent to $z = i$ on the Pointcaré half-plane $\mathcal{H}$. This gives us

$$\begin{aligned} f(\varepsilon) = a_1(u^2 + v^2)\,\varepsilon^2(1 - v\varepsilon + (\frac{u^2}{2} - \frac{a_2 u^2}{a_1} + \frac{a_2 v^2}{a_1})\,\varepsilon^2) + \\ \beta\,(1 - \frac{2}{3}(a_1 u^2 - a_1 v^2)\,\varepsilon^2 + (2\,a_1 u^2 v - \frac{2\,a_1 v^3}{3})\,\varepsilon^3 + \\ \frac{1}{9}(-a_1^2 u^4 + 6\,a_2 u^4 + 14\,a_1^2 u^2 v^2 - 36\,a_2 u^2 v^2 - a_1^2 v^4 + 6\,a_2 v^4)\,\varepsilon^4) + o(\varepsilon^5) \end{aligned} \tag{2.16}$$

where

$$a_1 = 49152\pi^4/\Gamma(-1/4)^8 \simeq 14.3678$$

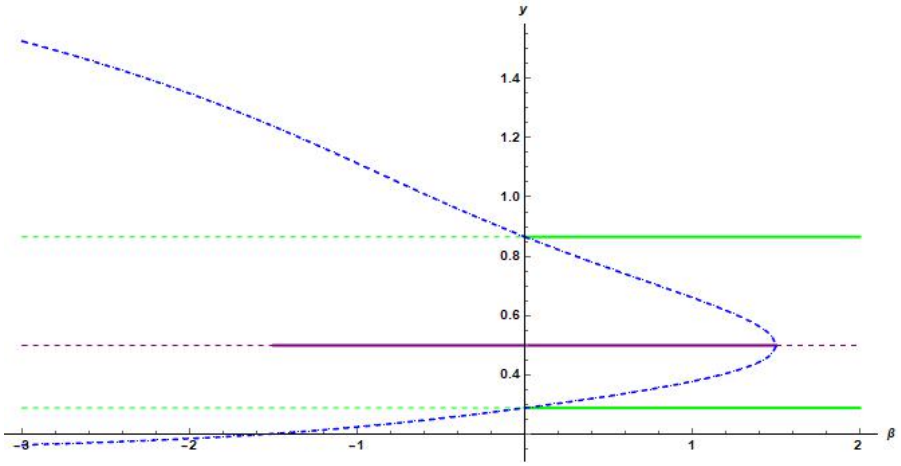

(a) $x = \frac{1}{2}$

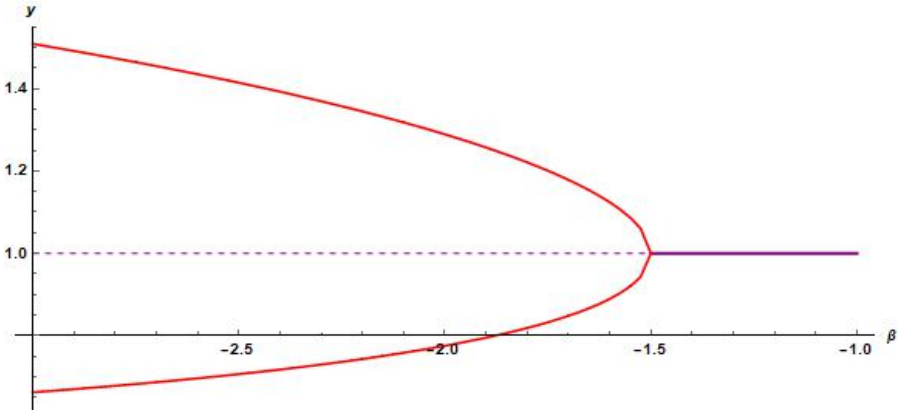

(b) $x = 0$

Figure 2.6: Bifurcation diagrams for the energy (2.3). The bifurcation parameter is β (on the abscissa). Solid and dotted lines indicate stable and unstable critical points. Green and purple lines refer respectively to hexagonal and square points, while blue and red lines refer respectively to rhombic and rectangular points. Figure (a): the three horizontal lines indicate the behavior of the two equivalent hexagonal points and the square point lying on $x = \frac{1}{2}$ (they are $\rho, \tau = 1/2(1 + i\sqrt{3}/3)$ and $\zeta = 1/2(1 + i)$). There is a subcritical pinchfork bifurcation between square and fat rhombic critical points around the critical value $\beta = \frac{3}{2}$. The unstable branches of the bifurcation then cross the hexagonal points turning into skinny rhombic critical points. The slanting blue dotted branches do not have an asymptote for $\beta \to -\infty$ even though their growth is slow. Hence every fat rhombic is eventually a critical point of the energy (2.3). Figure (b): the horizontal line indicates the behavior of the square point $z = i$. There is a supercritical pinchfork bifurcation between square and rectangular critical points around the critical value $\beta = -\frac{3}{2}$. The stable branches of the bifurcation also do not have an asymptote for $\beta \to -\infty$.

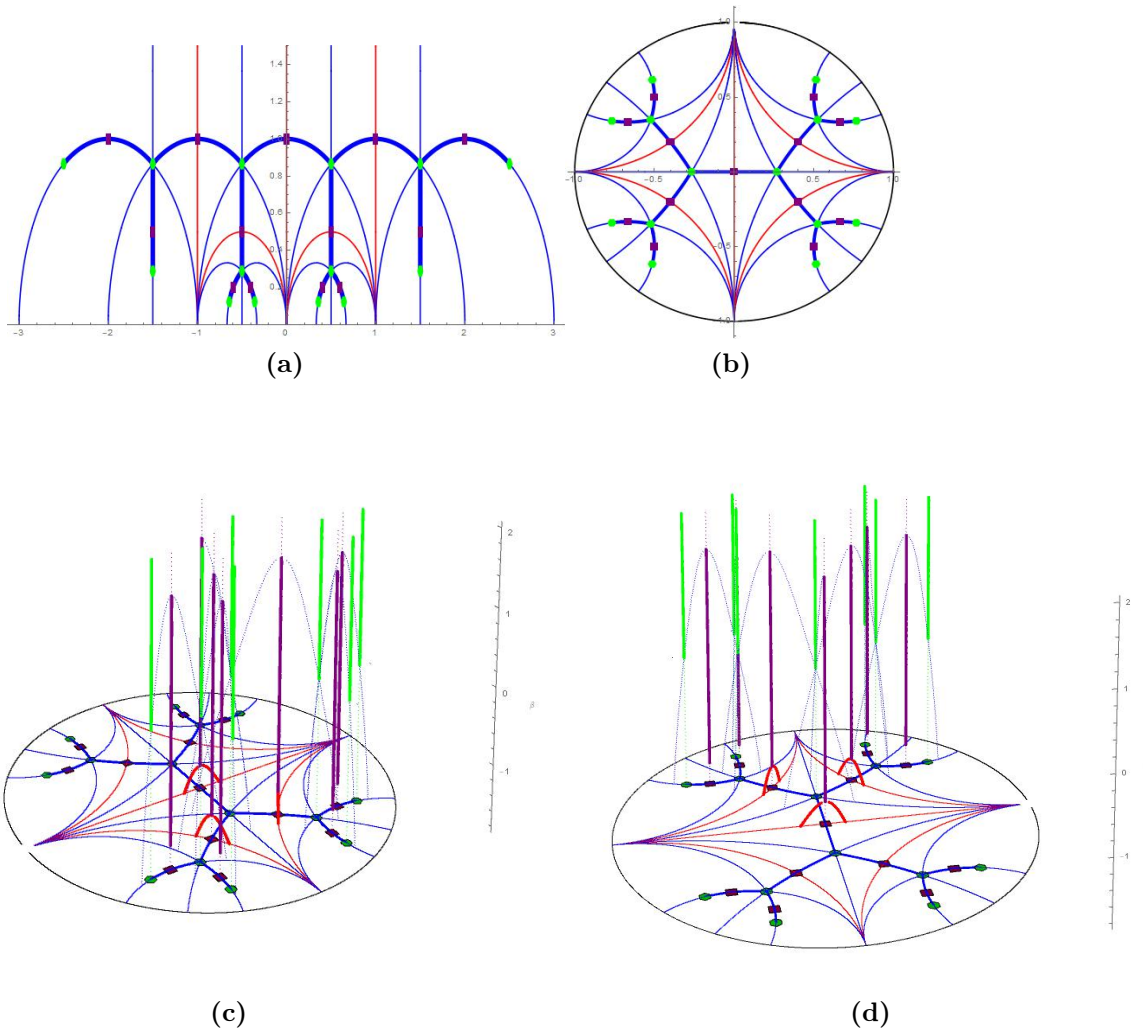

Figure 2.7: Two views of the three-dimensional bifurcation diagram for the energy (2.3) together with the Poincaré half-plane model and the Poincaré disk model (see Video "Rotation of 3D bifurcation diagram" in the Supplementary Material for a detailed view). In particular, (a) shows a tiling of the Poincaré half-plane $\mathcal{H}$ obtained drawing a number of geodesics. Each point lying on the red geodesics corresponds to a rectangular lattice. Each point lying on the blue geodesics corresponds to either a fat or skynny rhombic lattice according to the thickness of the curve (which thus acquires an expressive role). Purple squares and green hexagons respectively indicate equivalent square lattices and equivalent hexagonal lattices. Every feature in (a) maps to the disk model in (b), through the relation $(x, y) \mapsto (2\,x, x^2 + y^2 - 1)/(x^2 + (1 + y)^2)$ where (x, y) is a point in the half-plane model. The 3D bifurcation diagram ((c) and (d)) describes the character of each critical point belonging to one of the halfs of (b) with respect to the bifurcation parameter β which is shown on the vertical coordinate. The basis of the 3D graphic is the disk model and it lies at $\beta = -1.8$. This diagram adopts the graphic conventions of the 2D bifurcation diagrams: green, purple and red solid/dotted lines respectively indicate the stability/instability range of the hexagonal, square and rectangular points while blue dotted lines indicate unstable rhombic critical points. The bifurcations reflect specularly on the other half of the disk model but they are not reported for the sake of readability. For the same reason the tessellation of (a) (thus, also the one of (b)) is incomplete; the picture, however beautiful, would have been mightily tangled (see Fig. 1.5 on page 19).

and

$$a_2 = 4096\pi^4(753664\pi^4 + 27\Gamma(-1/4)^8)/3\Gamma(-1/4)^{16} \simeq 98.7013$$

where Γ is the Euler gamma function.
As expected, the only the 0-th order term of the expansion is β, which is the height of the energy when $z = i$. Furthermore, the quadratic term deriving from the expansion around $z = i$ of the square member of the energy $|J(z) - 1|$ is a convex paraboloid whose vertex is in $(u, v) = (0, 0)$; this term is indeed convex in the neighbourhood of the square lattice. Hence, it is the quadratic term multiplying β which wrecks the stability of $z = i$. The Hessian matrix of the quadratic term of the Taylor expansion is finally

$$\begin{bmatrix} 2\,a_1 - \frac{4}{3}a_1\beta & 0 \\ 0 & 2\,a_1 + \frac{4}{3}a_1\beta \end{bmatrix}. \tag{2.17}$$

Expression (2.17) proves the linear dependence of λ_1 and λ_2 on β (see 2.3 on page 30).
The values of β such that both the eigenvalues of (2.17) are strictly positive are

$$-\frac{3}{2} < \beta < \frac{3}{2} \tag{2.18}$$

as expected.
In order to find critical points around $z = i$, chosing $\varepsilon = 1$, we imposed $\nabla f = 0$ and we obtained three valid solutions

$$\begin{cases} u_1 = 0 \\ v_1 = 0 \end{cases} \tag{2.19}$$

$$\begin{cases} u_2 = 0 \\ v_2(\beta) = \frac{9a_1\,(3+2\beta)+\sqrt{3}\sqrt{a_1\,(3+2\beta)\,(32a_1^2\beta+27a_1\,(3+2\beta)-96a_2\,(3+2\beta))}}{8(-a_1^2\beta+a_2\,(9+6\beta))} \end{cases} \tag{2.20}$$

$$\begin{cases} u_3 = 0 \\ v_3(\beta) = \frac{-9a_1\,(3+2\beta)+\sqrt{3}\sqrt{a_1\,(3+2\beta)\,(32a_1^2\beta+27a_1\,(3+2\beta)-96a_2\,(3+2\beta))}}{8(a_1^2\beta-a_2\,(9+6\beta))} \end{cases}. \tag{2.21}$$

The other solutions found were not to be considered valid because either they were living in the complex domain (u and v need to be real scalar values because they describe displacements).
The three valid solutions share the coordinate $u = 0$, hence critical points scatter just in the y-direction from $z = i$.
The first one is precisely $z = i$ because it describes a zero displacement from the point around which the Taylor series was expanded. (2.19) and (2.20) are the branches of a supercritical pinchfork bifurcation where the critical value of the bifurcation parameter is $\beta = -\frac{3}{2}$ (see Fig. 2.8 on the next page). They are both defined for $\beta \leq -\frac{3}{2}$; any perturbation from $z = i$, which is an unstable position in this range of β, makes the system jump on one of those two branches. When $\beta \to -\frac{3}{2}$

$$v_2(\beta) \sim \frac{\sqrt{(-2a_1)(\beta + \frac{3}{2})}}{a_1} \qquad v_3(\beta) \sim -\frac{\sqrt{(-2a_1)(\beta + \frac{3}{2})}}{a_1}. \tag{2.22}$$

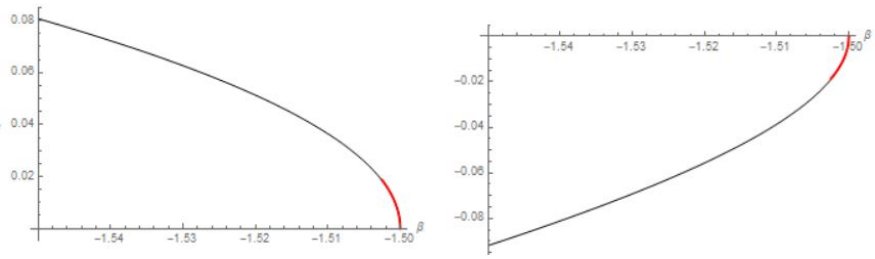

(a) **(b)**

Figure 2.8: The branches of the supercritical bifurcation around $z = i$ described in (2.19), (2.20). Red curves highlights the behavior close to $\beta = -3/2$, i.e. the vertical crossing of the horizontal axis.

They describe analytically how stable rectangles generate from $z = i$ when diminishing β, as represented on Fig. 2.6 on page 33(b).

An analogous procedure has been applied to give an analytical representation of the results in Fig. 2.6 on page 33(a).
Let us consider $z = \zeta = \frac{1}{2}(1 + i)$. In this case we expanded at the fourth order, around $\varepsilon = 0$, $f(\varepsilon) = \hat{\varphi}(\frac{1}{2} + \varepsilon u, \frac{1}{2} + \varepsilon v)$ and we obtained

$$\begin{aligned} f(\varepsilon) = b_1(u^2 + v^2)\,\varepsilon^2(1 - \frac{b_2 v\,\varepsilon}{b_1} + \frac{(b_2^2\ u^2 + 2b_1 b_3\ u^2 - 2b_1 b_3\ v^2)\,\varepsilon^2}{2b_1^2}) + \\ \beta\ (1 + \frac{2}{3}(b_1 u^2 - b_1 v^2)\,\varepsilon^2 + (-2b_2\ u^2 v + \frac{2b_2 v^3}{3})\,\varepsilon^3 + \\ \frac{1}{9}(-b_1^2 u^4 + 6b_3\ u^4 + 14\ b_1^2 u^2 v^2 - 36\ b_3 u^2 v^2 - b_1^2 v^4 + 6b_3 v^4)\,\varepsilon^4) + o(\varepsilon^5) \end{aligned} \tag{2.23}$$

where $b_1 \simeq 4\,a_1$, $b_2 \simeq 8\,a_1$, $b_3 \simeq 1234.3944$. Being ζ a square point equivalent to i, expression (2.16) and (2.23) can be related; the change in the coefficients b_1, b_2, b_3 can be explained in terms of the metric (1.20) with which the Poincaré half-plane $\mathcal{H}$ is endowed.
ζ is a square lattice equivalent to $z = i$, thus there the previous remarks about linear term and quadratic terms of the expansion still hold in this case. The Hessian matrix of the quadratic term of the expansion is

$$\begin{bmatrix} 2b_1 + \frac{4}{3}b_1\beta & 0 \\ 0 & 2b_1 - \frac{4}{3}b_1\beta \end{bmatrix} \tag{2.24}$$

which is positive definite for the range of β in (2.18).
Setting $\varepsilon = 0, \nabla f = 0$ gave three valid solutions

$$\begin{cases} u_1 = 0 \\ v_1 = 0 \end{cases} \tag{2.25}$$

$$\begin{cases} u_2 = 0 \\ v_2(\beta) = -\frac{-9b_2\,(-3+2\beta) + \sqrt{3}\sqrt{(-3+2\beta)\,(27b_2^2(-3+2\beta) - 32b_1\,(9b_3 + b_1^2\beta - 6b_3\beta))}}{8(b_1^2\beta + b_3\,(9-6\beta))} \end{cases} \tag{2.26}$$

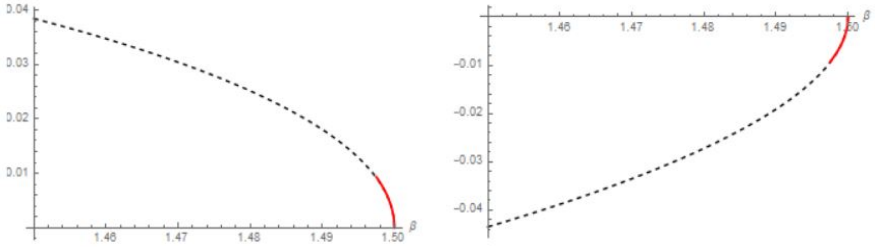

(a) (b)

Figure 2.9: The branches of the subcritical bifurcation around $z = \zeta$ described in (2.26), (2.27). Red curves highlights the behavior close to $\beta = 3/2$, i.e. the vertical crossing of the horizontal axis.

$$\begin{cases} u_3 = 0 \\ v_3(\beta) = \frac{9b_2\,(-3+2\beta)+\sqrt{3}\sqrt{(-3+2\beta)\,(27b_2^2(-3+2\beta)-32b_1\,(9b_3+b_1^2\beta-6a_3\beta))}}{8(b_1^2\beta+b_3\,(9-6\beta))} \end{cases} . \tag{2.27}$$

The first solution is precisely $z = \zeta$. The second and the third solution are the branches of a subcritical pinchfork bifurcation where the critical value of the bifurcation parameter is now $\beta = \frac{3}{2}$ (see Fig. 2.9). The branches are the instable saddles which generate from the square lattice corresponding to $z = \zeta$ which are represented in Fig. 2.6 on page 33(a). They are defined for $\beta \leq \frac{3}{2}$. For this range of β, $z = \zeta$ is stable. The two unstable branches toghether with the stable branch represented by the first solution will collapse to produce one unstable branch when $\beta > \frac{3}{2}$. When $\beta \to \frac{3}{2}$

$$v_2(\beta) \sim -\frac{\sqrt{(-2b_1)(\beta-\frac{3}{2})}}{b_1} \qquad v_3(\beta) \sim \frac{\sqrt{(-2b_1)(\beta-\frac{3}{2})}}{b_1}. \tag{2.28}$$

Finally, let us consider $z = \rho = e^{i\pi/3}$. Expanding $f(\varepsilon) = \hat{\varphi}(\frac{1}{2}+\varepsilon u, \frac{\sqrt{3}}{2}+\varepsilon v)$ at the fourth order around $\varepsilon = 0$

$$\begin{aligned} f(\varepsilon) = 1 + (-3c_1u^2v + c_1v^3)\,\varepsilon^3 + (-c_2u^4 + 6c_2u^2v^2 - c_2v^4)\varepsilon^4 + \\ c_1^{2/3}(u^2+v^2)\beta\,\varepsilon^2(1 - \frac{2c_2v\,\varepsilon}{3c_1} + \frac{(3c_2^2u^2 - 6c_1c_3u^2 - c_2^2v^2 + 6c_1c_3v^2)\,\varepsilon^2}{9c_1^2}) + o(\varepsilon^5) \end{aligned} \tag{2.29}$$

where

$$c_1 = J'''(\rho)/6 \simeq 26.4728$$

and $c_2 \simeq 45.8523$, $c_3 \simeq 52.9457$ (these latter being rather complex expressions obtained combining higher order derivatives of the Klein Invariant J).
The only 0-th term is 1, which is precisely the height of the strain energy function when $z = \rho$. The only quadratic term is

$$c_1^{2/3}(u^2+v^2)\beta \tag{2.30}$$

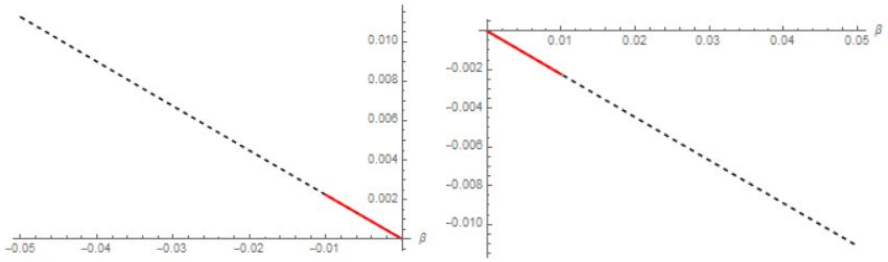

(a) **(b)**

Figure 2.10: The sloped branches of the bifurcation around $z = \rho$ described in (2.33). Red lines highlights the behavior close to $\beta = 0$, i.e. a slenting crossing of the horizontal axis.

which is a convex paraboloid with center in $(u, v) = (0, 0)$ when $\beta > 0$ and non convex when $\beta < 0$. When $\beta = 0$, the quadratic term disappear and it remains the third-order term, which defines as expected a monkey-saddle

$$c_1(-3\,u^2 v + v^3). \tag{2.31}$$

In order to recover the analytical description of the transversal crossing of the rhombic branch in Fig. 2.6 on page 33(a) we looked again at the solutions of $\nabla f = 0$. We obtained

$$\begin{cases} u_1 = 0 \\ v_1 = 0 \end{cases} \tag{2.32}$$

$$\begin{cases} u_2 = 0 \\ v_2(\beta) = -\dfrac{-9c_1^{4/3} + 6c_2\,\beta + c_1^{1/3}\sqrt{\dfrac{81c_1^{8/3} + 180c_1^{4/3}c_2\,\beta + 68\,c_2^2\,\beta^2 - 192c_1c_3\beta^2}{c_1^{2/3}}}}{8(cb_1^{4/3}c_2 + c_2^2\,\beta - 6c_1c_3\,\beta)} \end{cases} . \tag{2.33}$$

The first solution is precisely $z = \rho$. The second one is the analytical description of the transversal crossing of the rhombic branch (see Fig. 2.10). The displacement in the horizontal direction u is 0 because rhombic critical points are on the straight geodetic where also $z = \rho$ lies. When $\beta \to 0$

$$v_2(\beta) \sim -\frac{2}{3c_1^{1/3}}\beta \tag{2.34}$$

which is a decreasing straight line as expected.

2.4 Energy barriers

What we have seen so far is every feature that could be predicted through the proposed potential when varying its only free parameter β, which is an increasing function of the temperature. Bifurcation diagrams thus depict the reaction of the body to the change of temperature when the interpretation of its distorsive behavior is entrusted to the strain energy function in (2.3).

We finally want to address transformations that do not imply a change in temperature, setting our model in the domain of cold mechanics and exploring crystal elasto-plasticity. A particularly meaningful data in this field is undoubtedly the yield strenght that marks the frontier between reversible elastic behavior and irreversible plastic behavior. Its significance is also bound to the fact that its value can be easily obtainable through experimental tests. Adopting the energetic language, it emerges that the yield strenght is related to the energy barriers existing between two adjacent equilibrium configurations.
In these circumstances we define as adjacent equilibrium configurations points such that one can be obtained as the image of the other through some $SL(2,\mathbb{Z})$-tensors, hence they live in two copies of the fundamental domain sharing a portion of the boundary. In this way, we can explore the plastic domain.
A tranformation that could be constructed with some $SL(2,\mathbb{Z})$-tensors is $z \mapsto z+1$. This tranformation together with $z \mapsto -1/z$ descend from the matrices that span $SL(2,\mathbb{Z})$ group. We have already proven that $z \mapsto z+1$ corresponds to a simple shear in subsection (1.2.1).

2.4.1 Simple shear from i to $i+1$

In this chapter we first investigated which is the energetically optimal barrier-crossing path from i to $i+1$ for each value of β. This is the transformation also considered in the following numerical simulations. Since we want to consider i and $i+1$ as adjacent equilibrium configurations, we need to restrict the range of β to the values that actually guarantee that those points remain minima: $-3/2 \leq \beta < 3/2$. Furthermore, since the energetic landscape can vary significantly with β as we saw previously, we need to define the energy barrier

$$\Delta E_{best}(\beta) = \min_{\forall paths} \max_{z \in path} \varphi(z,\beta) - \min_{z \in path} \varphi(z,\beta). \tag{2.35}$$

For every value of β we choose the path from i to $i+1$ guaranteing a passage across the lowest among the summits. Taking this road, it could happen to encounter equilibrium configurations other than $i+1$ that for some values of β represent the absolute minimum for the strain energy function, being $i+1$ just a relative minimum. Once we chose the path, under the last clarification, the computation of the energy barrier for every value of β becomes obviously the difference between the maximum and the minimum along this path (see Fig. 2.11 on the following page)

2.4.2 Simple shear and prerotation of rectangular lattices

Our energetic model contains a supplementary information with respect to the expected minima. There is a range of β, $\beta < -3/2$, where equilibrium configurations move into rectangular lattices while both hexagonal and square lattices lose stability. The rectangles generate above and under $z = i$, bifurcating towards the geodetics that connect the square lattice to infinity.
In this section, we investigated the energy barriers between rectangular equilibrium

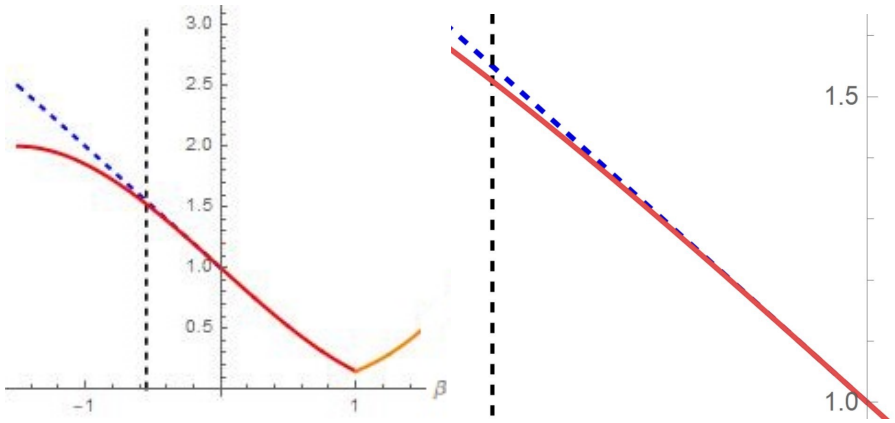

(a) **(b)**

Figure 2.11: (a) Energy barrier of the simple shear from i to $i+1$ for each value of β. For $-3/2 \leq \beta < 1$ (red line), the absolute minimum of (2.3) is the square lattice. For $1 < \beta < 3/2$ (orange line), the square lattice is a relative minimum and the hexagonal lattice is the absolute minimum, because $\alpha = 1 < \beta$. For $\beta = 1$, the value of the energy is the same for both square and hexagonal lattice.
For $0 \leq \beta < 3/2$ the energetically optimal path from i to $i+1$ goes throughout the geodetic connecting i to the hexagon lattice $z = e^{i\pi/3}$ and then throughout the one connecting $z = e^{i\pi/3}$ to $i+1$; here the summits to cross are the two equivalent fat rhombic saddles which generate along the two geodetics. For $-3/2 \leq \beta < 0$, above $z = e^{i\pi/3}$ skinny rhombic saddles generate. Thus, two passageways to get to $i+1$ could be possible. The first is the one consisiting in the previous geodetics, which involves crossing the maximum in the hexagon lattice $z = e^{i\pi/3}$ (blue dotted line is the energy barrier for this passageaway). The second is the one through the corridor of rhombic saddles, whose energy barrier is represented through the red line. From the zoom in (b) it can be observed that the corridor of rhombic saddles is more convenient. In the neighbourhood of $\beta \simeq -0.55$ (dashed black line) to lower values of β, this becomes more evident. It is interesting to observe that at this value of β the skinny rhombic saddle that creates above the hexagon corresponds to $z = 1/2 + i$, hence it lies on the same straight horizontal line as i. On the other hand, when the skinny rhombic saddle is sufficiently far from the hexagonal point (as it is in this case) this latter can be considered as a proper maximum. Indeed when $\beta = 0$ $z = e^{i\pi/3}$ is a monkey-saddle; when β slightly decreases still remaining in the close neighbourhood of 0, ρ is not a exactly a maximum yet but it can be considered as a deformed monkey saddle encircled by three equivalent skinny rhombic saddles, i.e. a monkey area through which it might not be so inconvenient to pass across to get to $i+1$ from i. At the critical value $\beta = 0$ the skinny rhombic saddles merge into the monkey-saddle in ρ.

configurations that can be said to be adjacent in the sense explained in the introduction of subsection (2.4). In particular, we compared the minimum energetic costs of moving from one minimum to the neighboring one required in the previously mentioned tranformation $z \mapsto z+1$ with respect to the tranformation $z \mapsto -\frac{1}{z}$, which can be proven to correspond to a $\frac{\pi}{2}$-prerotation as we did in subsection (1.2.1) (see Fig. 2.12 on the next page). When $\beta < -3/2$ the energetic landscape involves skinny rhombic saddles above $z = e^{i\pi/3}$, which form the energetically optimal barrier-crossing path when moving from a rectangular lattice z_0 to its tranformed $z_0 + 1$. On the other hand, the transformation $z_0 \mapsto -\frac{1}{z_0}$ entails crossing the saddle in $z = i$ (the picture could be clarified when looking at Fig. 2.5 on page 31 (e)). Plotting the energy barrier of the transformation $z_0 \mapsto z_0 + 1$ leads us to formulate what follows. In this case the energy barrier is for each value of β

$$\Delta E_{best}(\beta) = \varphi(z_{rhombi}(\beta), \beta) - \varphi(z_{rectangles}(\beta), \beta). \tag{2.36}$$

It emerges that

$$\Delta E_{best}(\beta) = \varphi(z_{rhombi}(\beta), \beta) - \varphi(z_{rectangles}(\beta), \beta) = k \tag{2.37}$$

where k is a constant value $k = 2$. Exploiting the identification between Poincaré half-plane $\mathcal{H}$ and $\mathbb{R}^2$, we reformulate $\hat{\varphi}(x, y, \beta) := \varphi(z, \beta)$. Since for each value of β the rectangular minimum and the rhombic saddle are always respectively on the straight lines $x = 0$ and $x = 1/2$, the dependence on β only acts on the y-coordinate. It follows that

$$\hat{\varphi}(x_{rhombi}, y_{rhombi}(\beta), \beta) - \hat{\varphi}(x_{rectangles}, y_{rectangles}(\beta), \beta) = k \tag{2.38}$$

which implies, differentiating with respect to β

$$\begin{aligned} &\frac{\partial \hat{\varphi}}{\partial y}(x_{rhombi}, y_{rhombi}(\beta), \beta) + \frac{\partial \hat{\varphi}}{\partial \beta}(x_{rhombi}, y_{rhombi}(\beta), \beta) = \\ &\frac{\partial \hat{\varphi}}{\partial y}(x_{rectangles}, y_{rectangles}(\beta), \beta) + \frac{\partial \hat{\varphi}}{\partial \beta}(x_{rectangles}, y_{rectangles}(\beta), \beta). \end{aligned} \tag{2.39}$$

Since rectangles and rhombi are stationary points for the strain energy function, the derivative with respect to y evaluated in these points is zero. Hence

$$\frac{\partial \hat{\varphi}}{\partial \beta}(x_{rhombi}, y_{rhombi}(\beta), \beta) = \frac{\partial \hat{\varphi}}{\partial \beta}(x_{rectangles}, y_{rectangles}(\beta), \beta). \tag{2.40}$$

Since we can divide the strain energy functon in its two members

$$\hat{\varphi}(x, y, \beta) = \hat{\varphi}_{square}(x, y, \beta) + \beta\, \hat{\varphi}_{hex}(x, y, \beta) \tag{2.41}$$

it is immediate to differentiate with respect to β, obtaining that

$$\hat{\varphi}_{hex}(x_{rhombi}, y_{rhombi}(\beta)) = \hat{\varphi}_{hex}(x_{rectangles}, y_{rectangles}(\beta)). \tag{2.42}$$

Substituting the expression of the hexagonal member of the energy we obtain that

$$|J(x_{rhombi} + i\, y_{rhombi})|^{2/3} = |J(x_{rectangles} + i\, y_{rectangles})|^{2/3}. \tag{2.43}$$

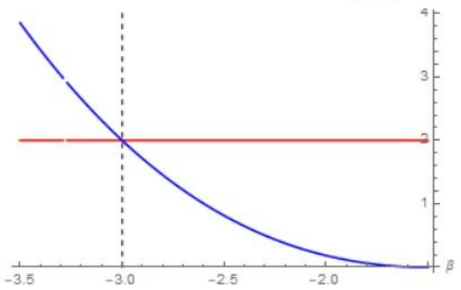

Figure 2.12: Energy barrier for each value of β of two transformations $z_0 \mapsto z_0 + 1$ (red line), $z_0 \mapsto -\frac{1}{z_0}$ (blue curve), where z_0 is the rectangle that generates above $z = i$ at the current β-value. For the first case, the energy barrier is constant $\Delta E_{best} = 2$. When $\beta = -3$ (dashed black line), the transformation $z_0 \mapsto z_0 + 1$ becomes more energetically convenient.

The evaluation of Klein Invariant J in rhombic points gives always a real negative value, while the evaluation of Klein Invariant J in rectangular points gives always a real positive value. Hence, raising to the power of 3/2 both members

$$-J(x_{rhombi} + i\, y_{rhombi}) = J(x_{rectangles} + i\, y_{rectangles}) \tag{2.44}$$

The last expression implies that, when $\beta < -3/2$, the minima of the strain energy function (rectangular lattices) and the skinny rhombic saddles, which form the energetically optimal passageaway to reach a translated domain, give opposite values of the Klein Invariant J. On the other hand, the rectangle that generates above $z = i$ for each value of β have the same height on the Poincaré half-plane $\mathcal{H}$ of the rhombus that generates above the hexagon $z = e^{i\pi/3}$ provided that β is distant enough from $\beta = -3/2$ (see Fig. 2.13 on the next page).

A second interesting observation which emerges from the comparison of the energy barriers of the two transformations is that there exists a value of β such that the transformation $z_0 \mapsto -\frac{1}{z_0}$ becomes more energetically expensive than the transformation $z_0 \mapsto z_0 + 1$. This value is $\bar{\beta} = -3$ (see Fig. 2.12). When β decreases, each minimum that generates above $z = i$ is more and more deformed, getting closer to $z = i\infty$. Since there exists the value $\bar{\beta}$, we can infer that, when the rectangular lattice is deformed enough, the best adjacent equilbrium configuration for the strain energy function turns the lattice into a parallelogram rather than into a $\frac{\pi}{2}$-prerotated rectangle. In order to quantify such critical deformation, we computed the aspect ratio of the rectangular critical point that generates above (and, in a specular manner, below) $z = i$ for each value of β.
The aspect ratio is a parameter that can be easily computed when considering the deformation gradient needed to turn a 2D-square into a 2D-rectangle, whose basis measure is α and height measure is $\frac{1}{\alpha}$. The aspect ratio is the ratio between the basis and the height

$$AR = \frac{\alpha}{\frac{1}{\alpha}} = \alpha^2. \tag{2.45}$$

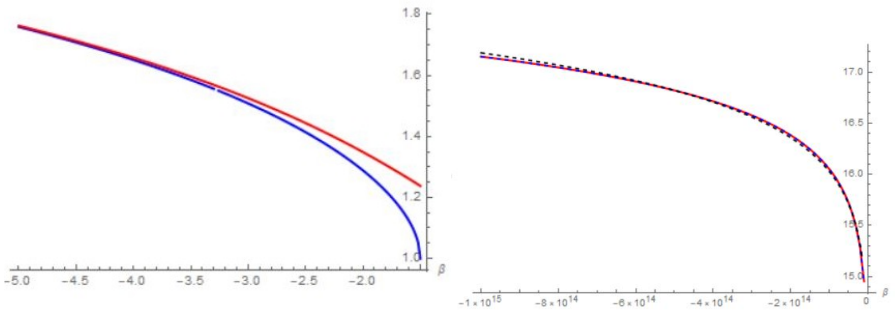

(a) **(b)**

Figure 2.13: (a) y-coordinate of rectangular lattices and rhombic lattices. The red curve represents the variation of y-coordinate of rhombic critical points above $z = e^{i\pi/3}$ with respect to β. The blue curve represents the variation of y-coordinate of rectangular critical points above $z = i$ with respect to β. The two curves coincide after a transient zone. The delay is due to the fact that rhombic points reaches the height of $1 + \delta$, i.e. the height of the first rectangle that generate above $z = i$, for $\beta = -0.55 - \varepsilon$ while the first rectangle generates for $\beta = -3/2 - \varepsilon$, where ε and δ are two arbitrarily small quantities. As already mentioned in 2.6 on page 33, when $\beta \to -\infty$ both curves (which eventually correspond) do not have an asymptote. (b) y-coordinate of rectangular and rhombic lattices when $\beta \to -\infty$. Color conventions are the same as (a); the blue curve is now dashed for the sake of graphical decipherability. Black dashed curve represents $y(\beta) = (-\beta)^{\frac{1}{n}}$, where $n = 16$; this is a function that approximately reproduce the trend of both curves to $-\infty$. It does not converge to a finite limit when $\beta \to -\infty$.

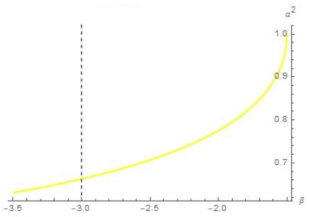

Figure 2.14: Variation of the aspect ratio of rectangular points above and below $z = i$ with respect to β. The black dashed line indicates the value of β below which the transformation $z_0 \mapsto z_0 + 1$ is energetically more convenient than $z_0 \mapsto -\frac{1}{z_0}$. The corresponding α^2 is 0.663.

The deformation gradient is

$$\mathbf{F} = \begin{bmatrix} \alpha & 0 \\ 0 & \frac{1}{\alpha} \end{bmatrix}. \tag{2.46}$$

Since $\mathbf{F}$ is diagonal, the right Cauchy-Green deformation tensor is then

$$\mathbf{C} = \mathbf{F}^T\mathbf{F} = \mathbf{F}^2 = \begin{bmatrix} \alpha^2 & 0 \\ 0 & \frac{1}{\alpha^2} \end{bmatrix}. \tag{2.47}$$

Thanks to the already mentioned Cauchy-Born hypothesis, $\mathbf{C}{=}(C_{ij})$ corresponds to a metric that is in a one-to-one correspondance with a point in the Poincaré half-plane $\mathcal{H}$ through the relation

$$z(\mathbf{C}) = \frac{C_{12}}{C_{11}} + i\frac{\sqrt{\det\mathbf{C}}}{C_{11}} = i\frac{1}{\alpha^2} = \begin{cases} > i & \text{if } -1 < \alpha < 1 \\ < i & \text{if } \alpha > 1 \vee \alpha < -1 \end{cases}. \tag{2.48}$$

Hence, in order to find the aspect ratio of each rectangle it is sufficient to take the reciprocal value of its y-coordinate on the Poincaré half-plane $\mathcal{H}$(see Fig. 2.14). We found that the aspect ratio corresponding to $\bar{\beta}$ is $\bar{\alpha} \simeq 0.663$.

Chapter 3

A model for weak phase tranformations

This chapter is devoted to presenting a second model for a strain energy function with two pre-assigned minimizing lattices z_0 and z_1. These lattices are now chosen in order to discuss martensitic (or solid-solid) phase transformations of the weak type, which make them reversible as it is explained in both the introduction and the second chapter of the thesis. As we discussed in subsection 1.1.1 of the first chapter, the natural domains of these transformations are Ericksen-Pitteri neighbourhoods. As a matter of fact symmetry-breaking (or weak) tranformations demand to consider two lattices such that one has a higher crystallographic symmetry than the other and the symmetry groups of both the parent and product phase are included in a common finite symmetry group. The first one describes the crystallographic structure of the austenite phase, while the second one the crystallographic structure of the martensite phase. In particular, shape memory effect requires an austenite whose symmetry is cubic, a martensite whose symmetry is a subgroup of the cubic and a volume-preserving transformation.
In a 2D-setting as the one where we operate we choose the square lattice to model the austenite phase and the rhombic lattice to model the martensite phase (we do not reduce to the least symmetrical oblique type but we preserve some simmetry also when the solid is exploring the martensitic phase). Thus, the metrics of the inital, final and any intermediate states belong to the EPN of the square-lattice metric.
As it is explained in the first chapter (section 1.2.1), the action of $GL(2,\mathbb{Z})$-group on the Poincaré half-plane $\mathcal{H}$, which parametrizes the strain space, generates the Dedekind Tessellation; $\mathcal{H}$ is made up of mutually congruent copies of the fundamental domain $\mathcal{D}$, whose boundary $\partial\mathcal{D}$ accomodates points representing metrics possessing nontrivial symmetries. As for the previous model z_0 and z_1 both live on $\partial\mathcal{D}$: $z_1 = i$, while z_0 is either a generic fat rhombic lattice, which lies along the geodetic connecting i and the hexagonal lattice $z = \rho = e^{i\frac{\pi}{3}}$ or a generic skinny lattice, which lies along the geodetic connecting ρ to $z = i\infty$.
The first section of this chapter discusses the conception of the explicit expression of an energy density that complies with the modelling of weak phase tranformations. In particular the choice of the two minima makes the model suitable to represent the behavior of shape memory alloys. Furthermore, by considering the temperature

as a fixed parameter this model is also suitable to represent the phenomenon of superelasticity, which has been illustrated in the introduction of the thesis.
The next sections analyze the mathematical implications of the chosen expression. The second section explores the energetic landscape with all its relevant features at a fixed temperature. In particular, subsection (3.2.2) investigates the character of the hexagonal lattice according to all possible combinations of the free parameters of the energy model.
The third section is devoted to exploring the energy barriers between adjacent equilibrium configurations.
In the fourth section we investigate the morphological features of the energy landscape imposed by our model at high and low temperatures when one single phase between austenite and martensite is stable.
In the last section we investigate the formalization of the optimal paths which connect the critical (stationarity) points of the energy landscape through a further perspective offered by theoretical chemistry.

3.1 Three-parameters model

The Klein Invariant J is the main instrument used to construct a model for the strain energy function because of its representativeness among modular functions. Its characteristic behavior at the corners of the fundamental domain $\mathcal{D}$ was exploited to generate a rather simple but still accurate model reconstructive phase transformations, as the one presented in the previous chapter.
Now, we are partially moving from the corners; the energy that we want to derive needs to have a minimum at one corner of the fundamental domain, $z = i$, and at a point of the boundary $z = z_0$, which is not a stationary point for J (unlike $z = i$, for which it holds $J'(i) = 0$). This latter detail entails that we need to impose a further requirement on the model as we will show hereinafter, which suggests how the analytical picture gets more complicated.
Two parameters are used to control the height of the energy at the stationary points; they reduce to one, by speaking of relative height, which directly relates to temperature. One extra parameter is used to impose $\varphi'(z_0) = 0$ (since $J'(z_0) \neq 0$, z_0 is not a stationary point of the energy a priori). A linear combination of the energy that guarantees a unique minimum in $z = i$ (expression (1.56)) and of the one guaranteing a unique minimum in $z = z_0$ (expression (1.45)) is not sufficient anymore. The simplest (in terms of order of the polinomial expressions involved) expression is spontaneously

$$\varphi(z) = \alpha_1|J(z) - 1| + \beta_1|J(z) - J(z_0)|^2 + \alpha_2|J(z) - 1|^2 \tag{3.1}$$

where a priori we do not impose any condition on the sign of the coefficients. However, this obviously plays a role in controlling the behavior of (3.1) at infinity, which will be discussed in the following.
As already mentioned, the conditions to impose are

$$\begin{cases} \varphi(i) = b_0 \\ \varphi(z_0) = b_1 \\ \varphi'(z_0) = 0 \end{cases} . \tag{3.2}$$

First condition in (3.2) implies

$$\varphi(i) = \beta_1 |J(i) - J(z_0)|^2 = \beta_1 |1 - J(z_0)|^2 = b_0. \tag{3.3}$$

Hence

$$\beta_1 := \frac{b_0}{|1 - J(z_0)|^2}. \tag{3.4}$$

Second condition in (3.2) implies

$$.\varphi(z_0) = \alpha_1 |J(z_0) - 1| + \alpha_2 |J(z_0) - 1|^2 = b_1 \tag{3.5}$$

Thus

$$\alpha_2 := \frac{b_1}{|J(z_0) - 1|^2} - \frac{\alpha_1}{|J(z_0) - 1|}. \tag{3.6}$$

Since $J'(i) = 0$, from first expression in (2.5)

$$\varphi'(i) = 0. \tag{3.7}$$

If we label $|J(z) - 1|$ as φ_{sq} and $|J(z) - J(z_0)|^2$ as φ_{rhmb}, (3.1) can be rewritten considering every member separately

$$\varphi(z) = \alpha_1 \varphi_{sq} + \beta_1 \varphi_{rhmb} + \alpha_2 \varphi_{sq}^2. \tag{3.8}$$

Since $J'(z_0) \neq 0$, $\varphi'_{sq}(z_0) \neq 0$. Hence

$$\varphi'(z_0) = \varphi'_{sq}(z_0)(\alpha_1 + 2\alpha_2 \varphi_{sq}(z_0)). \tag{3.9}$$

By explicitely imposing $\varphi'(z_0) = 0$ we obtain

$$\alpha_1 = -2\alpha_2 |J(z_0) - 1|. \tag{3.10}$$

After having substituted the definition of α_2, we obtain

$$\alpha_1 := \frac{2b_1}{|J(z_0) - 1|}. \tag{3.11}$$

The final expression of the energy is then:

$$\varphi(z, b_0, b_1, z_0) = \frac{b_0 |J(z) - J(z_0)|^2}{|1 - J(z_0)|^2} - \frac{b_1 |J(z) - 1|^2}{|J(z_0) - 1|^2} + \frac{2b_1 |J(z) - 1|}{|J(z_0) - 1|}. \tag{3.12}$$

However, this proposal for the energy strain function needs to be discarded for the following two reasons. First and foremost, by checking the behavior of (3.12) at the extreme borders of the Poincaré half-plane $\mathcal{H}$

$$\varphi(z, b_0, b_1,) \sim \frac{b_0 |J(z) - J(z_0)|^2}{|1 - J(z_0)|^2} - \frac{b_1 |J(z) - 1|^2}{|J(z_0) - 1|^2} \sim \frac{(b_0 - b_1)|J(z)|^2}{|1 - J(z_0)|^2} \quad z \to +i\infty.$$

Thus, in order to guarantee the correct behavior when $z \to +i\infty$, $b_0 > b_1$. This condition lavishly limits the model; recalling that b_0 is the height of the energy in the square lattice and b_1 is the height of the energy in the rhombic lattice, this

latter would never be assigned to the role of absolute minimum.
(3.12) intrinsecally guarantees that $z = i$ and $z = z_0$ are always stationary points. Though, we should also be able to ensure a correct positive-definite behavior of linear elasticity in the vicinity of the minimizers by conveniently combining b_0 and b_1, wherever z_0 is. Let us fix for instance z_0 in order to represent a skinny rhombic lattice $z_0 = \frac{1}{2} + i(\frac{\sqrt{3}}{2} - \delta)$, where $\delta = 0.1$. By numerically computing the Hessian matrix of (3.12) evaluated at $z = i$, after having exploited the identification beteween the Poincaré half-plane $\mathcal{H}$ and $\mathbb{R}^2$, which allows to reformulate $\hat{\varphi}(x, y) := \varphi(z)$, we obtain

$$H_{\hat{\varphi}}(0,1) = \begin{bmatrix} -2\,d\,b_0 + 2\,b_1\,d & 0 \\ 0 & 2\,d\,b_0 + 2\,d\,b_1 \end{bmatrix} \tag{3.13}$$

where $d \simeq 28.664$. By imposing that the eigenvalue $H_{\hat{\varphi}}(0,1)_{1\,1} > 0$, we obtain the condition $b_0 < b_1$ which is contrast with the condition that ensures the correct behavior when $z \to +i\infty$. This second observation hence condemns (3.12) to be discarded.

The previous analysis led us to formulate a model for the energy that contains a further parameter

$$\varphi(z) = \alpha_1|J(z) - 1| + \beta_1|J(z) - J(z_0)|^2 - \alpha_2|J(z) - 1|^2 + \alpha_3|J(z) - 1|^3. \tag{3.14}$$

By applying first condition in (3.2), the result is the same as (3.3). Again

$$\beta_1 := \frac{b_0}{|1 - J(z_0)|^2}. \tag{3.15}$$

The second condition in (3.2) requires that

$$\varphi(z_0) = \alpha_1|J(z_0) - 1| - \alpha_2|J(z_0) - 1|^2 + \alpha_3|J(z_0) - 1|^3 = b_1 \tag{3.16}$$

which implies

$$\alpha_3 := \frac{b_1}{|J(z_0) - 1|^3} - \frac{\alpha_1}{|J(z_0) - 1|^2} + \frac{\alpha_2}{|J(z_0) - 1|}. \tag{3.17}$$

Being $z = i$ stationary in both φ_{sq} and φ_{rhmb}, naturally $\varphi'(i) = 0$ as always. On the other hand, the third condition in (3.2) imposes

$$\varphi'(z_0) = \varphi'_{sq}(z_0)(\alpha_1 - 2\alpha_2\varphi_{sq}(z_0) + 3\alpha_3\varphi^2_{sq}(z_0)) = 0. \tag{3.18}$$

Hence, we obtain an explicit expression for α_2

$$\alpha_2 := -\frac{3\,b_1}{|J(z_0) - 1|^2} + \frac{2\,\alpha_1}{|J(z_0) - 1|}. \tag{3.19}$$

The final energy is

$$\begin{aligned} \varphi(z, b_0, b_1, z_0, \alpha_1) = \frac{1}{|1 - J(z_0)|^3} \big[& \alpha_1\,|1 - J(z_0)|^3\,|1 - J(z)| + \\ & |1 - J(z_0)|\,(3\,b_1 - 2\alpha_1|1 - J(z_0)|)\,|1 - J(z)|^2 + \\ & (-2\,b_1 + \alpha_1|1 - J(z_0)|)\,|1 - J(z)|^3 + \\ & b_0\,|1 - J(z_0)|\,|J(z) - J(z_0)|^2 \big] \end{aligned} \tag{3.20}$$

or, in terms of the unimodular strain $\bar{\mathbf{C}}$:

$$\begin{aligned}\sigma_{d,weak}(\bar{\mathbf{C}}, b_0, b_1, \bar{\mathbf{C}}_0, \alpha_1) = \frac{1}{|1 - J(\hat{z}(\bar{\mathbf{C}}_0))|^3} \big[\alpha_1 \, |1 - J(\hat{z}(\bar{\mathbf{C}}_0))|^3 \, |1 - J(\hat{z}(\bar{\mathbf{C}}))| + \\ |1 - J(\hat{z}(\bar{\mathbf{C}}_0))| \, (3\, b_1 - 2\alpha_1 |1 - J(\hat{z}(\bar{\mathbf{C}}_0))|) \, |1 - J(\hat{z}(\bar{\mathbf{C}}))|^2 + \\ (-2\, b_1 + \alpha_1 |1 - J(\hat{z}(\bar{\mathbf{C}}_0))|) \, |1 - J(\hat{z}(\bar{\mathbf{C}}))|^3 + \\ b_0 \, |1 - J(\hat{z}(\bar{\mathbf{C}}_0))| \, |J(\hat{z}(\bar{\mathbf{C}})) - J(\hat{z}(\bar{\mathbf{C}}_0))|^2 \big]\end{aligned} \tag{3.21}$$

where $\hat{z}$ is (1.21) and $\bar{\mathbf{C}}_0$ is any rhombic-lattice metric. The subscript *weak* indicates weak phase tranformations.
The free parameters of (3.2) are four: b_0, b_1, z_0, α_1. The first two parameters can be reduced to one to represent the relative height of the energy in the two minimizers z_0 and i; this unique free paramer is directly related to temperature.The parameter z_0 is determined by the specific metric of the martenstic phase. It should be noticed that the simple proposed expression does not provide a smooth limit $z_0 \to i$ or $z_0 \to \rho$ to study a second-order phase transition in which the martensitic phase departs continuously from the austenite. Proper energies which deal also with this case can be built from the Klein invariant, but we will not consider them in this context. Thus we exclude i and ρ from the range of possible values for z_0. α_1 is an additional parameter; according to the values of b_0, b_1, z_0, we can describe it as the control knob of some morphological features of the energetic landscape. On the other hand, it must satisfy one condition, which originates from the usual control on the behavior of the energy at infinity

$$\varphi(z, b_0, b_1, \alpha_1) \sim \frac{-2\, b_1 + \alpha_1 |1 - J(z_0)|}{|J(z) - J(z_0)|^3} |1 - J(z)|^3 \quad z \to +i\infty. \tag{3.22}$$

The condition to guarantee that $\varphi(z) \sim +\infty$ when $z \to +i\infty$ is

$$\alpha_1 > \frac{2\, b_1}{|J(z_0) - 1|}. \tag{3.23}$$

It would be too long to discuss the conditions ensuring the conditions to ensure the positive-definite behavior of linear elasticity in the vicinity of the minimizers for all possible values of all the free parameters. In the following sections, however, by choosing some specific, yet generic, values for some parameters, we will show how this analysis can be conducted in general.
The last observation concerns what happens at the hexagonal lattice $z = \rho = e^{i\frac{\pi}{3}}$. Being $z = \rho$ a third-order zero for the Klein invariant J, from (2.5) $z = \rho$ (and its equivalent copies) is not only a spontaneus stationary point for the energy in (3.20) but also a degenerate critical point with a null Hessian, whose order will be determined in the following sections through the Taylor expansion of (3.20) in the neighbourhood of $z = \rho$.

3.2 Critical energetic landscape at the thermodynamic transformation temperature

Fixing the temperature of our model results into fixing the relative height $\frac{b_0}{b_1}$. A meaningful value is $\frac{b_0}{b_1} = 1$. In this case, the height of the energy is the same at both lattices. Adopting the martensitic phase tranformations vocabulary, we call the temperature such that both minimizers have equal energy density the thermodynamic tranformation temperature or simply the transformation temperature (see Battacharya (2004)). Hence, there remain two leftover parameters. z_0 controls the position of the less-symmetrical minimizer, which in our model is etiher a fat or skinny rhombic lattice, mildly or extremely distorted. In other words, z_0 manipulates the extent of the symmetry-breaking property of the weak transformation. The other parameter is α_1, whose role will be clarified later on.
The first necessary observation deals with the convexity of the function in the vicinity of the minimizers. It can be numerically proven that (3.23) and the conditions which ensure the positive-definite behavior around i and z_0 coincide when $b_0 = b_1$. Let us fix for instance again $z_0 = \frac{1}{2} + i(\frac{\sqrt{3}}{2} - \delta)$, where $\delta = 0.1$. Then (3.23) is

$$\alpha_1 > f\, b_1 \tag{3.24}$$

where $f = \frac{2}{|J(z_0)-1|} \simeq 2.066$. On the other hand, numerical results of the Hessian matrix of (3.20) evaluated at $z = z_0$ and $z = i$ give

$$H_{\hat{\varphi}}(\frac{1}{2}, \frac{\sqrt{3}}{2} - \delta) = \begin{bmatrix} f\, b_0 & 0 \\ 0 & f\, b_0 - 3\, f\, b_1 + 2\, \alpha_1 \end{bmatrix} \tag{3.25}$$

$$H_{\hat{\varphi}}(0, 1) = \begin{bmatrix} -f\, h\, b_0 + h\, \alpha_1 & 0 \\ 0 & f\, h\, b_0 + h\, \alpha_1 \end{bmatrix} \tag{3.26}$$

where $h \simeq 28.735$ and $\hat{\varphi}(x, y) := \varphi(z)$ is the usual formulation which exploits the identification between $\mathcal{H}$ and $\mathbb{R}^2$.
Hence, if $b_0 = b_1$, the conditions the ensure that $H_{\hat{\varphi}}(\frac{1}{2}, \frac{\sqrt{3}}{2} - \delta)$ and $H_{\hat{\varphi}}(0, 1)$ are positive-definite both reduce to (3.24). This holds for any choice of z_0 representing a rhombic lattice. Being (3.24) an irrevocable condition (as it controls the behavior of the energy at infinity), this implies that at a fixed temperature both z_0 and i are always relative minima (see Fig. 3.18 on page 73). On the other hand, this comes as no surprise as we expect that both phases are stable when the height of the energy is precisely the same at the two corresponding points, with such a simple form of the energy as the one proposed. We will see in the next sections how the stability of the two phases change when $b_1/b_0 \neq 1$.
As soon as (3.24) is respected, the variation of α_1 thus does not change the character of stationary points. It intervenes on an other morphological aspect of the strain energy function, which will be discussed later. For the moment we can imagine that its value is chosen concurrently with the choice of z_0 arbitrarly in the range of those values respecting (3.24).
The first subsection (3.2.1) deals with the research of all stationary points of the function (3.20) precisely under the hypothesis of equal height in the relative minima i and z_0, i.e. $b_1/b_0 = 1$.

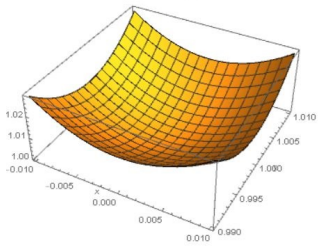

(a) Minimum in $z = i$

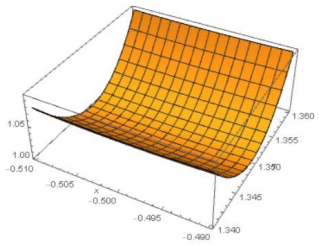

(b) Minimum $z = z_0 = \frac{1}{2} + i(\frac{\sqrt{3}}{2} - \delta)$

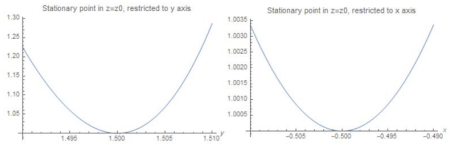

(c) Restrictions on the axes of the minimum $z = z_0 = \frac{1}{2} + i(\frac{\sqrt{3}}{2} - \delta)$

Figure 3.1: Energy surface in the neighbourhood of $z = i$ and $z = z_0$ when $b_1 = b_0 = 1$. The last parameter $\alpha_1 = 10$ was chosen in order to respect (3.24)

The second subsection (3.2.2) discusses the variation of the character of the energy surface (3.20) in the vicinity of the hexagonal point $z = \rho$ according to the different combinations of the free parameters b_0, b_1, z_0, α_1. The hexagonal point is special as its character shows how modular symmetry acts on the topography of the energy surface. The analysis will be rather involved because we are dealing with four control parameters; the subsection thus initally presents the list of aspects which will be treated, in order to hopefully guide the reader through the main steps.

3.2.1 Basins and mountain saddle passes

Since the energetic landscape embraces two relative minima z_0 and i, we expect natural passes to connect them. The area where those basins and elevations form is the Poincaré half-plane $\mathcal{H}$ sectioned in congruent copies of the fundamental domain $\mathcal{D}$. Stationary points of (3.20) are searched all over $\mathcal{D}$ even though it emerges that they tend to arrange along the boundary of $\mathcal{D}$, which is thus the main research path where we look for elevations. The square lattice i lies at one corner of $\mathcal{D}$; the other juction is at the hexagonal lattice forced by modular symmetry to be a degenerate critical point with a null Hessian. A direct computation, whose details will be discussed later, shows that $z = \rho = e^{i\pi/3}$ and its copies are degenerate critical points of order 3 for every choice of z_0, except for one $\bar{z_0} = \bar{x_0} + i\bar{y_0}$ corresponding to a very distorted skynny rhombic lattice. Numerically, it can be found that $\bar{y_0} \simeq 1.326$ when $b_0 = b_1 = 1$. This latter makes them degenerate critical point of order 6. In all other cases $z = \rho = e^{i\pi/3}$ is a monkey-saddle that sits at a bifurcating mountain pass along the symmetry related minimum-to-minimum energetically optimal path (see Fig. 3.2 on the next page). According to which of the paths leaving from $z = \rho = e^{i\pi/3}$ are descent or ascent directions, elevations generate in different points

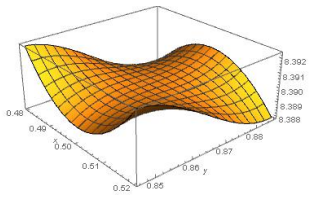

Figure 3.2: Energy surface in the neighbourhood of $z = \rho$ when $b_1 = b_0 = 1$ and $z_0 \neq \bar{z_0}$. The last parameter $\alpha_1 = 10$ was chosen in order to respect (3.24). It represent a typical monkey-saddle surface as a monkey could comfortably seat on it by arranging its legs and tail along the descent directions of the surface.

of the boundaries of $\mathcal{D}$ (see Fig. 3.3 on the facing page). As already mentioned, the position of z_0 is the parameter controlling the nature of ρ, hence whether the paths leaving from it are ascent or descent; eventually it entirely manipulates the morphology of the strain energy function with its peaks and basins (see Fig. 3.4 on page 54). Those elevations forming along the relevant paths connecting the minima turn out to be standard saddles (see Fig. 3.5 on page 55).

3.2.2 The energy surface in the neighbourhood of the hexagonal lattice

Modular symmetry forces the hexagonal points to be degenerate critical points with a null Hessian. This condition does not derive from some particular values of the free parameters of (3.20)$(b_0\,, b_1\,, z_0\,, \alpha_1)$ but it occurs spontaneously because (3.20) was not constructed in order to ensure a convex behavior in the vicinity of ρ, but in the vicinity of i and z_0. This opening statement justifies the temporary neglect of the hypothesis that has guided the previous section $b_0 = b_1 = 1$.
We now want to carefully look at the behavior of (3.20) near ρ, in order to establish the order of this degenerate critical point depending on the values of any free parameter.
As already said, since the possible combinations of the free parameters are many and have many implications (for instance on the correct behavior of the energy at infinity) the discussion around the order of the degenerate critical point ρ turns to be quite involved, hence the relevant steps of the analysis are here presented:

1. It is obtained the Taylor expansion of the potential around ρ by restricting ourselves in the neighbourhood of this point. This expression hides the variety of possible behaviors attainable by the surface in the vicinity of ρ according to the values of the free parameteres $b_0\,, b_1\,, z_0\,, \alpha_1$. This expression is analyzed through the help of a result taken from Peckham (2011); in particular it emerges that ρ is a third order degenerate critical point, i.e. a monkey saddle, for most combinations of the free parameters. However there are some combinations which makes it a sixth order degenerate critical point. The objective of the following steps is precisely to provide the combinations of $b_0\,, b_1\,, z_0\,, \alpha_1$ that transform ρ from a monkey-saddle to a sixth order

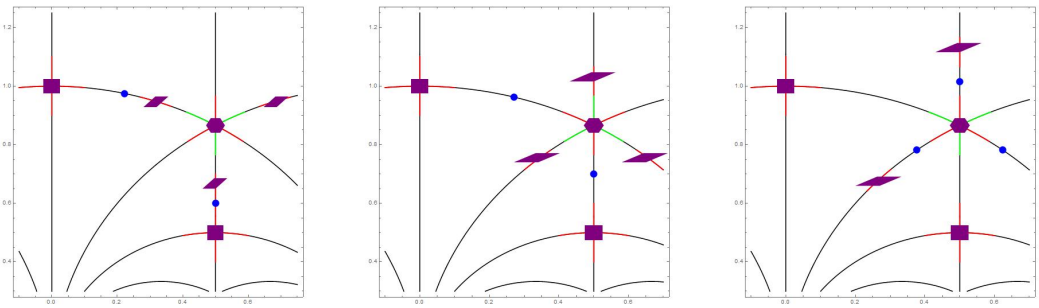

(a) $y_{square} < y_0 < y_{hex}$ **(b)** $y_{hex} < y_0 < \bar{y_0}$ **(c)** $y_0 > \bar{y_0}$

Figure 3.3: A repeated portion of the Poincaré half-plane $\mathcal{H}$. Two equivalent square points ($i, \zeta = 1/2(i+1)$), one hexagonal point ($\rho = e^{i\pi/3}$) and three equivalent rhombic points are indicated. The second relative minimum (besides the square) is located in $z_0 = 1/2 + i\, y_0$ where y_0 belongs to the three different ranges indicated in the caption. The relative minima heights are set to be equal to: $b_0 = b_1 = 1$ while α_1 is chosen in order to respect (3.24) for each considered value of z_0. Red lines indicate ascent directions, while green lines descent directions.
(a) $y_{square} < y_0 < y_{hex}$, i.e. z_0 represents a fat rhombic lattice. The ascent paths leaving from the rhombic minimum and the square minimum meet in saddle points, identified by the blue spots. The hexagonal configuration is a monkey saddle, with three descent directions leading towards the minimizing rhombi.
(b) $y_{hex} < y_0 < \bar{y_0}$ where $\bar{y_0}$ is such that $z = \rho$ is a 6-th order degenerate critical point. z_0 is now a mildly distorted skinny rhombic lattice. Notice that ρ is still a monkey-saddle, but ascent and descent directions interchange with respect to (a). Blue spots indicate fat rhombic standard saddles, which generate at the summit of meeting ascent paths.
(c) $y_0 > \bar{y_0}$, thus z_0 is a very distorted skinny rhombic lattice. Ascent and discent paths leaving from ρ have interchanged again. Blue spots now correspond to skinny rhombic standard saddles; the progressive departure of z_0 from ρ has caused the transfer of those stationary points beyond the hexagon. When $y_0 = \bar{y_0}$ blue spots collide into the 6-th order degenerate point, i.e. $z = \rho$.

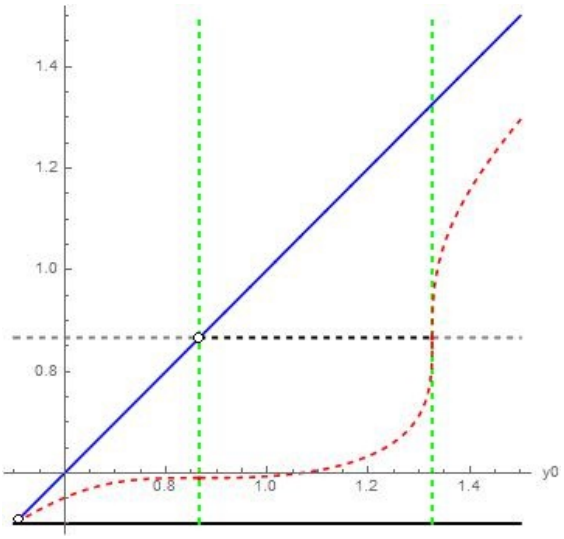

Figure 3.4: Position and character of the stationary points of (3.20) depending on the position of z_0 when $b_0 = b_1 = 1$. α_1 is chosen so that for every choice of z_0, (3.24) is respected. All relevant features of the energy can be represented by points lying on the straight line $x = \frac{1}{2}$. Thus, each curve of the graphic represents the variation of the y-coordinate of the stationary points with a constant $x = \frac{1}{2}$. The black solid horizontal line represents the stable behavior of the square lattice, which is always a minimum. The dotted horizontal line represents the unstable behavior of the hexagonal lattice $z = \rho = e^{i\pi/3}$, which is for every y_0 except $\bar{y_0}$ a monkey-saddle: the grey zone indicate the range of y_0 such that the ascent paths are those that connect ρ to the infinity and the descent paths are those that connect $z = \rho$ to the three square lattices around it, while the black zone indicate the range of y_0 such that the situation is reversed. Blue solid sloped line indicate stable behavior of the rhombic lattice z_0; it is the curve $y = y_0$, which exactly bisects the plane because y_0 is the independent variable. White circles represent the points of discontinuity in the values attainable by z_0, i.e. i and ρ, for which the model does not provide a smooth limit for z_0 as it has been explained at the beginning of section 3.1. Red dotted curve indicates the unstable behavior of the rhombic saddles that generate along the path between the two minima i and z_0. Their position change according to the value of y_0. The first vertical dotted green line indicate $y_0 = \frac{\sqrt{3}}{2}$ and the second one $y_0 = \bar{y_0} \simeq 1.326$, which are relevant values of y_0. The first one indicates the passage from z_0 being a fat rhombic lattice to z_0 being a skinny rhombic lattice. The second one indicates the position of z_0 such that saddles collide into the hexagon lattice, which turns into a sixth order degenerate critical point.

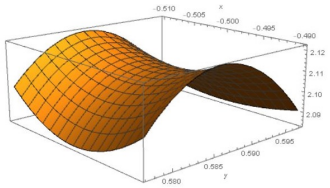

Figure 3.5: Energy surface in the neighboor of the standard saddle corresponding to $z = -\frac{1}{2} + i\bar{y}$, where $\bar{y} \simeq 0.587$. This saddle is the mountain pass to cross along the path connecting the square minimum $z = \zeta = 1/2(i+1)$ and the minimum $z_0 = -\frac{1}{2} + i(\frac{\sqrt{3}}{2} - \delta)$, where $\delta \simeq 0.1$ ($y_0 = 0.75$).

degenerate critical point and to understand precisely what it a sixth order degenerate critical point.

2. It is examined the expression of the Taylor expansion that controls the behavior of ρ when it can be classified as a sixth order degenerate critical point. In particular, we analyzed the dependence of this expression on the control parameter α_1: it turns out that there are some singular values of this parameter which would make this expression further degenerate. However a number of remarks leads to observe that these singular values are actually not to be considered valid. The conclusion of this step is that when ρ does not behave as a monkey-saddle it can be classified as a sixth order saddle surface.

3. The last step explicitely provides the combinations of values of $b_0\,, b_1\,, z_0\,, \alpha_1$ that make ρ a sixth order saddle surface both numerically and analytically. Two hypothesis are adopted: $b_0 = 1$ is fixed, hence the free parameters are three and i and z_0 have always to behave as relative minima. This latter hypothesis generates some restrictions on the remaining free parameters α_1 and b_1.

This analysis is presented in all its details to be thorough. However the most relevant information that has to be recovered is that the energy surface mostly behaves as a monkey-saddle surface in the vicinity of ρ. On the other hand, there are some combinations of the free parameters that makes it a saddle surface of order six: Figure 3.11 on page 64 will provide these combinations.

1.
For the first step we ought to reconsider the reformulation we exploited several times

$$\hat{\varphi}(x, y) := \varphi(z). \tag{3.27}$$

Notice that for convenience's sake in (3.27) we dropped the dependence on the four (which can be reduced to three) free control parameters z_0, b_0, b_1, α_1, but conceptually it obviously remains.
Then, we expand around $\varepsilon = 0$ the function $f(\varepsilon) = \hat{\varphi}(\frac{1}{2} + \varepsilon u, \frac{\sqrt{3}}{2} + \varepsilon v)$ where u, v are the displacements from the position $(1/2, \sqrt{3}/2)$ on $\mathbb{R}^2$ equivalent to $z = \rho = e^{i\pi/3}$ on the Poincaré half-plane $\mathcal{H}$.

In the result we highlight again the dependence on the four free parameters. However, the dependence on z_0 transforms into the dependence on $\gamma = J(z_0)$. Taylor expansion gives us

$$\begin{aligned} f(\varepsilon, b_0, b_1, \gamma, \alpha_1) =& \frac{b_1(-1+3\gamma) + (-1+\gamma)\,\gamma^2\,(b_0+\alpha_1)}{(-1+\gamma)^3} + \\ & \frac{a_1\, y(-3x^2+y^2)\,\gamma\,(6\,b_1 + 2b_0\,(-1+\gamma) + (-2+\gamma+\gamma^2)\,\alpha_1)}{(-1+\gamma)^3}\,\varepsilon^3 - \\ & \frac{a_2(x^4-6x^2y^2+y^4)\,\gamma\,(6\,b_1 + 2b_0(-1+\gamma) + (-2+\gamma+\gamma^2)\alpha_1)}{(-1+\gamma)^3}\,\varepsilon^4 + \\ & \frac{a_3\, y\,(5x^4-10x^2y^2+y^4)\,\gamma\,(6\,b_1 + 2b_0(-1+\gamma) + (-2+\gamma+\gamma^2)\alpha_1)}{(-1+\gamma)^3}\varepsilon^5 + \\ & (a_1^2\,(x^2+y^2)^3(\,\frac{b_0}{(-1+\gamma)^2} + \frac{a_1^2}{2}\,) + \\ & \frac{3a_1^2\,(x^6+21x^4y^2-9x^2y^4+3y^6)\,(2b_1+(-1+\gamma)\alpha_1)}{2(-1+\gamma)^3} + \\ & \frac{a_1^2\,(x^6+12x^4y^2-3x^2y^4+2y^6)(3b_1+2(-1+\gamma)\,\alpha_1)}{(-1+\gamma)^2} + \\ & a_4(-x^6+15x^4y^2-15x^2y^4+y^6)\,\frac{\gamma\,(6\,b_1+2b_0(-1+\gamma)+(-2+\gamma+\gamma^2)\alpha_1)}{(-1+\gamma)^3})\,\varepsilon^6 \end{aligned} \tag{3.28}$$

where $a_1 \simeq 26.473$, $a_2 \simeq 45.852, a_3 \simeq 52.946$, $a_4 \simeq 200.907$. The first three coefficients could already be found in the previous Taylor expansion (2.29) as expected.

This expression could appear mightily contorted but hopefully few observations will make it less confusing.

The only 0-th order term is precisely the height of (3.20) when $z = \rho$. The fact that expression (3.28) lacks both linear and second order terms proves that $z = \rho$ is a degenerate critical point with a null Hessian. Higher order terms can be analyzed with the help of an expression taken from Peckham (2011). It is a infinite sequence that provides polynomial expressions for an infinite family of high order saddle surfaces

$$f_n(x,y) = \sum_{\substack{k=0 \\ k\,even}}^{n} \binom{n}{k} x^{n-k} y^k i^k. \tag{3.29}$$

From this formula we can derive the normal expression for a second order saddle, which is a standard saddle

$$f_2(x,y) = x^2 - y^2. \tag{3.30}$$

The description of a third order saddle, which is a monkey-saddle:

$$f_3(x,y) = x^3 - 3xy^2. \tag{3.31}$$

And so forth:

$$f_4(x,y) = x^4 - 6x^2y^2 + y^4. \tag{3.32}$$

The fifth order saddle is called starfish saddle

$$f_5(x,y) = x^5 - 10x^3y^2 + +5xy^4 \tag{3.33}$$

$$f_6(x,y) = x^6 - 15x^4y^2 + 15x^2y^4 - y^6. \tag{3.34}$$

Each saddle in this family is characterized by the fact that it has precisely n directions in which the function decreases and n directions in which it increases. Moreover the graph is symmetric in such a way that all the descending and all the ascending pahts are symmetric.
We observe that the polynomial expansion in (3.28) contains each of these expressions. Third order term is the one characterizing the behavior of (3.20) in the neighbourhood of $z = \rho$, provided that its multiplying coefficient is not zero. In this case, the hexagonal point is a monkey-saddle. Though, as soon as the combination of $b_0, b_1, \gamma, \alpha_1$ is such that

$$6\,b_1 + 2\,b_0(-1+\gamma) + (-2+\gamma+\gamma^2)\,\alpha_1 = 0 \tag{3.35}$$

the third order term disappears. However, the left hand side of expression (3.35) also multiplies fourth and fifth order terms and a part of sixth order terms. Hence, if (3.35) is zero, ρ degenerates from a third order to a sixth order critical saddle. This is a consequence of the dimensions of the lattice group of the hexagonal metric. If we solve (3.35) with respect to γ, we are able to predict for every value of the relative height $\frac{b_0}{b_1}$ and of α_1 which value of γ would tranform the hexagonal points into sixth order degenerate critical points of (3.20). In other words we are able to forecast for every value of the temperature which choice of the second minimum z_0 would make the hexagon a sixth order degenerate critical point. We will now discuss in which sense, taking into account also the role of α_1 parameter.

2.
First and foremost, solving (3.35) gives us the following expressions

$$\gamma_1(b_0,b_1,\alpha_1) = \frac{-2\,b_0 - \alpha_1 - \sqrt{4\,b_0^2 + 12\,b_0\,\alpha_1 - 24\,b_1\alpha_1 + 9\,\alpha_1^2}}{2\,\alpha_1} \tag{3.36}$$

$$\gamma_2(b_0,b_1,\alpha_1) = \frac{-2\,b_0 - \alpha_1 + \sqrt{4\,b_0^2 + 12\,b_0\,\alpha_1 - 24\,b_1\alpha_1 + 9\,\alpha_1^2}}{2\,\alpha_1}. \tag{3.37}$$

Once we have substituted to γ expression (3.36) (or indifferently expression (3.36)), the expansion (3.28) loses its dependence on γ. Sixth order terms, which controls the behavior of the function in the vicinity of ρ, become

$$g(x,y,\alpha_1) = \frac{1}{3}\,a_1^2\,(x^6 + x^4\,y^2\,(6 - 9\,\alpha_1) + x^2\,y^4\,(1 + 6\,\alpha_1) + y^6(\frac{4}{3} - \alpha_1)). \tag{3.38}$$

This expression only depends on α_1 and the dependence on the relative height is lost. Though, it is not lost in the 0-th order term, which controls the altitude of the potential when $z = \rho$. Once we fixed α_1 we could be misled into infering that the appearance of the strain energy function in the vicinity of ρ, which is controlled by (3.38), is the same at every temperature. However, this would hold under the

indispensable condition that γ, i.e. z_0, was chosen at each temperature in order to satisfy relation (3.36). Hence, there exists a dependence on the temperature, which is hidden in the choice of γ.
To help us understand the dependence on α_1 of (3.38), we perform the following change of variable

$$h(\vartheta, \alpha_1) := g(\cos\vartheta, \sin\vartheta, \alpha_1). \tag{3.39}$$

The angle ϑ identifies the directions around $z = \rho$. According to the sign of $h(\vartheta, \alpha_1)$, we are able to determine which of these directions are upward and which are downward for every fixed value of α_1. Observing (3.38), it is evident that for certain values of α_1 the expression loses one of its monomials accordingly. Indeed

$$g(x, y, \frac{4}{3}) = \frac{a_1^2 x^6}{3} - 2a_1^2 x^4 y^2 + 3a_1^2 x^2 y^4 \tag{3.40}$$

$$g(x, y, \frac{2}{3}) = \frac{a_1^2 x^6}{3} + \frac{5}{3} a_1^2 x^2 y^4 + \frac{2a_1^2 y^6}{9} \tag{3.41}$$

$$g(x, y, -\frac{1}{6}) = \frac{a_1^2 x^6}{3} + \frac{5}{2} a_1^2 x^4 y^2 + \frac{a_1^2 y^6}{2}. \tag{3.42}$$

For every other fixed value of α_1, (3.38) can be traced back to (3.34). This latter expression is the normal polynomial description of a sixth order saddle. We can thus infer that the behavior of the strain energy function in the vicinity of ρ is precisely the one of a sixth order saddle surface (Fig. 3.6 on the facing page). In particular when $\alpha_1 = \frac{7}{3}$ we recover the normal form

$$g(x, y, \frac{7}{3}) = \frac{1}{3} a_1^2 \, (x^6 - 15x^4 y^2 + 15x^2 y^4 - y^6). \tag{3.43}$$

A sixth order saddle surface is such that there are six relevant directions; along three of them the surface has a maximum while along the three remaining directions it has a minimum. The plot of (3.39) for different values of α_1 best clarifies the picture (see Fig. 3.7 on page 60).
So far we have been describing the meaning of (3.38) without ever considering which implications stem from the dependence on the relative height. (3.38) is the degenerate form of Taylor expansion's sixth order terms, once γ is chosen to be (3.36) or (3.37). These expressions do not exist for every value of α_1. Setting $b_0 = 1$, their domain is defined as

$$\begin{aligned} &0 < b_1 < 1 \qquad \vee \\ &\{ \, (b_1 \leq 0 \, \vee \, b_1 \geq 1) \wedge \\ &\left[\alpha_1 \leq \frac{2}{3}(-1 + 2\, b_1) - \frac{4}{3}\sqrt{-b_1 + b_1^2} \;\vee\; \alpha_1 \geq \frac{2}{3}(-1 + 2\, b_1) - \frac{4}{3}\sqrt{-b_1 + b_1^2} \right] \} \end{aligned} \tag{3.44}$$

Hence, for every fixed value of the temperature, which produces a corresponding fixed value of b_1/b_0, α_1 needs to satisfy condition (3.44). As a consequence, not all previously mentioned "singular" values of α_1 are always valid. This is the

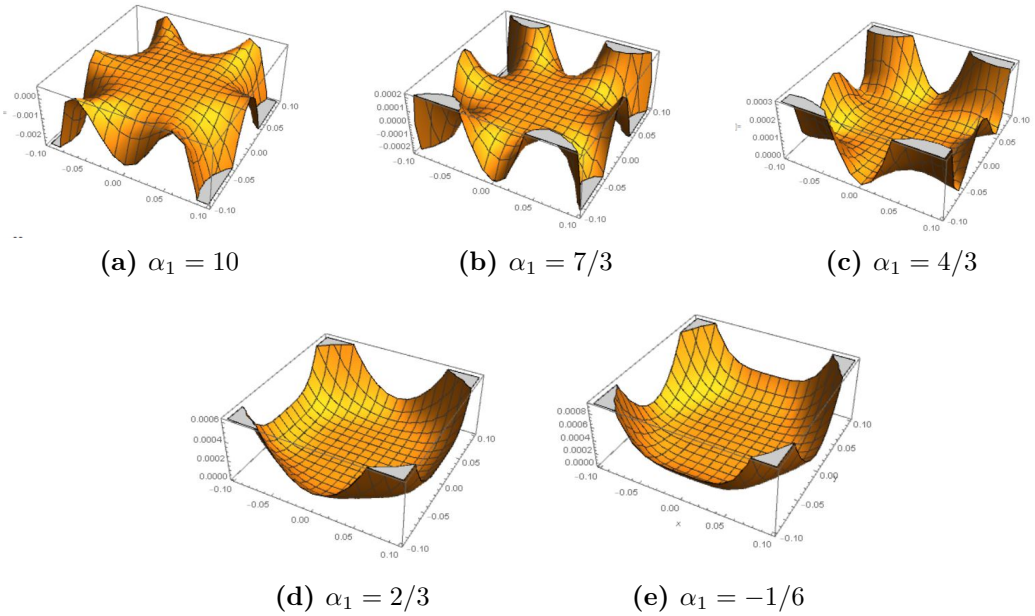

(a) $\alpha_1 = 10$ **(b)** $\alpha_1 = 7/3$ **(c)** $\alpha_1 = 4/3$

(d) $\alpha_1 = 2/3$ **(e)** $\alpha_1 = -1/6$

Figure 3.6: Energy surface in the vicinity of ρ at different values of α_1. (a) and (b) are sixth order saddle surfaces. (c) , (d) and (e) show the behavior in the degenerate cases (3.40), (3.41), (3.42).

first constraint to which α_1 is subjected. High values ($\alpha_1 \geq \frac{7}{3}$) tipically ensure compliance with condition (3.44) for any value of b_1/b_0, which implies this would be a more convenient choice.

3.

The previous paragraph unfolds from the hypothesis that γ satisfies either expression (3.36) or (3.37). Since $\gamma = J(z_0)$, these expressions precisely allow us to forecast, for every value of the temperature, which choice of the second minimum z_0 would make the energy surface in the vicinity of ρ convert from a monkey-saddle to what we found to be a sixth order saddle.

In subsection (3.2.1), it is reported a value of z_0 satisfying this property; we labelled it $\bar{z_0}$. This value was obtained numerically starting from the full strain energy function (3.20), under the hypothesis of the energetic landscape being paralyzed at a fixed value of the relative height $b_1/b_0 = 1$. We recall that this latter condition implies that α_1 does not change the character of stationary points, as it is explained at the beginning of section (3.2): we obtain the very same $\bar{z_0}$ for any value of α_1 satisfying condition (3.23). We can now recover and confirm this value also analytically by exploiting expression (3.35). We obtain

$$\gamma_1(1, 1, \alpha_1) = -2 \quad \forall \alpha_1. \tag{3.45}$$

This value is exactly the one attained by Klein Invariant J when $z = \bar{z_0} = \bar{x_0} + i\bar{y_0}$, where $\bar{x_0} = -\frac{1}{2}$ and $y_0 \simeq 1.326$:

$$J(-\frac{1}{2} + i\, 1.326) \simeq -2. \tag{3.46}$$

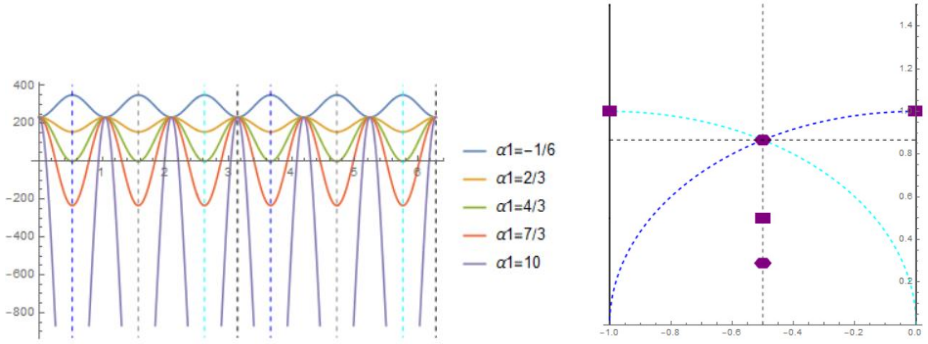

(a) $h(\vartheta, \alpha_1)$ **(b)** $\mathcal{H}$ around ρ

Figure 3.7: (a) $h(\vartheta, \alpha_1)$ for $\vartheta \in [0, 2\pi]$ at different values of α_1. It is a periodic function, whose period is $\frac{\pi}{3}$. Black dashed vertical lines indicate values of ϑ corresponding to x-direction, gray dashed vertical lines indicate values corresponding to y-direction. Blue and cyan dashed lines indicate ϑ values corresponding to the round geodetics crossing ρ. (b) represents a portion of the Poincaré half-plane $\mathcal{H}$ around $z = \rho$. We represented only the geodetics crossing ρ. Black dashed horizontal line identifies x-direction: it is not a geodetic belonging to Dedekind Tessellation, but simply a graphic device. Graphic conventions are consistent with those adopted in (a).
For every value of α_1 the function behaves identically along y-direction and along blue and cyan geodetics (let us name these directions "first group").On the other hand, it behaves identically along x-direction and along directions corresponding to $\vartheta = \frac{\pi}{3} + k\frac{\pi}{3}$, $k = 0, 1, 2, 3$ ("second group"). At $\alpha_1 = -1/6$, all directions are upward, with maximum ascents along the first group and minimum ascents along the second group. Also at $\alpha_1 = 2/3$, every directions is upward but maxima and minima interchange. At $\alpha_1 = 4/3$, the second group of directions are upward and the first group locates directions where the function is flat. At $\alpha_1 = 7/3$, along the first group of directions the function descends at its highest steepness, while along the second group of directions the function climbs up at its highest steepness. When α_1 increases, for instance $\alpha_1 = 10$, the picture is the same as for $\alpha_1 = 7/3$ but the descents are steeper.

Notice that we also confirmed the partial irrelevance of α_1 since -2 holds $\forall\alpha_1$. We named it partial because condition (3.23) must be respected, although evidently this constraint does not come to the light when considering the polynomial expansion of the potential. (3.23) is the second constraint to which α_1 is subjected.

Polynomial approximation is a robust device, which allows to easily neglect some of the hypotheses that can not be dropped when working directly with (3.20), unless some numerical efforts. We consider again two relative minima with possibily different heights, by fixing $b_0 = 1$ and releasing b_1, which becomes the main free parameter. In this regard, we need to make one important remark.
Imposing $b_0 = b_1 = 1$ implies that the conditions to ensure that $H_{\hat{\varphi}}(x_0, y_0)$ and $H_{\hat{\varphi}}(0, 1)$ are positive-definite both coincide with (3.23): together with (3.44), these are the two "only" constraints imposed on α_1. When b_1 is a free parameter, a further requirement intervenes, i.e. a third constraint. Let us analyze again the case of $z_0 = \frac{1}{2} + i(\frac{\sqrt{3}}{2} - \delta)$, where $\delta = 0.1$. An easy computation shows that in order to guarantee that the eigenvalues of (3.25) and (3.26) are all strictly positive α_1 must respect a third constraint

$$\alpha_1 > \frac{3}{2} f\, b_1 \tag{3.47}$$

where $f = \frac{2}{|J(z_0)-1|}$. Expression (3.47) is not the proper condition for every choice of z_0. It has to be numerically retrieved every time; though, we can generally claim that it will turn to be more restrictive than (3.23).

With this awareness, we can finally address the research of the values of z_0 that make the energy in the neighboor of ρ a sixth order saddle surface for each value of b_1 (recall that $b_0 = 1$ has been fixed).
Since z_0 represents either a fat or a skinny rhombic lattice, it can lie on two of the three edges of the fundamental domain $\mathcal{D}$. Those edges both can be found on the straight line $x = \frac{1}{2}$, as well as on all its suitable copies because of $GL(2, \mathbb{Z})$-invariance. By fixing $x_0 = \frac{1}{2}$ and varying $y_0 \in (\frac{1}{2}, \infty) \setminus \{\frac{\sqrt{3}}{2}\}$, we explore all the possibilities for z_0.
When considering the polynomial expansion, the research of the values of z_0 fulfilling the mentioned requirement is just a matter of plotting (3.35). Though, the result has been obtained also numerically (see Fig. 3.8 on the following page). In other words, adopting the labelling convention of subsection (3.2.1), we are seeking for the relation $J(\bar{z_0})(b_1)$. A priori, we can not know in which range it is suitable to vary b_1. Let us consider for instance $b_1 \in [-4, 4]$. The numerical result shows that $J(\bar{z_0})$ is approximately confined in $J(\bar{z_0}) \leq -1$, hence it is always negative. As a consequence, $\bar{z_0}$ represents for every value of b_1 in this range a skinny rhombic lattice (see Fig. 3.9 on the next page).
We need to ensure that $\bar{z_0}$ obtained for every value of b_1 is truly a minimum, as well as $z = i$. As we already mentioned, this results in choosing α_1 so that it respects the three depicted constraints. A rather high value of α_1 safely guarantees that the requirements are obeyed. Thus, Fig. 3.8 on the following page is obtained under the hypothesis $\alpha_1 = 10$. Consequently, also the choice of the range $b_1 \in [-4, 4]$ gains a proper significance; for this value of α_1, (3.44) implies that $b_1 \leq \frac{64}{15} \simeq 4.27$. Notice

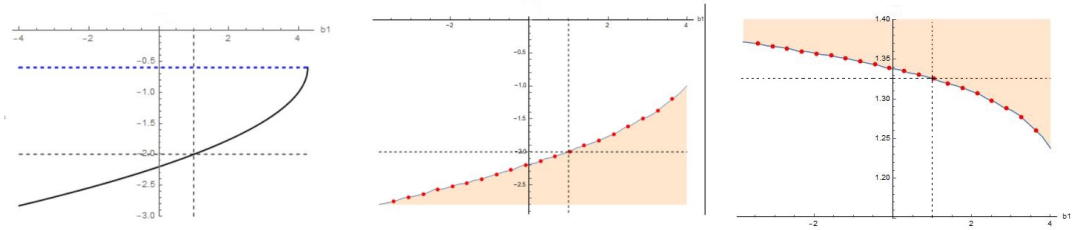

(a) $J(\bar{z_0})(b_1)$ **(b)** $J(\bar{z_0})(b_1)$ **(c)** $\bar{y_0}(b_1)$

Figure 3.8: Behavior of $J(\bar{z_0})(b_1)$ when $\alpha_1 = 10$. (a) Result obtained analytically by plotting (3.36). Blue dashed line locates the symmetry axis of the function. Black dashed lines locate $J(\bar{z_0})$ in the case $b_0 = b_1 = 1$: this is -2, as (3.45) shows. (*b*) The same result obtained numerically. (*c*) By inverting the function in (*b*), we can obtain the behavior of $\bar{y_0}$; this fully locates $\bar{z_0}$ because $\bar{x_0} = 1/2$ is fixed.

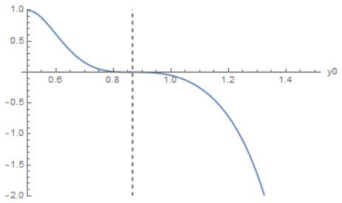

Figure 3.9: $J(z_0)$ where $z_0 = x_0 + iy_0$. We fix the x-coordinate, $x_0 = 1/2$, and we vary the y-coordinate, $y_0 \in (\frac{1}{2}, \infty) \setminus \{\frac{\sqrt{3}}{2}\}$. When z_0 represents a fat rhombic lattice the Klein Invariant J attains values between 1 and 0, where 1 and 0 are to be excluded because they are the values it attains at the vertices of $\mathcal{D}$ $z = i$ ans $z = \rho$; as explained in section (3.1) they are not valid values for z_0. When z_0 represents a skinny rhombic lattice, it attains increasingly negative values. Notice that all values are real because we restricted at the boundary $\partial\mathcal{D}$ of the fundamental domain.

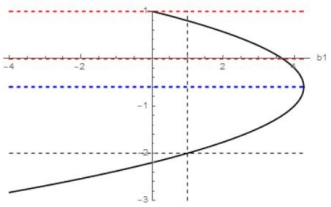

Figure 3.10: (3.36) and (3.37) when $b_0 = 1$ and $\alpha_1 = 10$. The independent parameter is b_1, which varies according to condition (3.44): $b_1 \leq \frac{64}{15}$. Blue dashed line indicates the symmetry axis, which splits the two branches γ_1 and γ_2. Red dashed line indicates $\gamma_2 = J(\bar{z_0}) = 0$, which would imply $\bar{z_0} = \rho$ and $\gamma_2 = J(\bar{z_0}) = 1$, which would imply $\bar{z_0} = 1$; these are not acceptable values for z_0. The upper branch locates values of $J(\bar{z_0})$ that correspond to either skinny rhombic lattices gathered in the neighboor of ρ or fat rhombic lattices. $\alpha_1 = 10$ is not high enough to guarantee that each z_0 belonging to this branch conveniently combined with the corresponding value of b_1 on the horizontal axis is a minimum for the strain energy function together with $z = i$. Thus, the values of $\bar{z_0}$ located by the second branch γ_2 are not to be considered.

that all the considered relationships are recursive and the dependences among the parameters are tangled: the adopted way of proceeding is one in a collection of possible procedures.

One could object that we never considered expression (3.37). It describes the twin branch of (3.36), as we can recognize from the plot of both (3.36) and (3.37) (see 3.10). This branch locates $\bar{z_0}$ gradually closer to $z = i$ for each value of b_1. The combinations of $\bar{z_0}$ and b_1 pinpointed by this branch would require increasing values of α_1 to fullfill the three constraints, untill α_1 diverges; if we set $\alpha_1 = 10$, this branch locates non acceptable solutions. This naturally leads to the last observation.
We want to investigate what happens to the branches describing the evolution of $J(\bar{z_0})(b_1)$ when increasing α_1, in order to make acceptable a a wider range of solutions. Observing 3.11 on the following page, it is revealed that high values of α_1, which are necessary if we want to ensure the condition of minimum of those $\bar{z_0}$ close to i, flatten the branches precisely at the constant values $J(\bar{z_0}) = -2$ and $J(\bar{z_0}) = 1$; this latter would correspond to $\bar{z_0} = i$, which is not acceptable. We can thus infer that (exept for some meticolous combination of α_1, b_1) the second branch of solution γ_2 is not to be considered: $\bar{z_0}$ is unique and it corresponds to a skinny lattice, more or less deformed according to the value of b_1.

3.3 Energy barriers

This new section is devoted to the analysis of some relevant transformations by means of the model we have been describing in this chapter. Our strategy retraces the one adopted in section (2.4) of the previous chapter, which was commited to the same topic. Thus, we skittishly take the liberty to neglect the proper introduction;

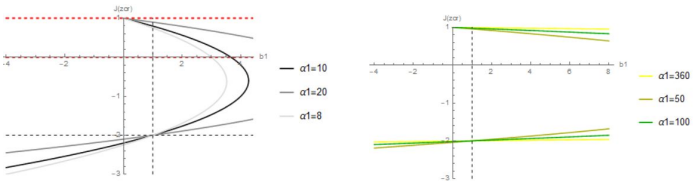

(a) $J(\bar{z_0})(b_1)$ at different values of α_1

(b) $J(\bar{z_0})(b_1)$ at different high values of α_1

Figure 3.11: (a) γ_1 and γ_2 at different values of $\alpha_1 = 8, 10, 20$. Red dashed lines indicate non acceptable values of $J(\bar{z_0})$. Black dashed lines cross at $(b_1, J(\bar{z_0})) = (1, -2)$. The variation of α_1 does not move this point, as (3.45) shows. (b) Same as (a), but α_1 varies at higher values. Black dashed line indicates $b_1 = 1$. The two branches flatten at $J(\bar{z_0}) = 1$ and $J(\bar{z_0}) = -2$.

this would be a precise copy of that given at the beginning of the mentioned section. We suppose again that the temperature is fixed, which implies that the relative height b_1/b_0 is fixed. Since it has emerged from the previous sections that $b_1/b_0 = 1$ returns a meaningful energetic outlook, we assume again this hypothesis.
Among the equivalent copies of the fundamental domain $\mathcal{D}$ which constitute the Dedekind Tessellation of the Poincaré half-plane $\mathcal{H}$ (hence of the strain space), we can identify the "first neighbors", i.e. those domains sharing a part of the boundary. These domains can be related through the following transformations (or by suitably combining these):

$$z \mapsto z + 1 \tag{3.48}$$

$$z \mapsto -\frac{1}{z}. \tag{3.49}$$

These transformations correspond respectively to a simple shear and a $\frac{\pi}{2}$-rotation (see section 1.2.1). More importantly, they descend from the matrices that span $SL(2, \mathbb{Z})$. As section (2.4) explained, jumping between equilibrium configurations belonging to two domains sharing a portion of the boundary, hence related through (3.48) or (3.49), let us explore the plastic domain. In particular the computation of the energy barriers existing between such adjacent equlibrium configurations allows to quantify the end of the elastic response of a material whose strain energy function is precisely (3.20).
Since $b_1/b_0 = 1$, the equilibrium configurations correspond to either the square lattices or the rhombic lattices, which are always minima under this hypothesis. Thus, we can apply tranformations (3.48) and (3.49) both to i and z_0. In particular we will investigate the energy barrier associated to a simple shear from the square equilibrium configuration

$$i \mapsto i + 1 \tag{3.50}$$

and a $\pi/2$-prerotation followed by a simple shear from the rhombic equilibrium configuration

$$z_0 \mapsto -\frac{1}{z_0} + 1. \tag{3.51}$$

3.3.1 The physical intepretation of α_1

Having chosen $b_1/b_0 = 1$, we deal with two free parameters z_0, α_1, which must be combined as follows. For every z_0 appointed with the role of minimum, the only condition that α_1 needs to obey is (3.23); once it is respected, z_0 and i are the two minima of the strain energy function. As this condition just provides a lower bound, α_1 partially remains free. Our purpose is to understand whether it is related to the energy barriers, so that it can be conferred with some physical interpretation.
Stemming from (2.35), the energy barriers are computed by selecting the optimal path to walk along between two chosen adjacent equilibrium configurations. We are now dealing with two free parameters. Hence the definition changes accordingly

$$\Delta E_{best}(z_0, \alpha_1) = \min_{\forall paths} \max_{z \in path} \varphi(z, z_0, \alpha_1) - \min_{z \in path} \varphi(z, z_0, \alpha_1) \tag{3.52}$$

where $\varphi(z, z_0, \alpha_1)$ is (3.20) once fixed $b_1/b_0 = 1$.
This definition can be better understood in light of an example. Suppose that we want to investigate the energetically optimal barrier-crossing path from i to $i+1$. For every choice of the second minimum z_0, the picture changes (see 3.4 on page 54). For every fixed value of z_0, among the paths connecting i to $i+1$ we choose the one that guarantees to pass across the lowest among the summits. The walk ends as soon as we encounter the minimum of (3.20) along the selected path. We can compute the energy barriers through the difference between the maximum and the minimum along the chosen path. The parameter α_1 does not change neither positions nor character of stationary points, hence it does not intervenes on the choice of the path. As we are about to see, α_1 either amplifies or contracts the height of the barriers. Most interestingly, this happens with a simple linear dependence.

Since the choice of z_0 affects the landscape significantly, we represent in Fig. 3.12 on the following page the energetically optimal barrier-crossing paths of tranformation (3.50) and (3.51) accordingly considered in order to hopefully make the following representation of energy barriers clearer. When $b_1/b_0 = 1$, we already remarked that we can distinguish four significant choices of z_0. We established that all possible positions can be found along the straight line $x = 1/2$, hence x_0 is fixed and there are four relevant ranges where to set y_0. These are conveniently indicated in Fig. 3.12 on the next page. In this figure, we indicated transformations $i \mapsto i+1$ and $z_0 \mapsto -1/z_0 + 1$. We can identify the most favorable paths of each of the two tranformations; these imply crossing mountain passes and meeting crossroads. Mountain passes correspond to the standard saddles, whose position is reported in Fig. 3.4 on page 54. On the other hand, the main crossroads are at the hexagonal points; these are mountain passes that sit along the symmetry-related minimum-to-minimum energetically optimal paths.
The four ranges can be recovered in the energy barriers representation of Fig. 3.13. Since $b_1/b_0 = 1$, i.e. the height of the energy is the same at the two minima i and z_0, when computing (3.52) it holds that for any choice of α_1 and z_0

$$\min_{z \in path} \varphi(z, z_0, \alpha_1) = b_0 = b_1 \quad . \tag{3.53}$$

On the other hand the mountain pass to cross changes depending on the transformation considered and depending on the position of z_0 as Fig.3.12 shows. However,

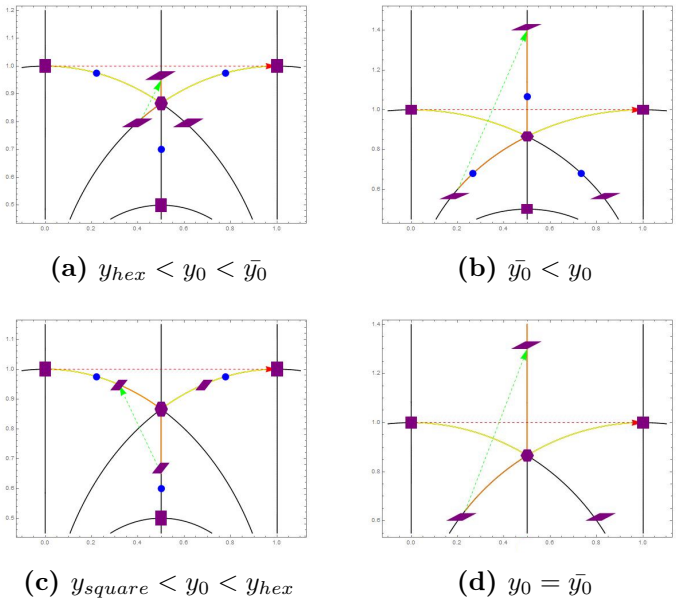

(a) $y_{hex} < y_0 < \bar{y_0}$ **(b)** $\bar{y_0} < y_0$

(c) $y_{square} < y_0 < y_{hex}$ **(d)** $y_0 = \bar{y_0}$

Figure 3.12: Transformations and paths at different values of z_0. The red line indicates in each picture the shear $i \mapsto i + 1$ and the green line indicates the tranformation obtained by the composition of a $\pi/2$-prerotation and a simple shear of the rhombic lattice $z_0 \mapsto -1/z_0 + 1$. The yellow curve draws the profile of the energetic passageway of the shear, while the orange curve draws the one of the composed tranformation. The blue points represent the saddles that generate along the geodesics: these are the summits to cross in every paths. In (a) and (b), z_0 corresponds to a skinny rhombic lattice; (b) considers the case of a very distorted lattice, such that the summits jump and change their nature from fat rhombic lattices to skinny rhombic lattices. $\bar{y_0}$ is the limit value; in (d) when $y_0 = \bar{y_0}$, summits collide into the hexagonal lattice, which turns into a sixth order saddle surface as discussed in the previous sections. While in this case the energy descends along all geodetics leaving from ρ, in all other three cases the hexagonal point is a monkey-saddle, i.e. the bifurcating mountain pass to cross when walking between two adjacent and equivalent equilibrium configurations. In (c), z_0 corresponds to a fat rhombic lattice.

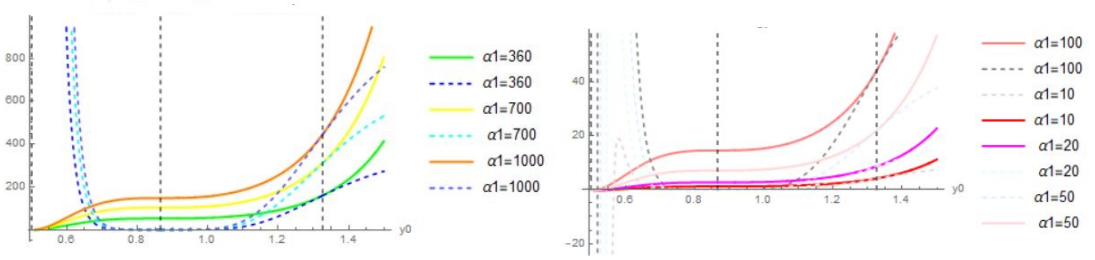

(a) $360 \leq \alpha_1 \leq 1000$ **(b)** $10 \leq \alpha_1 \leq 100$

Figure 3.13: Energy barriers for every choice of z_0 at different values of α_1. $z_0 = 1/2 + i\, y_0$, hence y_0 is the horizontal coordinate. Dashed black vertical lines indicate special values of y_0: $1/2$ and $\sqrt{3}/2$, which are not valid because they respectively correspond to the square and hexagonal lattice, and $\bar{y_0}$, which turns the hexagon in a sixth order degenerate critical point. In both figures, solid lines indicate the behavior of the energy barrier with respect to increasing values of α_1 and y_0 when the mountain pass to cross is at the standard saddle; instead dashed lines represent the result obtained when the mountain pass is at the hexagonal points. When $y_0 = \bar{y_0}$ the standard saddles collide into the hexagonal points, which makes dashed and solid lines meet. Figure (a) considers high values of α_1. High values of this parameter guarantee that condition (3.23) is respected even when z_0 is close to i; at this point the lower bound of condition (3.23) diverges to $+\infty$. Figure (b) considers lower values of α_1, which guarantee that (3.23) is respected only when z_0 is conveniently far from i. In both figures dashed lines diverge when z_0 moves close to i because the height of the energy at the hexagonal points depends on $\frac{1}{|J(z_0)-1|^3}$ as (3.28) tells, hence transformations implying a passage across the hexagonal points are impossible. In Fig.(b) we observe that when z_0 moves closer to i curves tend to $-\infty$ because the values of α_1 considered do not ensure a correct behavior of the strain energy function.

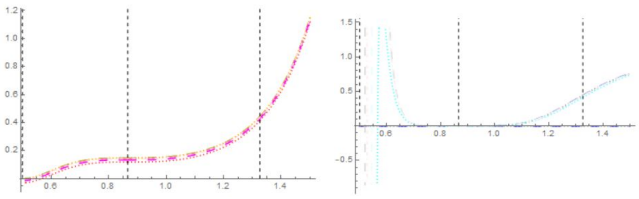

(a) mountain pass at z_{saddle} **(b)** mountain pass at $z = \rho$

Figure 3.14: $\frac{\Delta E_{best}(z_0,\alpha_1)}{\alpha_1}$: (a) reports the result when we use (3.54) to compute the energy barriers, while (b) reports the result obtained when using (3.55). The values of α_1 are those considered in Fig. 3.13 on the previous page. Solid curves in Fig. 3.13 on the preceding page collide into one unique curve when computing their ratio with respect to α_1, as well as dashed curves. This implies that the energy barriers have a linear increasing dependence with respect to α_1, which ultimately gains a precise physical meaning.

we observed that it can correspond either to the hexagonal points or to the rhombic saddles. Hence, if we consider the portion of the Poincaré half-plane $\mathcal{H}$ around the hexagonal point $z = \rho$

$$\min_{\forall paths} \max_{z \in path} \varphi(z, z_0, \alpha_1) = \varphi(\rho, z_0, \alpha_1) \tag{3.54}$$

or

$$\min_{\forall paths} \max_{z \in path} \varphi(z, z_0, \alpha_1) = \varphi(z_{saddle}, z_0, \alpha_1). \tag{3.55}$$

Therefore, Fig. 3.13 on the previous page reports what we obtained from the computation of (3.52) considering each of the two possibilities (3.54), (3.55). It emerges what we had previously announced: when increasing α_1, the value of the energy barrier increases. Furthermore, we can claim that $\Delta E_{best}(z_0, \alpha_1)$ is a linear relation with respect to α_1. The mathematical translation of this concept is

$$\frac{\Delta E_{best}(z_0, \alpha_1)}{\alpha_1} = \Delta E_{best}(z_0). \tag{3.56}$$

This equality is confirmed by Fig. 3.14.
In conclusion, α_1 can be defined as the parameter controlling the height of the energy barriers of the plastic deformations, at least when we fix the temperature at a value such that the energetic basins $z = z_0$ and $z = i$ are equally convenient.

3.4 Single state stability

Martensitic phase transformations are associated with abrubt modifications in the lattice structure at some some specific values of the external control parameters, such as the temperature or the mechanical loading. At high temperature the austenite phase is the stable state while at low temperature the stable state is martensite. A state stability impinges on the strain energy function by imposing a positive-definite behavior around the point corresponding to the considered state.

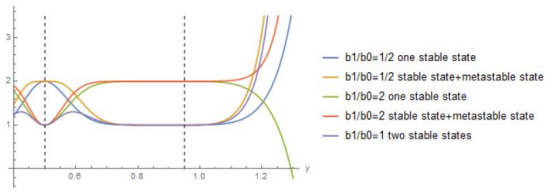

Figure 3.15: Behavior of the strain energy function (3.20) along the straight line $x = 1/2$ between $z_0 = 1/2 + i(\sqrt{3}/2 + \delta)$ and the square lattice $\zeta = 1/2 + i1/2$ at different values of the temperature. For each value of the relative height by properly choosing α_1 we represent the case of one stable state cohexisting with a metastable state and the case of one unique stable state. Only in the case $b_1/b_0 = 1$ the square and rhombic points, indicated by vertical dashed lines, are cohexisting minima and have equal energy density.

Hereinbefore, we have always properly combined the free parameters of (3.20) in order to ensure that both i and z_0 behaved as minima for the function. The hypothesis $b_1/b_0 = 1$ enshrines their equal convenience as relative minima for the potential. Section (3.2.2) also investigates different values of the relative height; in this case i and z_0 were minima, but one was the least energy state while the other played the role of a metastable state.
We now want to examine the energetic landscape that generates when one single phase between austenite and martensite is stable, exploring high and low temperatures.
There being three free parameters $b_1/b_0, z_0$ and α_1, we have already appreciated that the analysis is rather involved. Hence, we will fix z_0 to a representative value because for any other choice of z_0 the procedure is analogous. We choose $z_0 = \frac{1}{2} + i(\frac{\sqrt{3}}{2} + \delta)$, where $\delta \simeq 0.1$: it represents a skinny rhombic lattice sufficiently but not excessively distorted with respect to the hexagonal lattice.
We consider two values of the relative height in order to inspect both high and low ranges of temperature. We expect that at high temperatures there exists a unique stable state for the strain energy function in the square lattice i ; at low temperatures i loses the privilege and exchanges the character of stable state with the less symmetrical stationary point z_0. Two specific values that turn out to represent these two situations are

$$\frac{b_1}{b_0} = \begin{cases} 1/2 & \text{low temperature} \\ 2 & \text{high temperature} \end{cases} . \tag{3.57}$$

Again, setting the relative height at one of these two values is not a sufficient condition to completely fix the strain potential in order to properly represent the demanded physical picture: α_1 has to be conveniently chosen so that for each value of (3.57) there exists one unique stable state. Indeed, we do not want to explore the case of a stable state combined with another metastable state, which would express in terms of (3.20) with the cohexistence of an absolute minimum and a relative minimum (see Fig. 3.15); this case was already investigated in section (3.2.2).

3.4.1 High temperature landscape

We will first analyze the case $b_1/b_0 = 2$, which sets the model in the domain of high temperature. We want to inspect the profile of the strain energy function in the case of a unique minimum corresponding to the square lattice.
Again, the resulting analysis risks to be mightily contorted because of the number of conditions considered, hence we first present the list of the steps that have been followed in this subsection :

1. We discuss the constraints that α_1 should obey in order to guarantee that the chosen z_0 truly is an unstable critical point for the function (3.20) while $z = i$ is a minimum.

2. We analyze the character of z_0 under these hypotheses and we observe how the energetic landscape in turn changes by generating a new stationary point.

3. We release z_0 from its fixed value (in the previous steps z_0 is fixed to $z_0 = \frac{1}{2} + i(\frac{\sqrt{3}}{2} + \delta)$) and we provide a general representation of the variations of the energetic landscape (i.e. of its stationary points) at high temperature ($b_1/b_0 = 2$) depending on z_0. The value of the free parameter α_1 is chosen stemming from the considerations obtained in the previous steps. This choice has some consequences on the generality of this representation, which are also explored.

1.
In order to represent the required picture α_1 is subjected to some conditions. On the one hand, we usually impose a lower bound deriving from (3.23); this condition is essential to ensure the physical consistence and validity of our model. On the other hand, (3.20) should not have a positive-definite behavior in the vicinity of z_0 because we want to explore instability. Hence, α_1 has to be chosen in the following range

$$\frac{2\,b_1}{|J(z_0) - 1|} < \alpha_1 < \bar{\alpha_1} \tag{3.58}$$

where $\bar{\alpha_1} \simeq 4.933$ was obtained numerically computing the Hessian matrix of (3.20) in $z = z_0 = \frac{1}{2} + i(\frac{\sqrt{3}}{2} + \delta)$. The lower bound is $\frac{2\,b_1}{|J(z_0)-1|} \simeq 3.946$.
For any value of α_1 in this range, the energy surface is a standard saddle in the neighbourhood of z_0 (see 3.19 on page 73), while i always behaves as a minimum.
A short remark concerns the hexagonal points. As we discussed in section (3.2.2), they are monkey-saddles except for precise combinations of the free parameters of (3.20), none of which coincide with the one currently adopted.
The character degeneration of z_0 into a standard saddle warps the energy profile. If we chose $\alpha_1 \geq \bar{\alpha_1}$, the basins of (3.20) would still be at the square and rhombic points; as soon as α_1 falls into the range (3.58) the landscape depressions in z_0 and its equivalent copies turn into saddle mountain passes.

2.
Fig. 3.16 on the next page and Fig. 3.15 on the preceding page suggest that z_0 remains a relative minimum along the direction orthogonal to the geodesic where

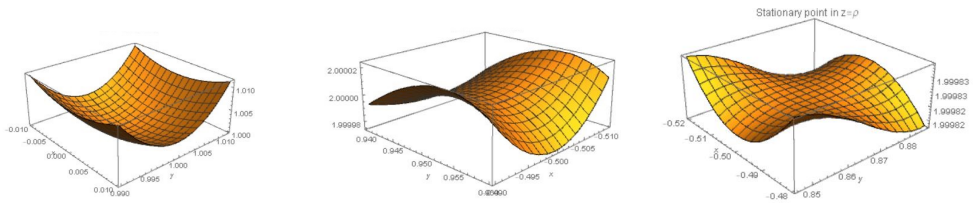

(a) $z = i$ **(b)** $z = z_0$ **(c)** $z = \rho$

Figure 3.16: Behavior of the energy surface in the vicinity of i, z_0 and ρ at high temperature. The square lattice is the unique minimum of the function. The rhombic lattice is a standard saddle while the hexagonal lattice is a monkey-saddle.

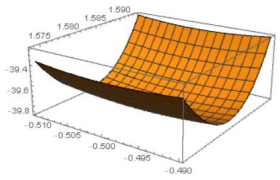

Figure 3.17: Behavior of the energy surface in the vicinity of z_{min}

it lies and it tranforms into a relative maximum in the direction located by the geodesic itself. The geodesic is the path connecting z_0 on one side to the hexagonal point and on the other side to infinity (see Fig. 3.3 on page 53(b) to visualize these paths). There being a relative maximum at z_0 along the geodesic, the tendency of the energy is decreasing in the neighbourhood of this point. Though, this tendency invert towards infinity because the energy has been constructed to eventually diverge to $+\infty$. The tendency reversal point correspond to a new basin, i.e. a new minimum for (3.20). When $z_0 = \frac{1}{2} + i(\frac{\sqrt{3}}{2} + \delta)$, where $\delta \simeq 0.1$, the minimum is at $z_{min} = \frac{1}{2} + iy_{min}$, where $y_{min} \simeq 1.583$, hence it represents a very distorted skinny rhombic lattice (see Fig. 3.17).

3.

Starting from this, we proceeded with an analysis that retraces section (3.2.1). The aim was to obtain a similar figure to Fig. 3.4 on page 54, in order to give a meaningful representation of position and character of stationary points at high temperature. Indeed, the position of z_{min} changes with the position of z_0. However, the basin corresponding to z_{min} only creates when z_0 degenerates into a standard saddle, which corresponds to a confined choice of the value of α_1 parameter. For each z_0, α_1 has to be confined in a upper and lower bounded range in order to ensure that z_0 would be unstable, as (3.58) yields for instance in a specific case. However, Fig. 3.4 on page 54 was obtained by fixing α_1. Hence, the new figure was also obtained by fixing α_1: we chose $\alpha_1 = 3.95$. The result is represented in Fig. 3.18 on page 73. This value of α_1 is slightly higher than the lowerbound in (3.58), which controls the divergence of the energy at infinity. Since the lowerbound decreases when z_0 moves further from the hexagonal point towards infinity, such a

value of α_1 guarantees a correct behavior of the energy at infinity for any choice of z_0 representing a more distorted skinny rhombic lattice than the one corresponding to $z_0 = \frac{1}{2} + i(\frac{\sqrt{3}}{2} + \delta)$ ($\delta \simeq 0.1$). On the other hand, as z_0 increases, $\alpha_1 = 3.95$ will not be sufficiently small to mantain the unstable character of z_0, which will turn into a minimum. This limit value is $\hat{z_0} = \frac{1}{2} + i\hat{y}$, where $\hat{y} \simeq 1.11$. When $y_0 \geq \hat{y}$, precisely as section (3.2.1) shows for the case $b_1/b_0 = 1$, the character of saddle mountain pass is tranferred to a rhombic point between z_0 and the square lattice. This rhombic point corresponds to a skinny rhombic lattice; however for a small range of z_0, which is represented by the adjacent vertical dashed green lines on Fig. 3.18 on the facing page, the saddle mountain pass travels across the hexagonal point and turns into a fat rhombic lattice. This phenomen can be explained in light of section (3.2.2): when plotting expression (3.36) and (3.37) at $\alpha_1 = 3.95$ (see Fig. 3.18 on the next page(b)), it emerges that for $b_1/b_0 = 2$ there are two possible values of $\bar{y_0}$ that turn the hexagonal points into sixth order saddle surface. It is then explained the tendency inversion of the red dashed curve when $y_0 > \hat{y}$.
The analysis with all remarks and figures sprang from the initial choice on z_0 as the introduction of this chapter reported. A different but nonetheless analogous picture would have been sourced from an other choice.

3.4.2 Low temperature landscape

Imposing $b_1/b_0 = 1/2$ sets the model in the domain of low temperature, where we witness the loss of stability of i while z_0 earns the character of the unique minimum. In a complementary manner with respect to the previous situation, α_1 has to be chosen in the following range in order to

$$\frac{2\,b_1}{|J(z_0) - 1|} < \alpha_1 \leq \bar{\alpha_1} \tag{3.59}$$

where $\bar{\alpha_1} \simeq 3.946$ was obtained numerically computing the Hessian matrix of (3.20) in $z = i$. For this choice of $z_0 = \frac{1}{2} + i(\frac{\sqrt{3}}{2} + \delta)$, the lower bound is $\frac{2\,b_1}{|J(z_0)-1|} \simeq 1.973$. Under these hypotheses the energy strain fuction is a standard saddle surface in the neighboor of $z = i$, which is thus unstable (see 3.19 on the facing page) while z_0 is a minimum. The previous remark about hexagonal points still holds, thus they are monkey-saddles.
With respect to the high temperature landscape the outline is reduced to essentials; besides the a priori imposed stationary points (z_0 and its suitable copies, as well as the square points) or those intrinsically part of the landscape because of symmetry reasons (the hexagonal points) there do not exist additional stationary points. Positions and characters of predictable stationary points fully indulge the tendency of the function.

3.5 Valley-ridge inflection points and valley floors

In this section we propose a further analysis of the energy surface (3.20) which arises from a parallelism with the potential energy surface analysis exploited in theoretical chemistry to predict chemical reactions dynamics. This section draws

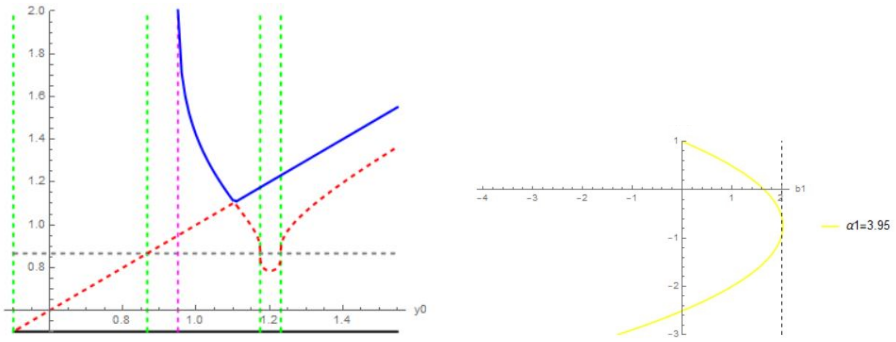

(a) **(b)** $\gamma_1(b_0, b_1, 3, 95)$ and $\gamma_2(b_0, b_1, 3, 95)$

Figure 3.18: (a) Position and character of stationary points at high temperatures, when $\alpha_1 = 3.95$. All relevant features of the energy can be represented by points lying on the straight line $x = \frac{1}{2}$. Thus, each curve of the graphic represent the variation of the y-coordinate of stationary points with a constant $x = \frac{1}{2}$. The horizontal axis corresponds to the variation of y_0. Dashed pink vertical line indicates $y_0 = i(\frac{\sqrt{3}}{2} + \delta)$ ($\delta \simeq 0.1$): smaller values of y_0 are not valid, because $\alpha_1 = 3.95$ would not guarantee the correct divergence at $+\infty$. Hence the left hand side of the picture with respect to the dashed pink line can be neglected. Black solid horizontal line indicates the stable behavior of the square point represented by $z = \zeta = 1/2 + i1/2$. Grey horizontal dashed line indicates the unstable behavior of the hexagonal point represented by $z = \zeta = 1/2 + i\sqrt{3}/2$. The blue solid curve indicates the position of stable stationary points, while red dashed curves and lines indicate the position of unstable stationary points. (b) When $b_1/b_0 = 2$, i.e. $b_1 = 2$ when fixing $b_0 = 1$, there are two intersections with the yellow curve: they correspond to those values of $J(\bar{z}_0)$, i.e. two values of $\bar{y}_0$, that transform the hexagonal points into sixth order saddle surface. These two values of $\bar{y}_0$ are reported in (a) from the last green dashed vertical lines: here the red curve intersects the grey dashed horizontal line because rhombic saddles collide into the hexagon, which turns into a sixth order degenerate critical point exactly as it happened when $b_1/b_0 = 1$ (in that case we obtained only one value of $\bar{y}_0$, see subsection (3.2.1)).

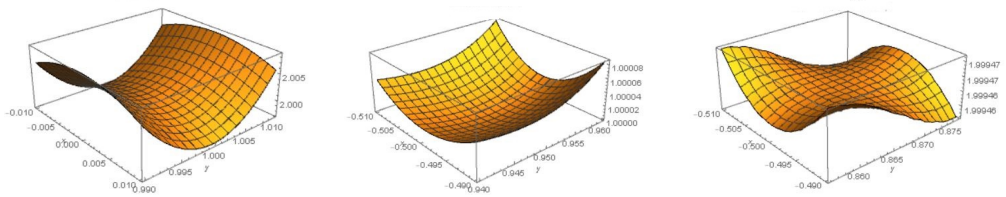

(a) $z = i$ **(b)** $z = z_0$ **(c)** $z = \rho$

Figure 3.19: Behavior of the energy surface (3.20) in the vicinity of i, z_0 and ρ at low temperature. The rhombic lattice $z_0 = 1/2 + i(\sqrt{3}/2 + \delta)$ is the unique minimum of the function. The square lattice is a standard saddle while the hexagonal lattice is a monkey-saddle.

from the work done by Hoffman, Nord, Ruedenberg (1986) and Quapp, Hirsch, Heidrich (2003).
The reason of this parallelism can be found in the definition of the minimum energy path or reaction path on a potential energy surface: this is the optimal path connecting two minimizers by passing a transition saddle point. The valley floor in between the reactant and the product phase over the saddle point is the reaction channel. A chemical reaction is the composition of a number of transitions that the system accomplishes following such elementary paths.
The energy surface (3.20) precisely reproduces this picture (once its free parameters are properly combined) if we interpret it as a potential energy surface where the reactant phase correspond to the square lattice i and the product phase correspond to the rhombic lattice z_0. The behavior of (3.20) has been deeply analyzed in its most significant facets in the case $b_1/b_0 = 1$. We thus assume again this hypothesis which truly guarantees that i and z_0 are minima of (3.20) once α_1 has been fixed according to the z_0-dependent condition (3.23).
The aim of this section is to search for the optimal "reaction path" that leads from the square minimizer to the rhombic minimizer following the definition given by Hoffman, Nord, Ruedenberg (1986) who propose to seek valley floor lines among what they call *gradient extremals*.
Before proceeding we ought to remark that not every choice of the second minimizer is suitable to reproduce an energetic landscape that complies with the expressed purpose. If we observe Fig 3.3 on page 53 we immediately appreciate that whenever z_0 corresponds to a fat rhombic lattice (picture (a)) the reaction paths trivially coincide with the portions of the geodesics connecting each equivalent pair square lattice - rhombic lattice (we will formally demonstrate that these paths actually fullfill the definition of gradient extremals). Hence z_0 has to be chosen among the skinny rhombic points. In particular, we choose again a slightly distorted skinny rhombic lattice to be the second minimizer: $z_0 = \frac{1}{2} + i(\frac{\sqrt{3}}{2} + \delta)$, where $\delta \simeq 0.1$. Subsection (3.2.1) precisely tells us that between the two minimizers we find a saddle point (SP) at $z = 1/2 + i\, y_{SP}$, where $y_{SP} \simeq 0.59$ (see also Fig. 3.5 on page 55). Notice that z_0 has been fixed for simplicity: for any other choice of z_0 (among the skinny rhombic points) the analysis is analogous to the one we are about to trace.

3.5.1 Gradient extremals

First and foremost we report the intuition of Hoffman *et al.* (1986) who define a floor line as the path that allows a person walking in a valley and moving in a direction perpendicular to the contour lines to perceive a minimal change in height. Thus this curve consists of the points of intersection with every contour line where the norm of the gradient is the smallest compared to its value in any other point of the contour. Along this curve the valley is "least steep". In other words, we seek those points in the contour subspace where the norm of the gradient

$$\frac{1}{2}|\nabla f|^2 \tag{3.60}$$

is extremal, where $V = f(x, y) : \mathbb{R}^2 \to \mathbb{R}$ is the two-dimensional surface at least of class C^3 explored by the excursionist. At any such point the following condition has to be satisfied:

$$(\mathbf{e} \cdot \nabla)(\nabla f)^2/2 = \mathbf{e} \cdot (\nabla\nabla) \cdot (\nabla f) = 0 \tag{3.61}$$

where $\mathbf{e}$ is the unit vector tangent to the contour line and perpendicular to the gradient. Expression (3.61) implies that the projection of $\nabla(\nabla f)^2/2$ onto the direction identified by this vector must vanish. The unit vector $\mathbf{e}$ is explicitely:

$$\mathbf{e} = (f_y, -f_x)/(f_x^2 + f_y^2)^{1/2} \tag{3.62}$$

By inserting (3.62) and $\nabla f = (f_x, f_y)$ into (3.61) we obtain the differential equation for the gradient extremals:

$$f_{xy}(f_x^2 - f_y^2) + (f_{yy} - f_{xx})f_x f_y = 0. \tag{3.63}$$

Hoffman *et al.* (1986) prove in the appendix that this equation corresponds to finding those points where

$$H(\mathbf{x})\nabla f(\mathbf{x}) = \lambda(\mathbf{x})\nabla f(\mathbf{x}) \tag{3.64}$$

where $\mathbf{x} = (x, y)$ and $H(\mathbf{x}) = \nabla\nabla f(\mathbf{x})$ is the Hessian matrix of f at the point $\mathbf{x}$. Expression (3.64) could be derived also from the problem to find an extremal of (3.60) under the constraint $V = f(\mathbf{x}) =$ constant where λ is a Lagrangian multiplier. This expression tells that "a gradient extremal is a locus of point where the gradient of $f(\mathbf{x})$ is an eigenvector of the Hessian of $f(\mathbf{x})$".
We can define the eigenvalue of the Hessian corresponding to the direction of $\nabla f(\mathbf{x})$ as

$$\lambda = (\nabla f \cdot \nabla\nabla f \cdot \nabla f)/(\nabla f)^2 = (f_{xx}f_x^2 + 2f_{xy}f_x f_y + f_{yy}f_y^2)/(f_x^2 + f_y^2) \tag{3.65}$$

and the one corresponding to the direction of $\mathbf{e}$ as

$$\lambda' = (\mathbf{e} \cdot \nabla\nabla f \cdot \mathbf{e}) = (f_{xx}f_y^2 - 2f_{xy}f_x f_y + f_{yy}f_y^2)/(f_x^2 + f_y^2). \tag{3.66}$$

Hoffman *et al.* (1986) also provide a classification of gradient extremals according to the sign of (3.66) and an other quantity. First we ask ourselves how the surface changes when moving from a point on the gradient extremal perpendicularly to the gradient; if the ground rises we are walking in an actual *valley* while if it decreases we are precariously walking along a *ridge*. More precisely if $\lambda' > 0$ we are in a valley while if $\lambda' < 0$ we are on a ridge. Furthermore equation (3.63) allows to find gradient extremals hence two other cathegories can be distinguished according to whether these points define a maximum or a minimum of the gradient: if we are in a minimum these points indicate the gentlest slope, while if we are in a maximum they indicate the steepest slope. In this latter case we do not speak about valleys and ridges but about *cliffs* and *cirques* (specularly). This jargon is interestingly taken from the analysis of glaciers morphology. The distinction between the first group (valleys and ridges) and the second group (cliffs and cirques) depends on the sign of the second derivative of the norm of ∇f, i.e.

$$\lambda'' = (\mathbf{e} \cdot \nabla)(\mathbf{e} \cdot \nabla)(\nabla f)^2/2. \tag{3.67}$$

A number of manipulation that we do not report (see Hoffman *et al.* (1986) for the direct computation) yields the following expression:

$$\lambda'' = \lambda'(\lambda' - \lambda) + (f_{xxx}f_y + f_{yyy}f_x)f_x f_y + f_{xxy}f_y(f_y^2 - 2f_x^2) + f_{xyy}f_x(f_x^2 - 2f_y^2). \quad (3.68)$$

Before moving to our case we would like to observe that gradient extremals are not necessarily gradient flow curves. If this were so, the gradient would be tangent to the gradient extremal itself and gradient extremals would be a special class of steepest descent lines. One can prove that this depends on a cross third derivative as follows.
Points where the gradient is an eigenvector of the Hessian which define gradient extremals are characterized by the property that $\mathbf{g}(\mathbf{x}) = H\nabla f \wedge \nabla f = 0$. In components,

$$0 = \varepsilon_{ijk}(H\nabla f)_j(\nabla f)_k = \varepsilon_{ijk}H_{jl}(\nabla f)_l(\nabla f)_k = \varepsilon_{ijk}f_{,jl}f_{,l}f_{,k} \quad (3.69)$$

for $i = 1, 2, 3$ where ε_{ijk} denotes the Levi Civita symbol which vanishes if two indexes $(i, j, k = 1, 2, 3)$ are equal, is equal to $+1$ if the indexes are a cyclic permutation of $(1, 2, 3)$ (hence $(1, 2, 3), (3, 1, 2), (2, 3, 1)$) and -1 if the permutation is odd (hence $(3, 2, 1), (1, 3, 2), (2, 1, 3)$). Summation is understood among equal indexes, and the comma indicates differentiation with respect to that variable, e.g. $f_{,l} = \frac{\partial f}{\partial x_l}$.
Expression (3.69) is interesting only for $i = 3$ in fact. Indeed it is the compact notation for the explicit computation of $\mathbf{g}(\mathbf{x})$ which is:

$$\mathbf{g} = \mathbf{k}\,(f_{xx}f_x f_y + f_{xy}f_y^2 - f_{yx}f_x^2 - f_{yy}f_x f_y) \quad (3.70)$$

where $\mathbf{k} = (0, 0, 1)$ is the third vector of the standard basis in $\mathbb{R}^3$.
Let us now consider a gradient flow curve, that is a curve such that in all its points $\gamma(s) = \mathbf{x}(s)$ it holds $\dot\gamma = \big(\dot x(s), \dot y(s)\big) = \alpha(s)\nabla f(s)$. In all points where $g(\mathbf{x}) = 0$, let λ be the eigenvalue such that $H\nabla f = \lambda\,\nabla f$. Let us consider a gradient flow curve $\gamma(s)$, starting from a point $\mathbf{x}$ which is a gradient extremal point, with $g(\mathbf{x}) = 0$. We want to know if and when it is possible that all points of a gradient-flow curve belong to a gradient extremal, i.e. $g(\gamma(s)) = 0$ for all s. By differentiating (3.69) we obtain (highlighted in red the parts modified in the following line)

$$\begin{aligned}
\frac{dg(s)}{ds} &= \varepsilon_{ijk}(f_{,jlm}\dot{x}_m)f_{,l}f_{,k} + \varepsilon_{ijk}f_{,jl}(f_{,lm}\dot{x}_m)f_{,k} + \varepsilon_{ijk}f_{,jl}f_{,l}(f_{,km}\dot{x}_m) \\
&= \alpha\varepsilon_{ijk}\Big(f_{,jlm}f_{,m}f_{,l}f_{,k} + f_{,jl}\,f_{,lm}f_{,m}f_{,k} + f_{,jl}f_{,l}\,f_{,km}f_{,m}\Big) \\
&= \alpha\varepsilon_{ijk}\Big(f_{,jlm}f_{,m}f_{,l}f_{,k} + \lambda\, f_{,jl}f_{,l}f_{,k} + \lambda\, f_{,jl}f_{,l}f_{,k}\Big) \\
&= \alpha\varepsilon_{ijk}\Big(f_{,jlm}f_{,m}f_{,l}f_{,k} + \lambda^2\, f_{,j}f_{,k} + \lambda^2\, f_{,j}f_{,k}\Big) = \alpha\varepsilon_{ijk}f_{,jlm}f_{,m}f_{,l}f_{,k}
\end{aligned}$$

where x_m denotes one of the component of $\mathbf{x} = (x, y)$. If $\frac{dg(s)}{ds} = 0$ the property of gradient extremals is preserved for all points of the gradient flow curve. This expression tells that the third gradient of f establishes whether a gradient extremal is a gradient flow line as well. More precisely, an analysis of the result above shows that **given a gradient extremal point, a gradient flow line starting from the point will keep on being a gradient extremal point only if**

$$f_{,xxy} = 0, \quad (3.71)$$

where x is the gradient direction (so that $f_{,xx}$ is the second derivative in the gradient direction) and y is the direction orthogonal to the gradient.

3.5.2 Reaction paths on the Poincaré half-plane $\mathcal{H}$

We finally move to our context. As already mentioned the objective is finding the (non trivial) reaction path that connects the square point to the rhombic point on the energy surface described through expression (3.20) with the following combination of the parameters: $b_1/b_0 = 1$, $z_0 = \frac{1}{2} + i(\frac{\sqrt{3}}{2} + \delta)$ ($\delta \simeq 0.1$) and $\alpha_1 = 10$ (this value allows to respect (3.23); any other value in this range could be chosen because α_1 does not intervenes on the position and character of the stationary points of the function but it acts on the energy barriers as the previous sections explain).
First we want to formally prove that all "trivial" paths are actual gradient extremals. In this context trivial paths are represented by any geodesics connecting stationary points on the Poincaré half-plane $\mathcal{H}$, which we will prove to be gradient extremals (hence reaction paths according to the definition of Hoffman *et al* (1986)) for any potential conceived on the Poincaré half-plane. This result thus holds for the general class of strain energy functions with a single minimizer described in the first chapter, for the strain energy function (2.3) and for (3.20). In fact, the result that we are about to prove holds for any geodetic lines of the Poincaré half-plane, including those connecting any stationary point to infinity.
The objective is to prove that all geodetics composing the Dedekind Tessellation of the upper complex haf-plane $\mathcal{H}$ are gradient extremal curves for any potential energy invariant under the full symmetry group $GL(2,\mathbb{Z})$ of 2D lattices.
We are allowed to restrict ourselves to the fundamental domain $\mathcal{D}$ because of $GL(2,\mathbb{Z})$-invariance. Thus let us consider the boundary of the fundamental domain $\mathcal{D}$ consisting of the three geodesics $\gamma_1, \gamma_2, \gamma_3$ (see Fig. 3.20 on page 80) (not to be confused with γ_1 and γ_2 in (3.36) and (3.37) of subsection 3.2.2).
We will first prove that γ_1, γ_2 and γ_3 are always gradient flow curves of a function $\varphi(z) : \mathcal{H} \to \mathbb{R}$ which exhibits the correct invariance.
γ_1:
Let us consider two symmetrical points with respect to γ_1, P_1 and P_1'. They are related through the following Mobius tranformation:

$$z \mapsto -\bar{z}. \tag{3.72}$$

Hence $P_1 \mapsto -\bar{P}_1 = P_1'$. Since they are two equivalent points

$$\varphi(P_1) = \varphi(P_1') \quad \text{thus} \quad \varphi(z) = \varphi(-\bar{z}). \tag{3.73}$$

Identifying $\mathcal{H}$ with $\mathbb{R}^2$, (3.73) yields

$$\varphi(x,y) = \varphi(-x,y). \tag{3.74}$$

By differentiating (3.74) with respect to x:

$$\varphi_x(x,y) = -\varphi_x(-x,y). \tag{3.75}$$

Now, γ_1 lies along the straight line $x = 0$. Hence, if we evaluate expression (3.75) on γ_1 we obtain

$$\varphi_x(0, y) = -\varphi_x(-0, y) \to \varphi_x(0, y) = 0 \tag{3.76}$$

$\varphi_x(0, y) = 0$ precisely implies that γ_1 is a gradient flow curve. Among this expressions (3.74) is the most meaningful because it tells us that the energy has to be even with respect to x hence its derivative with respect to this component is odd, which necessarily implies that it vanishes in $x = 0$.

γ_2:
Let us consider two symmetrical points with respect to γ_2, P_2 and P_2'. They are related through the following Mobius tranformation:

$$z \mapsto -\bar{z} + 1. \tag{3.77}$$

Hence $P_2 \mapsto -\bar{P}_2 + 1 = P_2'$. Since they are two equivalent points

$$\varphi(P_2) = \varphi(P_2') \quad \text{thus} \quad \varphi(z) = \varphi(-\bar{z} + 1). \tag{3.78}$$

Identifying $\mathcal{H}$ with $\mathbb{R}^2$, (3.78) yields

$$\varphi(x, y) = \varphi(-x + 1, y). \tag{3.79}$$

By differentiating (3.79) with respect to x:

$$\varphi_x(x, y) = -\varphi_x(-x + 1, y). \tag{3.80}$$

Now, γ_2 lies along the straight line $x = 1/2$. Hence, if we evaluate expression (3.80) on γ_2 we obtain

$$\varphi_x(1/2, y) = -\varphi_x(1/2, y) \to \varphi_x(1/2, y) = 0. \tag{3.81}$$

$\varphi_x(1/2, y) = 0$ precisely implies that γ_2 is a gradient flow curve.

γ_3:
This curve connects the hexagonal point ρ to the square point i. Since it is a copy of the segment γ_3' of the straight line $x = 1/2$ that connects the square point ζ to the hexagonal point ρ, we can equivalently consider this segment for our computations. All couples of symmetrical points with respect to γ_3' are related through the Mobius tranformation in (3.78). Hence, we would proceed exactly as we did for γ_2 and we would obtain that γ_3' is a gradient flow curve, which also implies that γ_3 is a gradient flow curve.

In order to prove that γ_1, γ_2 and γ_3 are gradient extremals curve we rely on the result (3.71).
Let us consider γ_1:
We have proven that the gradient direction is y and the direction orthogonal to the gradient is x. Hence, we want to see if $\varphi_{,yyx} = 0$ on this line. This is equivalent to see if $\varphi_{,xyy} = 0$ because they are mixed partial derivatives.
By double differentiating (3.75) with respect to y we obtain

$$\varphi_{,xyy}(x, y) = -\varphi_{,xyy}(-x, y). \tag{3.82}$$

Thus $\varphi_{,xyy}(x,y)$ is an odd function with respect to x and it vanishes in $x=0$. Again, γ_1 precisely lies on the straight line $x=0$ hence we obtain $\varphi_{,xyy}=0$, which implies γ_1 is a gradient extremal.
We do not report the procedure for γ_2 and γ_3 because it retraces exactly the procedure for γ_1. In this case we need to double differentiate with respect to y expression (3.80) and we have to substitute $x=1/2$; we analogously obtain that γ_2 and γ_3 are gradient extremals curves. Hence all geodesics which constitute the boundary of $\mathcal{D}$ are gradient extremals; since the Poincaré half-plane $\mathcal{H}$ is covered by congruent copies of the fundamental domain all geodesics are gradient extremals for any potential living on this plane.
Whenever we aim to seek non trivial reaction paths we must rely on numerical calculations. In order to trace on the energy surface (3.20) those paths other than the geodesics of $\mathcal{H}$ connecting the square lattice and the rhombic lattice we look for those points satisfying (3.64). The result is reported in Fig. 3.21 on page 81, which represents the vector field of $-\nabla\varphi(\mathbf{x})$ in a portion of $\mathcal{H}$ including one square point, two equivalent rhombic points and one hexagonal point. We can observe that as expected the points belonging to the path connecting the square point and the rhombic point through the geodesics satisfy (3.64) and they can also be retrieved numerically. However in the close neighbourhood of the hexagonal point the path bifurcates identifying an untrod shortcut to reach the rhombic point. This result indicates that the minimum energy path between the two minimizers of (3.20) includes either passing through the hexagonal point or in its neighbourhood.
These reaction paths can be classified in light of section (3.5.1) through (3.66) and (3.67). In particular the most interesting result concerns the character of the tract of the path lying along the geodesic connecting the square point to the hexagonal point. From the behavior of λ' and λ'' on this tract (see Fig. 3.22 on page 81) we can infer that this gradient extremal is initially a valley and then it deforms into a ridge. This change of behavior occurs in correspondance with a so-called *valley-ridge inflection point*. We devote a brief paragraph to their definition:

Valley-ridge inflection points We report the traditional definition given by Quapp, Hirsch, Heidrich (2003): a valley-ridge inflection point (VRI) is that point in the configuration space where, orthogonally to the gradient, at least one main curvature of the potential energy surface becomes zero.
This definition implies the necessity to satisfy the following two conditions: 1. one eigenvalue of the Hessian must be zero, and 2. the gradient is orthogonal to the corresponding zero eigenvector. In other words, it has to be satisfied an orthogonality condition: $\mathbf{g}^T\mathbf{e}_0=0$, where $\mathbf{e}_0$ is the eigenvector of the Hessian with zero eigenvalue and $\mathbf{g}$ is the gradient. It should be remarked that VRI points are usually nonstationary points of the potential energy surface.

When we combine the free parameters of (3.20) as we already mentioned ($b_1/b_0=1$, $z_0=\frac{1}{2}+i(\frac{\sqrt{3}}{2}+\delta)$ with α_1 arbitrarly in the range identified by (3.23), e.g. $\alpha_1=10$) we find that $z_{VRI}=1/2+i\,y_{VRI}$ where $y_{VRI}\simeq 0.613$. This point exactly fulfills the definition given: when walking along the gradient extremal where z_{VRI} lies, we move from a convex (the valley) to a concave region (the ridge) and

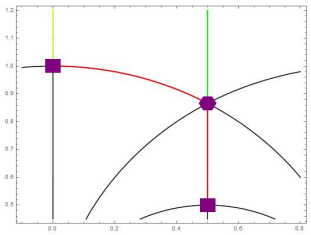

Figure 3.20: Indication of the geodesics that form the boundary of the fundamental domain $\mathcal{D}$. Two square points (i and $\zeta = 1/2(1+i)$) and one hexagonal point ($\rho = e^{i\pi/3}$) are indicated. The green line indicates the geodesic that connects ρ to $i\infty$. This is referred as γ_2 in the text. The yellow line indicates γ_1, which connects i to $i\infty$. The red curve indicates γ_3, which is the portion of the unit circle that connects i to ρ: it is equivalent to the red straight segment that connects ζ to ρ, which we labelled as γ_3' in the text.

the eigenvalue orthogonal to the gradient λ' has to change its sign as the definition requires.
On the other hand, the tracts of the reaction channels that connect the hexagonal point to the rhombic points are valleys and we do not find further valley-ridge inflection points.
It should be remarked that the numerical results obtained concerning the research of non-trivial reaction paths between stationary points of (3.20) has provided paths passing in the strict neighbourhood of the hexagonal point because the energy surface is rather flat around this point when combining the free parameters of (3.20) as mentioned ($b_1/b_0 = 1$, $z_0 = \frac{1}{2} + i(\frac{\sqrt{3}}{2} + \delta), \alpha_1 = 10$). Different combinations of the free parameters deform the energy landscape and accentuate its mountainous character also in the vicinity of ρ; in this case non-trivial reaction paths will probably avoid passing in the neighbourhood of ρ by crossing the internal part of the fundamental domain $\mathcal{D}$.

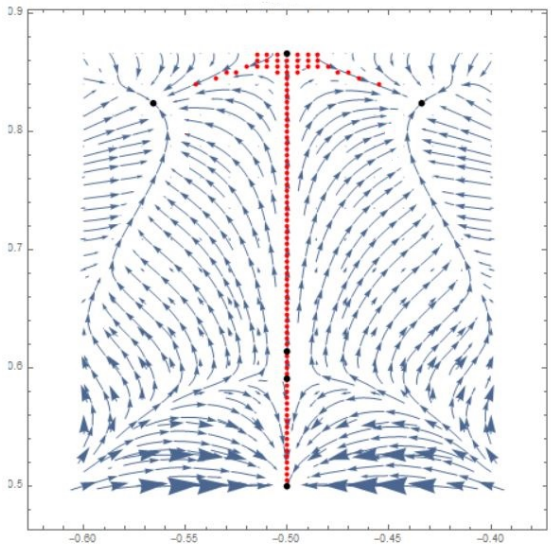

Figure 3.21: Vector field of $-\nabla\varphi(\mathbf{x})$ in a portion of $\mathcal{H}$ where φ is (3.20). The black points indicate from the bottom up a square point corresponding to $z = -1/2 + i1/2$, the saddle point $z = -1/2 + iy_{SP}$ where $y_{SP} \simeq 0.59$, the valley-ridge inflection point (see main text for the definition) $z = -1/2 + iy_{VRI}$ where $y_{VRI} \simeq 0.613$, two rhombic points equivalent to $z_0 = -1/2 + i(\sqrt{3}/2 + \delta)$ where $\delta \simeq 0.1$ and one hexagonal point $z = -1/2 + \sqrt{3}/2$. The swarm of red dots indicate the reaction path from the "reactant" which corresponds to the square point to the "product phases" which correspond to the equivalent rhombic points. In the neighbourhood of the hexagonal point the unique reaction channel bifurcates identifying two shortcuts to reach to rhombic points that allow to avoid passing through the hexagonal point (even though in its vicinity).

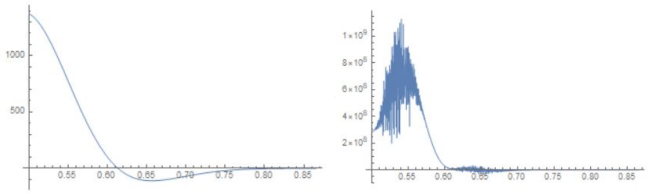

(a) λ' **(b)** λ''

Figure 3.22: Behavior of λ' (3.66) and λ'' (3.67) along the tract of the reaction channel that lies on the geodetic connecting the square point to the hexagonal point. λ' changes its sign in correspondance with the valley-ridge inflection point z_{VRI} while λ'' is always positive. The oscillations of λ'' are due to the fact that its computation requires third order derivatives of (3.20), which are obtained numerically and thus provoke the observable lack of precision.

Chapter 4

Numerical analysis

The last chapter is devoted to numerically validate the model built in the second chapter to predict reconstructive phase transformations.
We consider a boundary value problem which describes the equilibrium of an hyperelastic body in the context of finite, non-linear elasto-plasticity. The strain energy function which controls the problem is (1.15) where the expression for σ_v is (1.17) and the expression for σ_d is (2.3).
In each single simulation we consider the temperature as a fixed parameter. This implies fixing β, which controls the character of the stationary points of (2.3): depending on its value the landscape changes considerably as the second chapter witnesses hence the equilibrium problem will be solved by fixing β at different values; we do not replicate the phase change of a reconstructive phase transformations but rather analyze the elasto-plastic deformations at different values of the temperature.
In the first section we present the theoretical problem to solve.
In the second section we modify the problem in order to make it solvable through a finite elements method and we describe the iterative procedure that has been applied to the resulting equation.
The third section analyzes the results obtained by distinguishing between the simulations performed at a fixed value $\beta \leq 0$ and those performed at a fixed value $\beta > 0$ in order to explore both the case of a single minimizer in the fundamental domain $\mathcal{D}$ corresponding to i and the case of two minimizers, i and ρ.
The original finite elements code was written by E. Arbib and it was suitably modified in order to host expression (2.3) for the distorsive part of the strain energy function.

4.1 The theoretical problem

Let us consider a continuum body whose reference configuration at time t_0 is an open, bounded and connected subset Ω of $\mathbb{R}^2$ (we consider a two dimensional setting). Given a point in the reference configuration $\mathbf{X}$ this corresponds to a point in the current configuration through the relation $\mathbf{x} = \mathbf{x}(\mathbf{X}, t)$. The deformation gradient is then defined as $\mathbf{F} = \nabla \mathbf{x} = \frac{\partial \mathbf{x}}{\partial \mathbf{X}}$.
Since the displacement field is defined as $\mathbf{u} = \mathbf{x} - \mathbf{X}$ it holds that $\mathbf{F} = \nabla \mathbf{u} + \mathbf{I}$.
For problems where inertial effects are negligible, balance of linear momentum leads

to the equation of equilbrium

$$\mathrm{Div}(\mathbf{T}) = 0 \quad \text{in} \quad \Omega_t \tag{4.1}$$

in absence of body forces, where $\mathbf{T}$ is the Cauchy stress tensor and Ω_t is the current configuration. This tensor measures the contact force per unit area in the *deformed* (current) configuration, which is not known a priori. Hence it is more convenient to express the equilibrium equation in terms of a tensor that gives the contact force per unit area in the *undeformed* (reference) configuration Ω. This tensor is the First Piola Kirchhoff stress tensor, defined by

$$\mathbf{S} = \det\mathbf{F}\,\mathbf{T}\,\mathbf{F}^{-\mathrm{T}}. \tag{4.2}$$

Through $\mathbf{S}$ we can write the equilibrium equation in the reference configuration:

$$\mathrm{Div}(\mathbf{S}) = 0 \quad \text{in} \quad \Omega. \tag{4.3}$$

Since we consider an hyperelastic material $\mathbf{S}$ can be obtained by differentiating the strain energy function with respect to $\mathbf{F}$:

$$\mathbf{S} = \frac{\partial \sigma}{\partial \mathbf{F}} \tag{4.4}$$

where σ is the sum of (1.17) and (2.3) formulated in terms of the deformation gradient $\mathbf{F}$.
The boundary value problem of finite elasticity is obtained by adjoining to this expression suitable boundary conditions which prescribe either displacement or traction (or both) on $\partial\mathcal{B}$. The problem consists in finding the displacement $\mathbf{u}$ such that

$$\begin{cases} \mathrm{Div}(\mathbf{S}) = 0 \quad \text{in} \quad \Omega \\ \mathbf{u} = \tilde{\mathbf{u}} \quad \text{on} \quad \Gamma_D \\ \mathbf{S}\mathbf{n} = \mathbf{g} \quad \text{on} \quad \Gamma_N \end{cases} \tag{4.5}$$

where Γ_D and Γ_N are such that

$$\Omega = \Gamma_D \cup \Gamma_N. \tag{4.6}$$

The problem (4.4) can be expressed in terms of components once we chose an orthonormal basis of $\mathbb{R}^2$. We need to find the displacement $\mathbf{u} = (u_1, u_2)$ where $u_1 : \Omega \to \mathbb{R}$ and $u_2 : \Omega \to \mathbb{R}$ such that

$$\begin{cases} \frac{\partial S_{ij}}{\partial x_j}(u_1, u_2) = 0 \quad \text{in} \quad \Omega \\ u_i = \tilde{u}_i \quad \text{on} \quad \Gamma_D \\ S_{ij} n_j = g_i \quad \text{on} \quad \Gamma_N \end{cases} \tag{4.7}$$

where $i = 1, 2$ and S_{ij} are the components of the First Piola Kirchoff stress tensor expressed through the orthonormal basis $\{\mathbf{i}_1, \mathbf{i}_2\}$.

4.2 Finite-element methods implementation

Problem (8.2) is a non linear system of partial differential equations. It is rendered more suitable for solution by the finite element method if it is recast in a *weak* form. We will first find the weak form of the fist equation in (4.5) and then we will write it in terms of components.
Let us consider a suitable test function $\mathbf{v} = (v_1, v_2)$, where v_1 and v_2 both belong to the following functional space

$$V = H^1_{0,\Gamma_D}(\Omega) = \left\{ v \in H^1(\Omega) \,:\, v|_{\Gamma_D} = 0 \right\}. \tag{4.8}$$

Furthermore let us suppose that $\tilde{\mathbf{u}} = (\tilde{u_1}, \tilde{u_2})$ is such that $\tilde{u_1}, \tilde{u_2} \in H^{1/2}(\Gamma_D)$ where

$$H^{1/2}(\Gamma_D) = \left\{ \tilde{u} \in L^2(\Gamma_D) : \exists\, u \in H^1(\Omega) \,\text{such that}\, \gamma_0 u = \tilde{u} \right\} \tag{4.9}$$

where $\gamma_0 : H^1(\Omega) \mapsto L^2(\Gamma_D)$ is the trace operator. Finally $\mathbf{g} = (g_1, g_2)$ is such that $g_1, g_2 \in L^2(\Gamma_N)$ while the Sobolev space for the components of the solution $\mathbf{u} = (u_1, u_2)$ is $H^1(\Omega)$.
By multiplying the first equation in (4.5) for the test function v, then integrating over the domain Ω and applying the divergence theorem we obtain:

$$\int_\Omega \mathbf{S} : \nabla \mathbf{v} \, d\,\Omega = \int_{\Gamma_N} \mathbf{v}\,\mathbf{g}\, ds. \tag{4.10}$$

The weak formulation of the problem is then given in terms of components:

Given $\tilde{u_1}, \tilde{u_2} \in H^{1/2}(\Gamma_D)$, $g_1, g_2 \in L^2(\Gamma_N)$, find $u_1, u_2 \in H^1(\Omega)$ such that

$$\int_\Omega S_{ij}(u_1, u_2) \frac{\partial v_i}{\partial x_j} \, d\,\Omega = \int_{\Gamma_N} v_i \, g_i \, ds \quad \forall\, v_1, v_2 \in V \tag{4.11}$$

$$u_i = \tilde{u_i} \quad \text{on} \quad \Gamma_D \quad \text{in the sense of trace.} \tag{4.12}$$

By exploiting the hypothesis of hyperelasticity we can rewrite (4.11) as:

$$\int_\Omega \frac{\partial \sigma}{\partial F_{ij}}(u_1, u_2) \frac{\partial v_i}{\partial x_j} \, d\,\Omega = \int_{\Gamma_N} v_i \, g_i \, ds \quad \forall\, v_1, v_2 \in V. \tag{4.13}$$

However before proceeding to the discretization we want to further modify (4.13). We would like to integrate Dirichlet condition (4.12) into the equation (4.13) by introducing a proper lifting. In this way we can look for the solution in an actual subspace of $H^1(\Omega)$ (the behavior of (u_1, u_2) on the Dirichlet boundary expressed through (4.12) sentence the components of the solution to belong to a space which is not close with respect to linear combinations of its elements).
Thus we assume to know two lifting functions $r_{\tilde{u}_1}, r_{\tilde{u}_2} \in H^1(\Omega)$ such that

$$r_{\tilde{u}_1}|_{\Gamma_D} = u_1 \quad r_{\tilde{u}_2}|_{\Gamma_D} = u_2. \tag{4.14}$$

The spirit of the lifting materializes when introducing two functions $\mathring{u}_1 = u_1 - r_{\tilde{u}_1}$ and $\mathring{u}_2 = u_2 - r_{\tilde{u}_2}$. We observe that $\mathring{u}_i|_{\Gamma_D} = 0$ $(i = 1, 2)$ hence $\mathring{u}_1, \mathring{u}_2$ both belong to V defined in (4.8).

The problem finally is:

Given $g_1, g_2 \in L^2(\Gamma_N)$, find $\mathring{u}_1, \mathring{u}_2 \in V$ such that

$$\int_\Omega \frac{\partial \sigma}{\partial F_{ij}}(\mathring{u}_1 + r_{\tilde{u}_1}, \mathring{u}_2 + r_{\tilde{u}_2})\frac{\partial v_i}{\partial x_j}\, d\,\Omega = \int_{\Gamma_N} v_i\, g_i\, ds \quad \forall\, v_1, v_2 \in V. \tag{4.15}$$

We are now ready to discretize the problem through a finite element approximation. First we introduce a tessellation of the domain Ω through non-overlapping triangles. The discretized domain is

$$\Omega_h = int(\bigcup_{K \in \mathcal{T}_h} K) \tag{4.16}$$

where *int* indicate the inner part of the set. Ω_h precisely coincide with Ω only if Ω is a polygonal domain; in all other case we introduce an approximation error due to the rectification of $\partial\Omega$. The parameter h defines the grid density; given h_K=diam(K) for each $K \in \mathcal{T}_h$, where diam(K)=max$_{x,y\in K}|x-y|$, h is defined as $h = \max_{K\in\mathcal{T}_h} h_k$.
The definition of the discretized problem also requires introducing the finite element space:

$$X_k^r = \left\{ v_h \in C^0(\bar{\Omega}) : v_h|_K \in \mathbb{P}_r, \forall K \in \mathcal{T}_h \right\} \tag{4.17}$$

i.e. the space of the globally continuous functions which are polynomials of degree r. We also define $V_h^r = \mathring{X}_k^r = X_k^r \cap H^1_{0,\Gamma_D}$. Finally the problem (4.15) can be rewritten as:

Given $g_1, g_2 \in L^2(\Gamma_N)$, find $\mathring{u}_{h,1}, \mathring{u}_{h,2} \in V_h^r$ such that

$$\int_\Omega \frac{\partial \sigma}{\partial F_{ij}}(\mathring{u}_{h,1} + r_{h,\tilde{u}_1}, \mathring{u}_{h,2} + r_{h,\tilde{u}_2})\frac{\partial v_{h,i}}{\partial x_j}\, d\,\Omega = \int_{\Gamma_N} v_{h,i}\, g_i\, ds \quad \forall\, v_{h,1}, v_{h,2} \in V_h^r \tag{4.18}$$

where $r_{h,\tilde{u}_i} \in X_h^r$ is the approximated lifting.
Problem (4.18) contains a further pitfall being non-linear. Non-linear problems are usually treated through iterative methods, which involve using an initial guess to generate a sequence of solutions of a number of linear problems where the non-linearity is suppressed by introducing the solution of the previous iterative step. The sequence stops when the chosen termination criteria is satisfied.
Among these methods it stands the gradient descent algorithm, which implies interpreting our problem as a minimization problem of an objective functional whose gradient (in terms of Fréchet derivatives) is precisely expression (4.18) once we moved every term on the left-hand side. The i-th component of the gradient is

$$G_i(\mathring{u}_{h,1}, \mathring{u}_{h,2}) = \int_\Omega \frac{\partial \sigma}{\partial F_{ij}}(\mathring{u}_{h,1}+r_{h,\tilde{u}_1}, \mathring{u}_{h,2}+r_{h,\tilde{u}_2})\frac{\partial v_{h,i}}{\partial x_j}\, d\,\Omega - \int_{\Gamma_N} v_{h,i}\, g_i\, ds \quad \forall\, v_{h,1}, v_{h,2} \in V_h^r \tag{4.19}$$

where $i = 1, 2$.
Thus applying gradient descent method to our problem means applying the following procedure to generate a sequence of pair $\left\{(\mathring{u}_{h,1}^n, \mathring{u}_{h,2}^n)\right\}$:

1. initialize the pair $\mathring{u}_{h,1}^0, \mathring{u}_{h,2}^0 \in V_h^r$

2. the solution for the n-th iterative step can be obtained from $\mathring{u}_{h,1}^{n-1}, \mathring{u}_{h,2}^{n-1}$ as

$$\mathring{u}_{h,i}^{n} = \mathring{u}_{h,i}^{n-1} - \alpha^n \, d_i^{\,n-1} \tag{4.20}$$

where α^n is the step size at the n-th iteration which is chosen according to the Wolfe condition and $d_i^{\,n-1}$ is the i-th component of the vector which indicates the direction of the step. We will later explain precisely how to compute both these quantities.

3. update $n = n + 1$

The iterative cycle stops when the following termination criterion is satisfied :

$$||\text{residual at } n\text{-th step}|| = ||\nabla G^n|| = \sqrt{\nabla G^{n\,T} \nabla G^n} < \varepsilon \tag{4.21}$$

where $\nabla G^{\,n} = (G_1(\mathring{u}_{h,1}^n, \mathring{u}_{h,2}^n), G_2(\mathring{u}_{h,1}^n, \mathring{u}_{h,2}^n))$ and ε is a fixed tolerance.

The vector which indicates the moving direction at the n-th step $\mathbf{d}^{\,n-1} = (d_1^{\,n-1}, d_2^{\,n-1})$ can be obtained as follows

$$\mathbf{d}^{\,n-1} = \mathbf{M}^{-1} \, \nabla G(\mathring{u}_{h,1}^{n-1}, \mathring{u}_{h,2}^{n-1}) \tag{4.22}$$

where $\nabla G^{\,n-1} = (G_1(\mathring{u}_{h,1}^{n-1}, \mathring{u}_{h,2}^{n-1}), G_2(\mathring{u}_{h,1}^{n-1}, \mathring{u}_{h,2}^{n-1}))$ and $\mathbf{M}$ is a preconditioner, which has to be a symmetric positive-definite matrix. We necessarily have to use a preconditioner because we deal with non convex potential. On the other hand the step size α^n is obtained through Wolfe conditions according to the following inequalities

$$G(\mathring{\mathbf{u}}_h^{n-1} - \alpha^n \, \mathbf{d}^{\,n-1}) \leq G(\mathring{\mathbf{u}}_h^{n-1}) - c_1 \alpha^n (\nabla G^{\,n})^T \mathbf{d}^{\,n-1} \tag{4.23}$$

where c_1 is usually chosen to be quite small for instance $c_1 = 10^{-4}$ and G is the objective functional we are trying to minimize:

$$G = \int_\Omega \sigma(\mathbf{F}) \, d\,\Omega - \int_{\Gamma_N} \mathbf{g} \cdot \mathbf{u}_h \, ds \tag{4.24}$$

where $\mathbf{g} = (g_1, g_2)$ and $\mathbf{F}$ is the deformation gradient associated to the discretized displacement field $\mathbf{u}_h$ through the relation $\mathbf{F} = \nabla \mathbf{u}_h + \mathbf{I}$.
Before proceeding to the results we devote two brief subsections to discussing both the implementation of the preconditioner and the approximation of the Klein Invariant J, which is the raw material to construct the distorsive component σ_d (see expression (2.3)) of the strain energy function that we want to test.

4.2.1 The choice of the preconditioner M

In order to provide a proper justification for the choice of the preconditioning matrix $\mathbf{M}$ (which we did not explicit yet) let us consider the non-discretized problem in the form (4.13). If we apply directly the finite elements discretization to this problem, without incorporating in the problem Dirichlet boundary condition through a lifting, we obtain the following problem:

Given $\mathbf{g} \in L^2(\Gamma_N;\mathbb{R}^2)$, find $\mathbf{u}_h \in X_h^r(\Omega;\mathbb{R}^2)$ such that

$$\int_\Omega \frac{\partial \sigma}{\partial \mathbf{F}}(\mathbf{I}+\nabla \mathbf{u}_h) : \nabla \mathbf{v}_h \, d\Omega = \int_{\Gamma_N} \mathbf{g}\cdot \mathbf{v}_h \, ds \quad \forall \, \mathbf{v}_h \in V_h^r(\Omega;\mathbb{R}^2) \tag{4.25}$$

$$\mathbf{u}_h = \tilde{\mathbf{u}} \quad \text{on} \quad \Gamma_D \tag{4.26}$$

where $V_h^r(\Omega;\mathbb{R}^2) = X_h^r(\Omega;\mathbb{R}^2) \cap H^1_{0,\Gamma_D}(\Omega;\mathbb{R}^2)$. Notice that this formulation is not written in terms of components as (4.18), hence we need to use spaces for vector-valued functions. Also, the dependence of the strain energy function on the discretized displacement field has been made explicit through the relation $\mathbf{F} = \nabla \mathbf{u}_h + \mathbf{I}$.
We want to give an estimate of the condition number of the stiffness matrix associated to problem (4.25) in order to provide a preconditioning matrix able to reduce it.
The stiffness matrix of this problem can be obtained through linearization:

Given $\mathbf{g} \in L^2(\Gamma_N;\mathbb{R}^2)$ and $\mathbf{u}_h^{n-1} \in X_h^r(\Omega;\mathbb{R}^2)$, find $\mathbf{u}_h^n \in X_h^r(\Omega;\mathbb{R}^2)$ such that

$$\begin{aligned}\int_\Omega \frac{\partial^2 \sigma}{\partial \mathbf{F}^2}(\mathbf{I}+\nabla \mathbf{u}_h^{n-1}) : (\nabla \mathbf{u}_h^n \otimes \nabla \mathbf{v}_h) \, d\Omega = &\int_{\Gamma_N} \mathbf{g}\cdot \mathbf{v}_h \, ds - \\ &\int_\Omega \frac{\partial \sigma}{\partial \mathbf{F}}(\mathbf{I}+\nabla \mathbf{u}_h^{n-1}) : \nabla \mathbf{v}_h \, d\Omega\end{aligned} \tag{4.27}$$

$$\mathbf{u}_h = \tilde{\mathbf{u}} \quad \text{on} \quad \Gamma_D \tag{4.28}$$

$\forall \, \mathbf{v}_h \in V_h^r(\Omega;\mathbb{R}^2)$.

Then, given a basis $\left\{\boldsymbol{\varphi}^{(i)}\right\}$ for the finite elements space $X_h^r(\Omega;\mathbb{R}^2)$, the stiffness matrix $\mathbf{A}$ of the problem has components:

$$A_{ij} = \int_\Omega \frac{\partial^2 \sigma}{\partial F_{ls} \partial F_{kt}}(\mathbf{I}+\nabla \mathbf{u}_h^{n-1}) \frac{\partial \varphi_l^{(i)}}{\partial x_s} \frac{\partial \varphi_k^{(j)}}{\partial x_t} \, d\Omega \tag{4.29}$$

which can be rewritten as

$$A_{ij} = \int_\Omega H_\sigma(\mathbf{I}+\nabla \mathbf{u}_h^{n-1}) \, \nabla \boldsymbol{\varphi}^{(i)} \cdot \nabla \boldsymbol{\varphi}^{(j)} \, d\Omega \tag{4.30}$$

where H_σ is the following 4×4 matrix given by:

$$H_\sigma = \begin{bmatrix} \frac{\partial^2 \sigma}{\partial F_{11}\partial F_{11}} & \frac{\partial^2 \sigma}{\partial F_{11}\partial F_{12}} & \frac{\partial^2 \sigma}{\partial F_{11}\partial F_{21}} & \frac{\partial^2 \sigma}{\partial F_{11}\partial F_{22}} \\ \frac{\partial^2 \sigma}{\partial F_{12}\partial F_{11}} & \ddots & \ddots & \vdots \\ \vdots & \ddots & \ddots & \vdots \\ \frac{\partial^2 \sigma}{\partial F_{22}\partial F_{11}} & \frac{\partial^2 \sigma}{\partial F_{22}\partial F_{12}} & \cdots & \frac{\partial^2 \sigma}{\partial F_{22}\partial F_{22}} \end{bmatrix} \tag{4.31}$$

while $\nabla\boldsymbol{\varphi}^{(i)}$ is a vector belonging to $\mathbb{R}^4$ such that:

$$\nabla\boldsymbol{\varphi}^{(i)} = \begin{bmatrix} \frac{\varphi_1^{(i)}}{\partial x_1} \\ \frac{\varphi_1^{(i)}}{\partial x_2} \\ \frac{\varphi_2^{(i)}}{\partial x_1} \\ \frac{\varphi_2^{(i)}}{\partial x_2} \end{bmatrix}. \tag{4.32}$$

In order to estimate the condition number $k(\mathbf{A})$, we remark that for every K_i (we add a subscript to make the notation clearere) of the triangulation $\mathcal{T}_h$ the quantity $H_\sigma(\mathbf{I}+\nabla\mathbf{u}_h^{n-1}) := H_\sigma$ is constant and we label $\{\lambda_i, \Lambda_i\}$ its minimum and maximum eigenvalues. Then, if $\mathbf{t}$ is a generic vector of dimension $\dim(X_h^r(\Omega;\mathbb{R}^2))$, it holds:

$$\mathbf{A}\mathbf{t}\cdot\mathbf{t} = t_i\, t_j \int_\Omega H_\sigma(\mathbf{I}+\nabla\mathbf{u}_h^{n-1})\,\nabla\boldsymbol{\varphi}^{(i)}\cdot\nabla\boldsymbol{\varphi}^{(j)}\,d\,\Omega. \tag{4.33}$$

Thus:

$$\min_i \lambda_i \int_\Omega |\nabla(\boldsymbol{\varphi}^{(i)}t_i)|^2\,d\,\Omega \le \mathbf{A}\mathbf{t}\cdot\mathbf{t} \le \max_i \Lambda_i \int_\Omega |\nabla(\boldsymbol{\varphi}^{(j)}t_j)|^2\,d\,\Omega. \tag{4.34}$$

Hence:

$$k(\mathbf{A}) \le \frac{\max_i \Lambda_i}{\min_i \lambda_i}. \tag{4.35}$$

In the implementation of the code Arbib proposes the preconditioning matrix $\mathbf{M}$ such that its components are:

$$M_{ij} = \int_\Omega \frac{\mathrm{tr}(H_\sigma)}{4}\nabla\boldsymbol{\varphi}^{(i)}\cdot\nabla\boldsymbol{\varphi}^{(j)}\,d\,\Omega. \tag{4.36}$$

Hence, we proceed to estimate $k(\mathbf{M}^{-1}\mathbf{A})$. Since $\lambda_i \le \frac{\mathrm{tr}(H_\sigma)}{4}\big|_{K_i} \le \Lambda_i$ for all i, the following inequalities hold:

$$\begin{aligned} \mathbf{A}\mathbf{t}\cdot\mathbf{t} = &\int_\Omega H_\sigma(\nabla\boldsymbol{\varphi}^{(i)}t_i)\cdot(\nabla\boldsymbol{\varphi}^{(j)}t_j) = \\ &\sum_S \int_{K_S} H_\sigma(\nabla\boldsymbol{\varphi}^{(i)}t_i)\cdot(\nabla\boldsymbol{\varphi}^{(j)}t_j) \ge \\ &\sum_j \int_{K_j} \lambda_j|\nabla\boldsymbol{\varphi}^{(i)}t_i|^2 = \\ &\sum_j \frac{\lambda_j}{c_j}\int_{K_j} c_j|\nabla(\boldsymbol{\varphi}^{(i)}t_i)|^2 \ge \\ &(\min_j \frac{\lambda_j}{c_j})\sum_j \int_{K_j} c_j|\nabla(\boldsymbol{\varphi}^{(i)}t_i)|^2 \ge \\ &\tau_1\,\mathbf{M}\,\mathbf{t}\cdot\mathbf{t} \end{aligned} \tag{4.37}$$

where $\frac{\mathrm{tr}(H_\sigma)}{4}\big|_{K_i} = c_i$ and $\min_j \frac{\lambda_j}{c_j} = \tau_1$.
Through an analogous procedure we also obtain that:

$$\mathbf{A}\mathbf{t}\cdot\mathbf{t} \le \tau_2\,\mathbf{M}\,\mathbf{t}\cdot\mathbf{t} \quad \text{where} \quad \tau_2 = \max_j \frac{\Lambda_j}{c_j}. \tag{4.38}$$

Hence the estimate of the condition number gives:

$$k(\mathbf{M}^{-1}\mathbf{A}) \leq \frac{\tau_2}{\tau_1} = \max_j \frac{\Lambda_j}{\lambda_j} \tag{4.39}$$

which is a better estimate than (4.35), thus the choice (4.36) for the conditioning matrix $\mathbf{M}$ is a good choice.

4.2.2 Approximation of the Klein Invariant J

Klein's function J is defined as the combination of two infinite sums (see expression (1.42)). However in order to approximate this function we rely on a result presented in Apostol (1976) where it is proven that if $z \in \mathcal{H}$ we have the following Fourier expansion of J:

$$12^3 J(z) = e^{-2\pi i z} + 744 + \sum_{n=1}^{\infty} c(n) e^{2\pi i n z} \tag{4.40}$$

where the $c(n)$ are integers. The first one hundred coefficients were calculated in 1953 by Van Wijngaarden. Being J analytic in $\mathcal{H}$ its Fourier expansion converges pointwise.
Thus in the numerical resolution of our problem we use the Fourier expansion (4.40) truncated at the n-th term, which we label J_n. In particular we used J_{604} (we choose such an n because it corresponds to the maximum number of terms acceptable in a real variable by the solver Freefem++ 3.51).

4.3 Numerical results

In this section we report the results obtained from the resolution of (4.18) under the following hypotheses:

1. The strain energy function $\sigma(\mathbf{F})$ corresponds to the expression constructed to model reconstructive martensitic phase tranformations, which we express in terms of the metric $\mathbf{C}$:

$$\sigma_{rec}(\mathbf{C}, \vartheta) = \sigma_v(\det \mathbf{C}, \vartheta) + \sigma_{d,rec}(\bar{\mathbf{C}}, \beta(\vartheta)) \tag{4.41}$$

$$\sigma_v(\det \mathbf{C}, \vartheta) = \nu \left(\det \mathbf{C} - \frac{\vartheta}{\vartheta_0} \log(\det \mathbf{C}) \right) \tag{4.42}$$

$$\sigma_{d,rec}(\bar{\mathbf{C}}, \beta(\vartheta)) = |J_n(\hat{z}(\bar{\mathbf{C}})) - 1| + \beta(\vartheta) |J_n(\hat{z}(\bar{\mathbf{C}}))|^{\frac{2}{3}}. \tag{4.43}$$

In particulare we choose $\mu = 1$ and $\nu = 100$. Notice that we stressed the dependence of β on the temperature ϑ (from chapter 2 we know that β is an increasing function of ϑ). However as previously mentioned in the introduction of this chapter the simulations were performed considering the temperature, hence also β, as a fixed parameter. Thus the functions used for problem (4.18) are:

$$\sigma_{rec}(\mathbf{C}) = \sigma_v(\det \mathbf{C}) + \sigma_{d,rec}(\bar{\mathbf{C}}, \beta_0)) \tag{4.44}$$

$$\sigma_v(\det \mathbf{C}) = \nu \left(\det \mathbf{C} - \log\left(\det \mathbf{C}\right)\right) \tag{4.45}$$

$$\sigma_{d,rec}(\bar{\mathbf{C}}, \beta) = |J_n(\hat{z}(\bar{\mathbf{C}})) - 1| + \beta |J_n(\hat{z}(\bar{\mathbf{C}}))|^{\frac{2}{3}} \tag{4.46}$$

where $\beta = \beta(\vartheta_0)$ is suitably fixed at a different value in each simulation.

2. The reference configuration is a rectangle-shaped body Ω

$$\Omega = (0, 1) \times (0, 1.4) \subset \mathbb{R}^2 \tag{4.47}$$

which contains an initially homogeneus material in which the underlying lattice is square, defect free and aligned with the body sides. Hence the undeformed state corresponds to $z_0 = i$. According to the Cauchy-Born hypothesis (1.14) the lattice metric represents the right Cauchy-Green tensor provided that the reference basis is orthonormal. Since the basis associated with the underformed configuration $z_0 = i$ is precisely orthonormal then $C_{ij} = (\mathbf{F}\mathbf{F}^T)_{ij}$ (this would not hold if $z_0 = \rho$; in this case we should rewrite the basis of the underformed configuration in terms of an orthormal basis).

3. The triangulation $\mathcal{T}_h$ of the domain Ω is obtained by imposing 50 vertices on the top and bottom sides of the rectangle and 70 vertices on the remaining two sides of the rectangle (see Fig. 4.1 on page 94).

4. The finite elements space chosen is X_k^1

5. We apply a quasi-static loading on the top side of the body to simulate a simple shear stress condition. In particular we impose Dirichlet boundary conditions on the top and bottom sides of the body while the remaining two sides are left free. Hence

$$\Gamma_D = \left\{(x_1, x_2) \in \mathbb{R}^2 : x_2 = 0 \vee x_2 = 1.4\right\} \tag{4.48}$$

$$\Gamma_N = \left\{(x_1, x_2) \in \mathbb{R}^2 : x_1 = 0 \vee x_1 = 1\right\}. \tag{4.49}$$

Since the two sides of the rectangles belonging to Γ_N are left free, we impose $g_i = 0$, $i = 1, 2$. Dirichlet conditions are integrated through the lifting; in particular in order to impose a shear along a primary direction we impose:

$$r_{h,\tilde{u}_1} = \gamma x_2 \quad r_{h,\tilde{u}_2} = 0 \tag{4.50}$$

where γ is the shear parameter. When $\gamma = 0$ we recover the reference state $z_0 = i$ because no deformation is imposed, while $\gamma = 1$ corresponds to a new configuration such that the vectors of the lattice basis form a $\pi/4$ angle: the new state is equivalent to $z = i + 1$ on the Poincaré half-plane $\mathcal{H}$, which is the adjacent equilibrium sheared-square configuration. As section (2.4) of chapter 2 explains, imposing such a deformation allows to explore the plastic domain. In our simulations γ is initially equal to 0.1 and then it is gradually increased of a percentage point in order to accurately reproduce a quasi-static loading. In this way we explore a part of the elastic regime and more importantly the plastic-flow initiation as γ in our simulations never reaches the value $\gamma = 1$ but at most $\gamma = 0.3$.

However, this value is high enough to observe at least a partial plastification of the body as the end of the elastic regime tipically takes place at a value of γ in the range $\gamma \in [0.065, 0.17]$. This value depends on the value of β and we label it as $\gamma_{first\,aval}$ where *aval* indicates "avalanche": at this value for the first time a number of scouting cells abandons the basin corresponding to $z = i$ to explore the other dips of the energetic territory. This primary large plastification event triggers a sequence of smaller plastification events. We will analyze extensively these phenomena in the following section.
Before moving to the analysis though it is important to make a remark. As (4.46) is a non-convex potential, rather periodic, it does not hold any theorem of uniqueness of the solution. Different parts of the system could find different solutions solving the equilibrium problem (4.18), where we label as "different" two solutions corresponding to two different basins of the energy. Hence, we are looking for one among the possible equilibrium solutions: in particular, for each γ the algorithm searches for the equilibrium solution closest to the one found at the preceeding γ. Since we will observe that the relevant quantities which can be obtained by solving the equilibrium problem for every γ are characterized by abrupt jumps, we can infer that the equilibrium configuration does not depend continuously on the loading parameter γ.

For the time being the last observations allow to remark upon the influence of the parameter β on the plastification mode chosen by the body. As a matter of fact β controls the character and the position of the stationary points of (4.46) by either changing the depth of the basins or even generating new dips other than the square points as section (2.3) of chapter 2 extensively tells.
This parameter can arbitrarly vary in the range $\beta \in [-3/2, 3/2)$, which guarantees at least the existence of one basin corresponding to the square configuration (one in the fundamental domain $\mathcal{D}$, together with the infinitely many equivalent square points). In this range the energy (4.46) remarkably changes its behavior according to whether β is positive or negative; in particular when $-3/2 \leq \beta \leq 0$ the square points are the unique equilbrium configurations while when $0 < \beta < 3/2$ further equilibrium positions generate corresponding to the hexagonal points. In the presentation and analysis of the results we will usually consider separately positive and negative values of β as they correspond to quite different regimes. Indeed, as we just mentioned, for negative β there is only one relative minimum of the potential in each fundamental domain (corresponding to a square lattice). For positive values of β a second minimum appears, corresponding to hexagonal lattices.

4.3.1 The elastic regime

Before proceeding to the analysis of the plastification mechanisms we present in Fig. 4.2 on page 95 the first relevant information that can be extrapolated from the numerical simulations, i.e. that concerning the extent of the elastic regime. In particular:

1. Few observations can be made with regards to the behavior of $\gamma_{first\,aval}(\beta)$, which describes the dependence on β of the strain value ratifying the elastic response limit:

- As β diminishes becoming more and more negative, the first plastification event appears at smaller values of the imposed strain. On the other hand, the magnitude of the corresponding stress fall decreases (Fig. 4.2 on page 95 (c)).
- The combination of these two events could be explained in light of the morphological deformations induced on the energetic landscape, which are extensively presented in section (2.3) of the second chapter. As β decreases in the range of negative values the basins of the square points increase (see Fig. 4.3 on page 96), i.e. the convexity boundaries around the square points broaden; simultaneously we witness the generation of a favorable passageway among the skinny rhombic points above ρ, which constitutes the optimal barrier-crossing path to reach the well in $i+1$. This passage, which lies on the geodetic that connects ρ to $i\infty$, precisely arranges more and more in the neighbourhood of the intersection with the horizontal straight line which parametrizes the simple shear $i \mapsto i+1$ as β diminishes.
- As a consequence, as soon as the first few sample cells deform with strains which fall outside of the convexity region of the strain potential, they encounter a fast-track to immediately reach the basin in $i+1$ provoking the first avalanche to happen. However, the basin around i being more and more wide, the number of scouting cells that actually manage to cross the convex boundaries diminishes as the majority of cells are stifled around i. This explains why the magnitude of the first stress fall decreases together with β in the negative range of this parameter.
- The term "cells" does not want to be deceptive. In fact the physical cells of the body evidently do not explore the energetic basins but rather each of them is associated to a strain in turn related to a point in the Poincaré half-plane $\mathcal{H}$ through (1.21): these are the entities that can be said to explore the basins associated to the square points.

2. The behavior of both these quantities, $\gamma_{first\,aval}(\beta)$ and the magnitude of the first stress fall with respect to β, in the positive range of the values taken by β is more intuitive and it could be explained in light of Fig. 2.11 on page 40 that we report for the ease of the reader also on the lower panel of Fig. 4.2 on page 95:

   - When $\beta > 0$ the distorsive component of the energy (4.46) has two minima in the fundamental domain $\mathcal{D}$, one corresponding to i and the other to ρ. When β increases in the positive range, the basin around ρ and those around the infinitely many equivalent hexagonal points enlarge: as soon as the system becomes unstable by approaching the convexity boundaries around i, which are gradually restricting (see Fig. 4.3 on page 96), it falls into the basin of ρ and the first large plastification event takes place.
   - On the other hand the energy barrier decreases, which explains the behavior of the stress fall associated to the end of the elastic response.

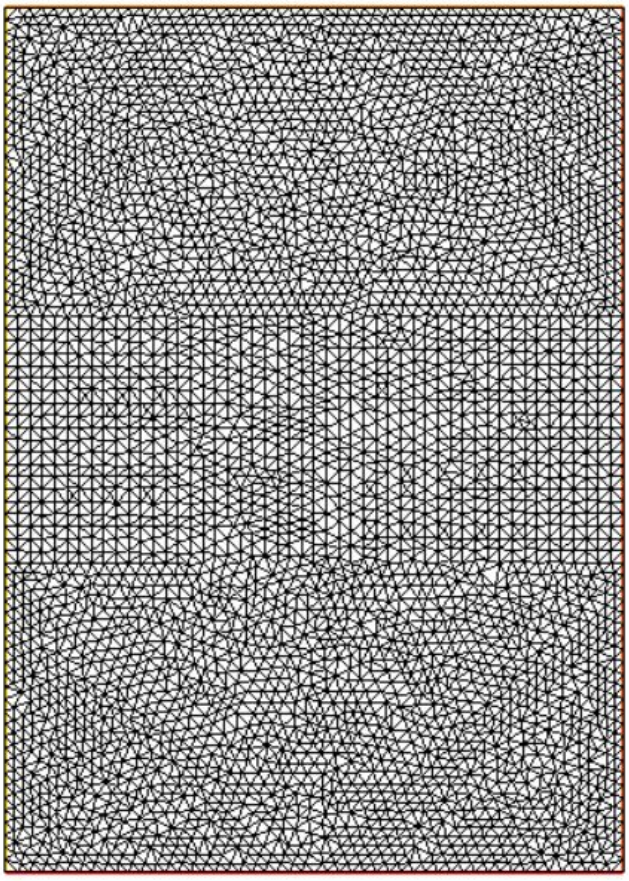

Figure 4.1: Triangulation $\mathcal{T}_h$ of Ω

Furthermore, coherently with the energy barrier behavior this quantity starts increasing when $\beta \geq 1$. It should be noticed that when $\beta \geq 1.2$ it apparently starts decreasing again. However, Fig. 4.16 (b) will show that this trend can be explained in light of the fact that the first avalanche occurs with two subsequent steps due to the inevitable discontinuity of the loading; the sum of the stress fall of these two steps gives a total stress fall indulging the expected trend.

3. The maxima of both $\gamma_{first\,aval}(\beta)$ and the first stress fall are registered at $\beta = 0$ (or in its strict neighbourhood). This is the case of a single minimizer in the fundamental domain $\mathcal{D}$ corresponding to i as it is when $\beta < 0$. However ρ is not a maximum of the energy as it is when $\beta < 0$ but a third order degenerate critical point, i.e. a monkey-saddle. The discussion around this case is posponed to the next section.

4. Panel (b) of Fig. 4.2 on the next page represents the value of the yield strength depending on β, which can be related directly to the behavior of the energy barrier in panel (d).

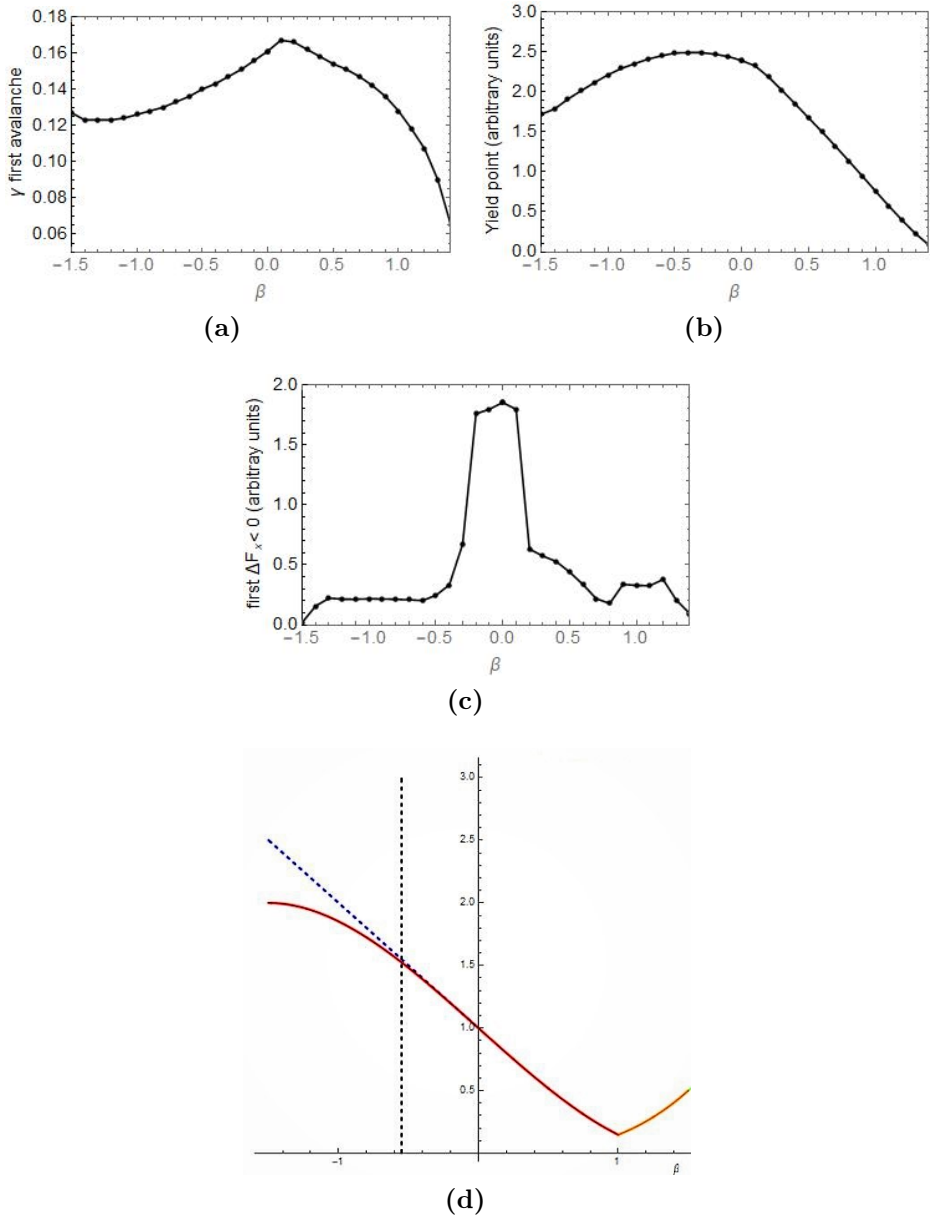

Figure 4.2: (a) Value of the strain parameter γ ratifying the end of the elastic regime depending on β, i.e $\gamma_{first\,aval}(\beta)$. (b) Value of the stress F_x ratifying the end of the elastic regime depending on β. (c) Value of the stress fall $|\Delta F_x|$ at the yield point depending on β. (d) Energy barrier for (4.46) of the simple shear $i \mapsto i+1$ for each value of β

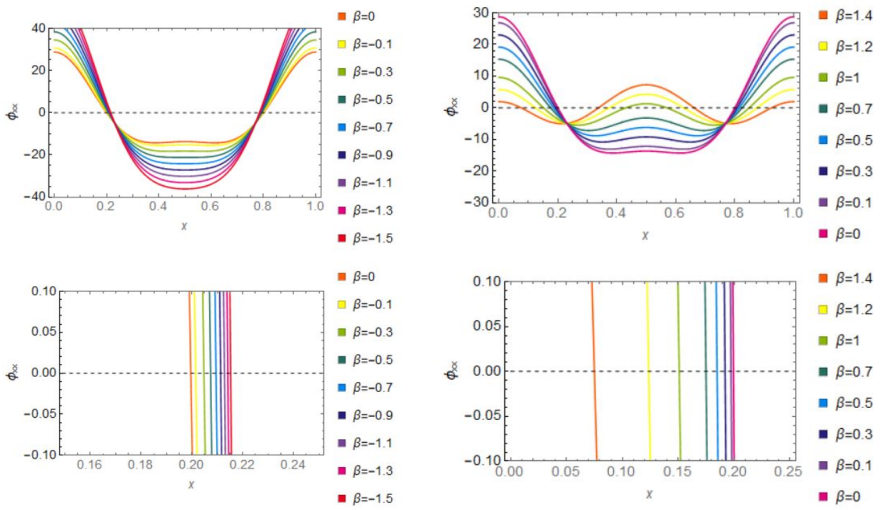

Figure 4.3: Enlargement of the convexity boundaries of (4.46) depending on β. We report the behavior of the second derivative with respect to the horizontal component restricted on the straight line parametrizing the simple shear $i \mapsto i + 1$ (i.e. $\{x = t; y = 1\}, t \in [0, 1]$). The bottom side images show a zoom of the points where it first vanishes, which indicate the end of the convexity area around $z = i$. As β decreases in the negative range the convexity boundaries amplify as the square point is a deeper and deeper dip, while as β increases in the positive range they restrict as the dip around the square point is gradually flattening.

4.3.2 Elasto-plastic tranformation: Single minimizer in the fundamental domain $\mathcal{D}$

This subsection is devoted to the analysis of the plastification mechanisms emerging from the numerical simulations in the case $\beta \leq 0$. First we observe how certain quantities informing about this phenomenon change according to β, then we present more extensively the results concerning the simulation corresponding to $\beta = -0.5$ (the results of this simulation are presented in the Video V1 in the Supplementary Material) and those concerning the case $\beta = 0$ (see Video V5 in the Supplementary Material).
Fig. 4.4 on the following page presents the stress-strain relation during loading at every (negative) β while Fig. 4.5 on page 99 shows the number of cells in each energetic basin during loading at every (negative) β.
Fig. 4.5 on page 99 suggests that the plastification mechanism is in general more complex than expected due to the way global symmetry acts on the energetic landscape. Indeed the basins interested in the process are not only the one associated to the reference configuration $z_0 = i$ and the one imposed by the boundary conditions $z = i + 1$ but also a third basin, the one around $z = \zeta$. On the other hand this is the symmetry-equivalent square energy-basin closest to i in the direction of the boundary condition besides $i + 1$.
However the basin around ζ is more or less involved according to the value of β:

- When β is strictly smaller than 0, say $\beta < -0.1$, very few cells are attracted in this basin as the first plastification event occurs. Indeed being ρ a maximum the energetically optimal barrier-crossing path involves traveling through the corridor corresponding to the skinny rhombic saddle above ρ which allows to directly reach $i + 1$. On the other hand this Figure also confirms that when β is strictly negative the majority of cells tends to remain in the basin around $z = i$ during the loading; in order to observe an actual migration to the boundary-conditions imposed basin around $i + 1$, γ should be higher.

- When $\beta = 0$ the corridor corresponding to the skinny rhombic saddle above ρ disappears by merging into the third order degenerate critical point at ρ, which is a monkey-saddle. Cells, or more properly strains, need to go through this point while reaching the basin in $i + 1$. The presence of the bifurcation mountain pass at $z = \rho$ implies that at the first strain avalanche the second primary shear path $i \to \zeta$ (the first is $i \mapsto i + 1$) is certainly more involved than it was for strictly negative value of β. The symmetry-imposed degenerate saddle points are said to be the lattice disorder engines as their presence immediately activates alternative shear paths.

- A similar picture to the one produced when $\beta = 0$ also concerns $\beta = -0.1$: in this case ρ is not an actual monkey-saddle but still a mightily moderate maximum encircled by three skinny rhombic saddles, hence a monkey-area. More properly, we could speak about monkey-area untill $\beta \simeq -0.55$ as it is explained in the description of Fig. 2.11 on page 40. Indeed at this value the corridor corresponding to the skinny rhombic saddle above ρ precisely lies in the intersection with the straight line parametrizing the deformation

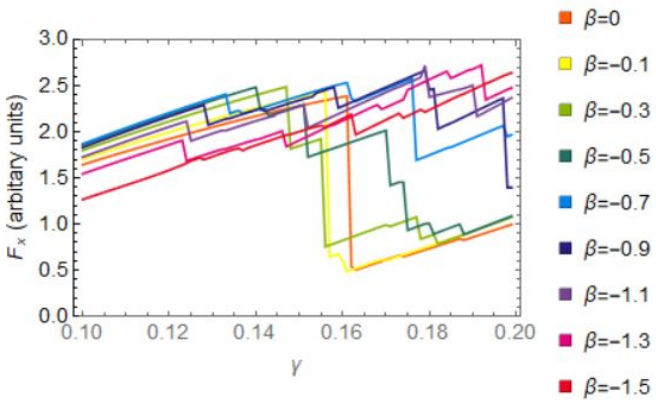

Figure 4.4: The relation stress-strain for $\beta \leq 0$

$i \mapsto i+1$, hence this saddle together with the other two equivalent skinny rhombic saddles around ρ are sufficiently far to consider the central point ρ as a maximum and no more a deformed monkey-saddle. As a consequence the alternative shear path $i \to \zeta$ is involved also at $\beta = -0.3$ and $\beta = -0.5$, even though after the first plastification event has occurred.

A deepened analysis of the case $\beta = -0.5$: hysteresis loop

Loading Figure 4.6 on page 101, Figure 4.7 on page 102 and Figure 4.8 on page 103 show three frames of the Video V1 in the Supplementary Material: they represent three moments of the deformation of the rectangular body imposed by a quasi-static loading along the primary-direction $i \mapsto i+1$ in the case $\beta = -0.5$. In the first frame $\gamma \simeq \gamma_{first\,aval}(-0.5) = 0.14$, in the second frame $\gamma \simeq 0.152$ and in the third frame $\gamma \simeq 0.174$. The three figures describe three moments of the plastic-flow initiation after the initally defect-free lattice has gone through the elastic load-up, which precisely ends at $\gamma \simeq \gamma_{first\,aval}(-0.5)$.
In particular:

1. Figure 4.6 on page 101 displays the information concerning the strain condition right after the first large platification event. We can make the following observations:

   - From the distribution of $\bar{\mathbf{C}}$ on the Poincaré half-plane $\mathcal{H}$ in (b), which appears like a cloud-like set of points, we can observe that the basin around i stifles the majority of cells while few scouting cells lie in the basin of $i+1$.
   - The corresponding deformation field of the body shown in (a) precisely reproduces this condition as we can observe a subdivision into two differently coloured regions, which can be interpreted by looking at the color coding in (c). Both regions appear as deformed but only the blue region corresponds to the plastic slip as it is deformed in the direction of the highest shear corresponding to $\gamma = 1$; indeed this slip band contains

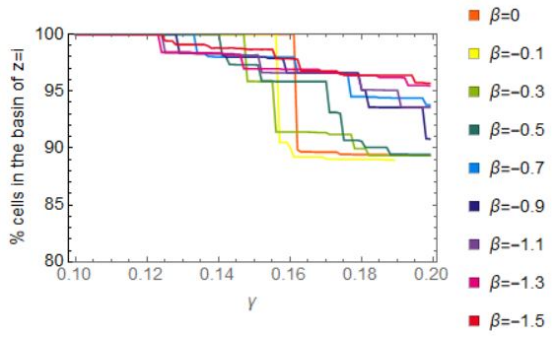

(a)

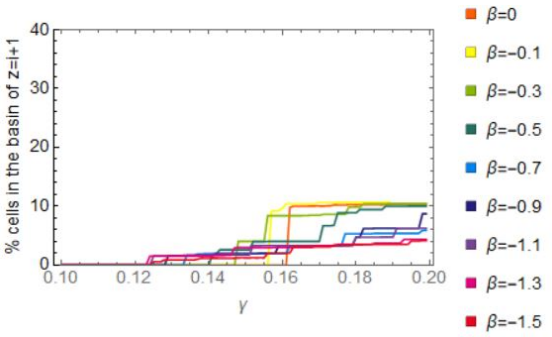

(b)

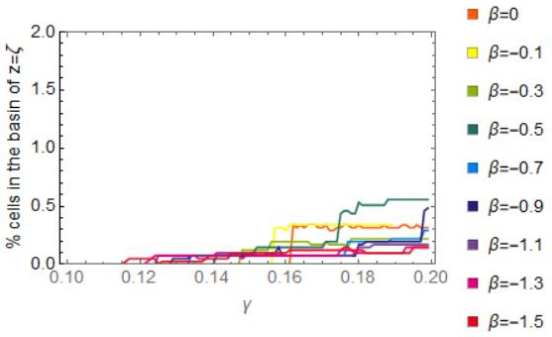

(c)

Figure 4.5: Percentage of cells in each basin during the loading at different values of $\beta \leq 0$

the physical cells associated to strains that jumped to the basin around the minimizer $i+1$ right after the end of the elastic regime. A few green cells represent the set of points in the strain-cloud which travelled through the other primary shear path $i \to \zeta$.

2. The first plastification event triggers a sequence of intermittent avalanches shown in the panel (e) of every frame: the orange spikes quantify the discontinuity of the strain activity, as the strain cloud splinters. The other two mentioned figures capture two moments of this bursting plastic flow. In particular:

   - Figure 4.7 on page 102 and Figure 4.8 on page 103 show how the slip band thickens as more and more cells reach the basin around $i+1$ during this phase. Simultaneously the distribution of local angles coherently fragments from the inital unique block as the bottom side of the body deforms in the direction of the imposed shear. The two Figures depict the strain condition right after the second and third large slip events, which produce a stress relaxation observable in the panel (e) of each Figures.
   - The slipped portion of the crystal is not completely homogeneus as it contains few green cells that represent the strains entagled in the basin around ζ. The presence of a number of strains in this latter basin can be explained in light of the fact that when $\beta = -0.5$ the region around the hexagonal point is a monkey area, which activates the second primary shear path $i \to \zeta$ as we explained previously.

Unloading The analysis of the case $\beta = -0.5$ comprehends also Figures 4.9 on page 105 and 4.10 on page 106. These Figures represent the results obtained from the resolution of the problem (4.18) under the hypotheses listed in section (4.3). However we want now to simulate a decreasing shear stress condition by gradually diminishing γ. As the end of the elastic regime for $\beta = -0.5$ is at $\gamma \simeq \gamma_{first\,aval}(-0.5) = 0.14$ we choose a slightly higher value of γ as a starting point and decrease it of a percentage point untill $\gamma = 0$ and Dirichlet boundary conditions vanish. The objective is to observe the residual body deformation due to the irreversibility characterizing the plastic domain.
Fig. 4.9 on page 105 represents a frame of the Video V2 in the Supplementary material at $\gamma \simeq 0.075$ while Fig. 4.10 on page 106 represents the frame at $\gamma = 0$. We want to remark that:

1. By observing the panel (e) of each frame we can deduce that the basin-hopping activity of the strains is almost null; during the reverse process strains are almost paralyzed in the initial basins hence the material does not recover the reference configuration and at $\gamma = 0$ we can register a residual stress.

2. The reference configuration has now been contaminated as the body contains a non-homogeneus material in which the underlying lattice corresponds to two different variants of the square lattice. Such a body shape portrays a real

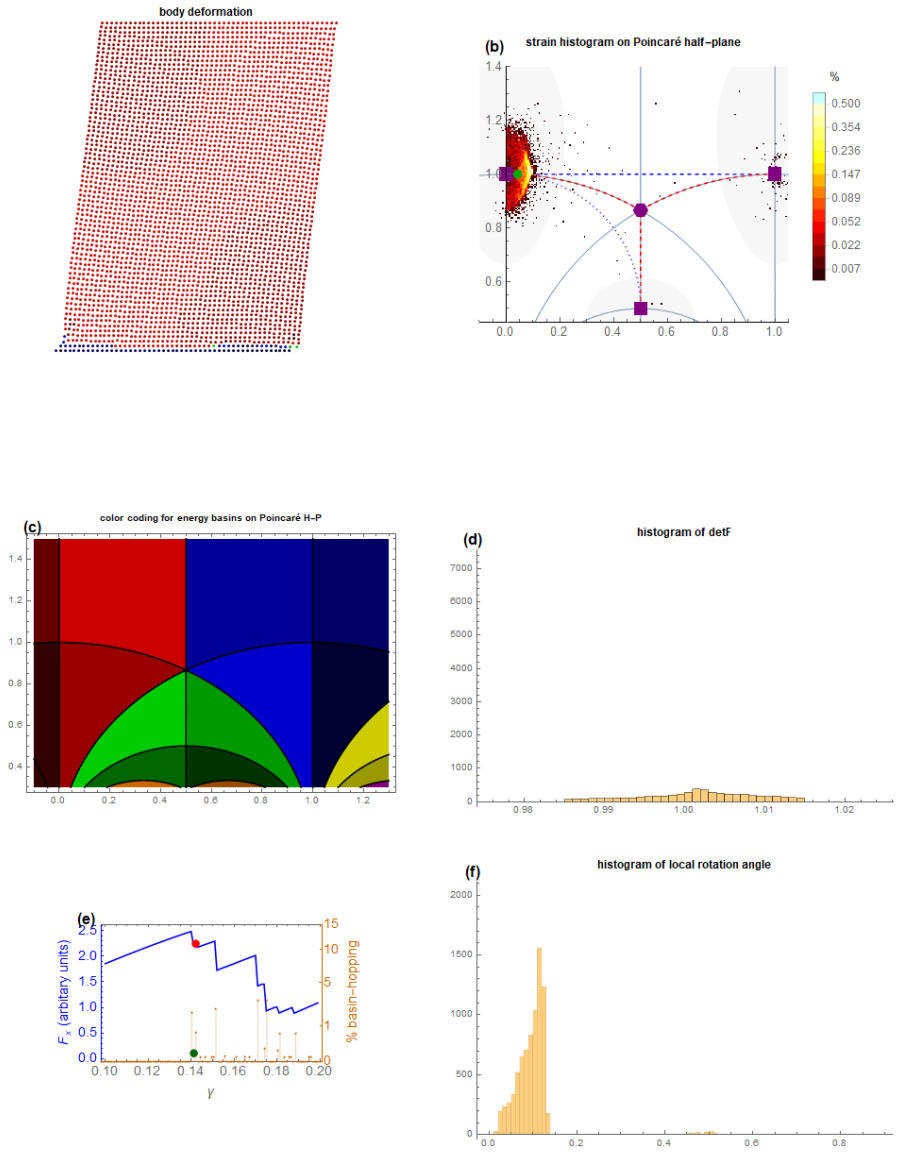

Figure 4.6: Results of the numerical simulation of plastic flow initiation of a square crystal with energy (4.46) when $\beta = -0.5$ and γ increasing from 0.1 to 0.2: frame corresponding to $\gamma \simeq 0.14$. In each frame there are six panels: (a) shows the body deformation evolution; colors are coherent to panel (c), highlighting to which basin it belongs the strain associated to every physical cell. (b) shows the evolution of the distribution of strains on the Poincaré half-plane as γ increases, represented by a moving cloud-like set of points. This can be obtained as the histogram of the density of $\bar{\mathbf{C}}$ on $\mathcal{H}$. Gray palls represent the convexity domains in $\mathcal{H}$. The straight dashed blue line parametrizes the increasing shear γ from i to $i+1$: this corresponds also to the optimal barrier-crossing path, which involves travelling through the corridor formed by the skinny rhombic saddle above the hexagon. Dashed red curve indicates the path from i to $i+1$ that involves passing through the hexagonal maximum instead. Panel (e) displays the stress-strain with a blue curve while the orange spikes on the bottom side of the graph describe the percentage of strains jumping from one energy basin to another at every value of γ. Panel (d) shows the distribution of the values assumed by the determinant of the deformation gradient $\mathbf{F}$ in every cell of the body. Panel (f) analogously reports the distribution of the local rotation angles, which can be obtained from the rotation matrix associated to $\mathbf{F}$ in every cell.

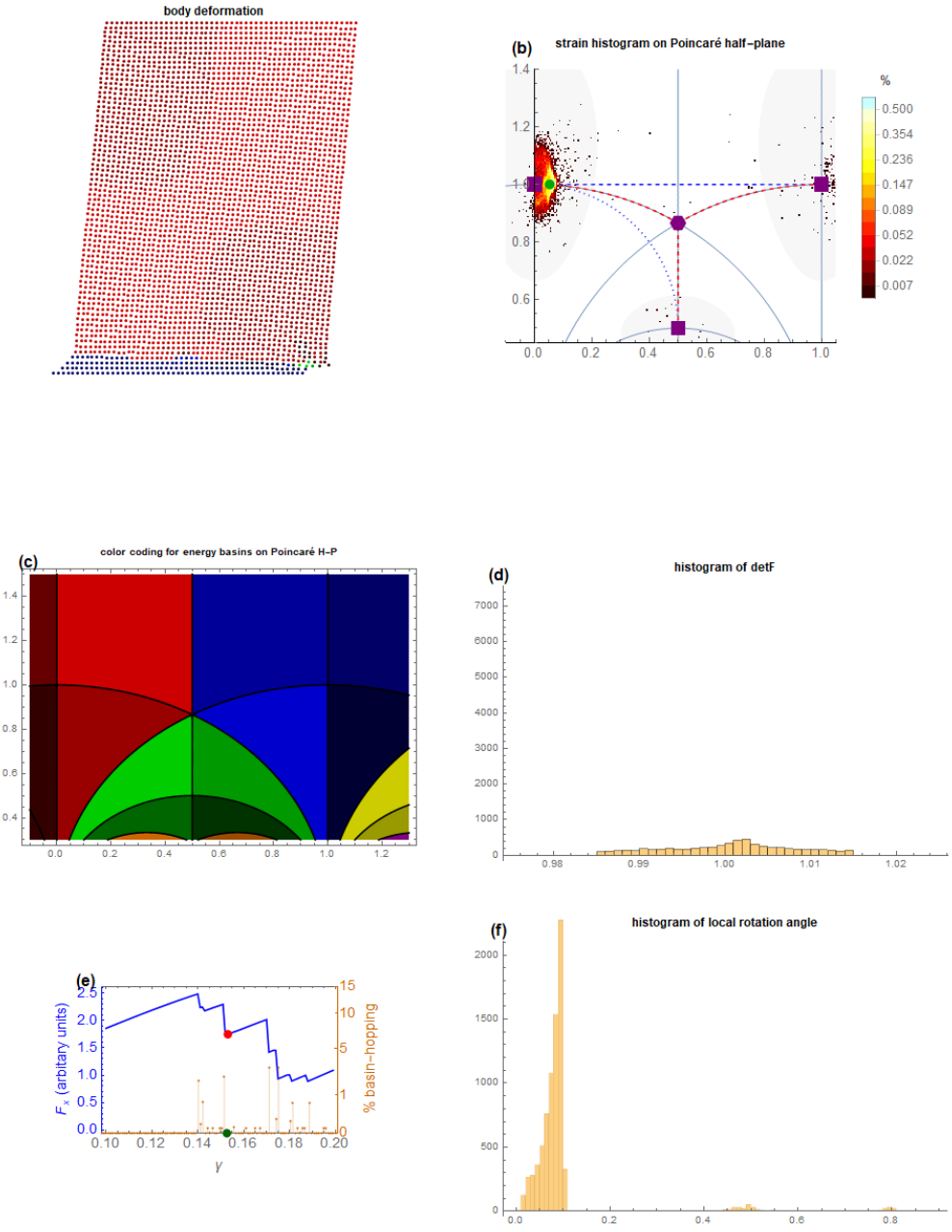

Figure 4.7: Results of the numerical simulation of plastic flow initiation of a square crystal with energy (4.46) when $\beta = -0.5$ and γ increasing from 0.1 to 0.2: frame corresponding to $\gamma \simeq 0.152$

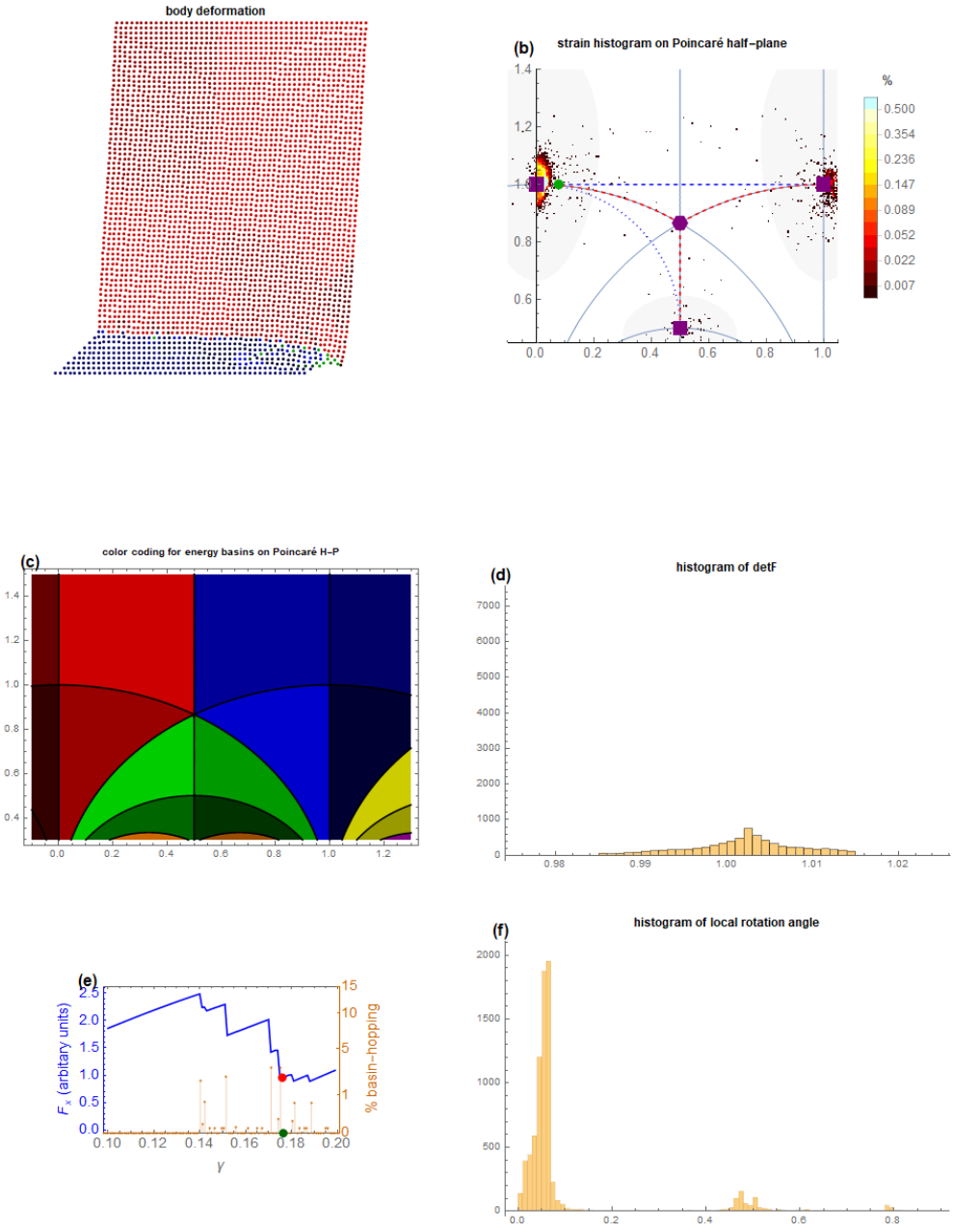

Figure 4.8: Results of the numerical simulation of plastic flow initiation of a square crystal with energy (4.46) when $\beta = -0.5$ and γ increasing from 0.1 to 0.2: frame corresponding to $\gamma \simeq 0.174$

crystalline material more faithfully than the purest crystalline body that was considered as initial configuration for the outward voyage.

3. The combination of the stress-strain relation of the outward and backward voyage returns a part of the shear hysteresis loop of the material (see Fig. 4.11): the cycle is incomplete as the loading directly started at $\gamma = 0.1$ and the material should be further stimulated in the range of negative γ to reabsorb the splip band; this would reproduce a loading along the opposite primary-shear direction towards the basin around $i - 1$.

A deepened analysis of the case $\beta = 0$: a full hysteresis loop
A complete shear hysteresis loop has been obtained instead in the case $\beta = 0$ (see Fig. 4.11 on page 107). This comprehends a first loading phase along the primary-shear path $i \to i + 1$, which is obtained by gradually increasing γ from 0.1 to 0.2. Then we proceeded to unload the material decreasing γ from 0.18 to -0.10; in the range of negative γ, the primary shear direction is reversed as it heads towards the well in $i - 1$. Finally a new loading phase from $\gamma = -0.10$ to $\gamma = 0.18$ concluded the cycle. The evolution of the deformation with all its relevant characteristics is represented in Video V5 (first loading), V6 (unloading) and V7 (final loading) of the Supplementary Material.
As previously mentioned, this case is relevant because when $\beta = 0$ the strain energy function (4.46) degenerates into the purely "square" energy (1.56); since the term acting on the behavior of the function in the vicinity of ρ has vanished, global symmetry freely shapes the local energy topography around this point, which turns into a third-order degenerate critical point i.e. a monkey saddle. As the count of the number of cells in each basin demonstrates (see Fig. 4.5 on page 99), the basin around ζ is involved earlier than it was in the previous considered case because the degenerate saddle point ρ behaves like a source of lattice disorder by activating the alternative shear path $i \to \zeta$ as soon as the first plastification event occurs (in the case $\beta = -0.5$, very few cells explored the basin around ζ at the first "avalanche"). We decided to perform a full hysteresis loop in this case precisely because we expect that the material after the first loading will be considerably flawed due to the disorder mechanism just explained. Thus we would like to investigate if these defects are preserved during the unloading phase and whether the second loading phase differs from the first one by eventually starting from a defective reference configuration.

Loading Fig. 4.12 on page 108 reports a frame of the first loading phase (Video V5) which corresponds to $\gamma \simeq 0.18$, i.e. the strain condition from which the unloading phase starts. Two main observations can be done about this phase:

1. Since an extremely marked stress relaxation has already ratified the end of the elastic regime, we can observe the consecutive abrupt subdivision of the body (panel (a) of Fig. 4.12 on page 108) into two distinguished regions as it happened in the case $\beta = -0.5$.

2. Panel (b) of the same figure witnesses how some strains have also occupied the dip in ζ as it was expected due to the presence of a monkey-saddle in ρ.

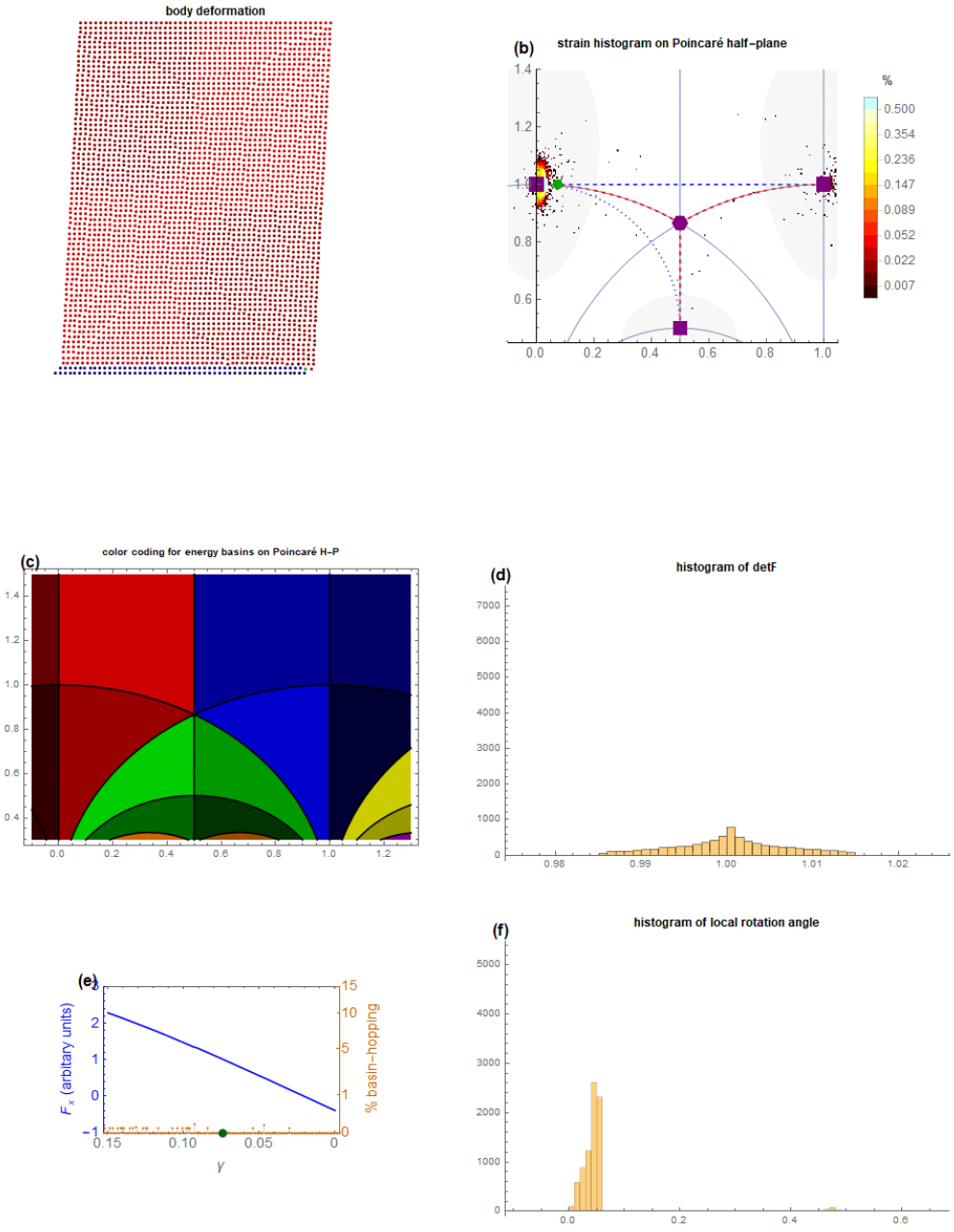

Figure 4.9: Results of the numerical simulation of plastic flow initiation of a square crystal with energy (4.46) when $\beta = -0.5$ and γ decreasing from 0.15 to 0: frame corresponding to $\gamma \simeq 0.075$

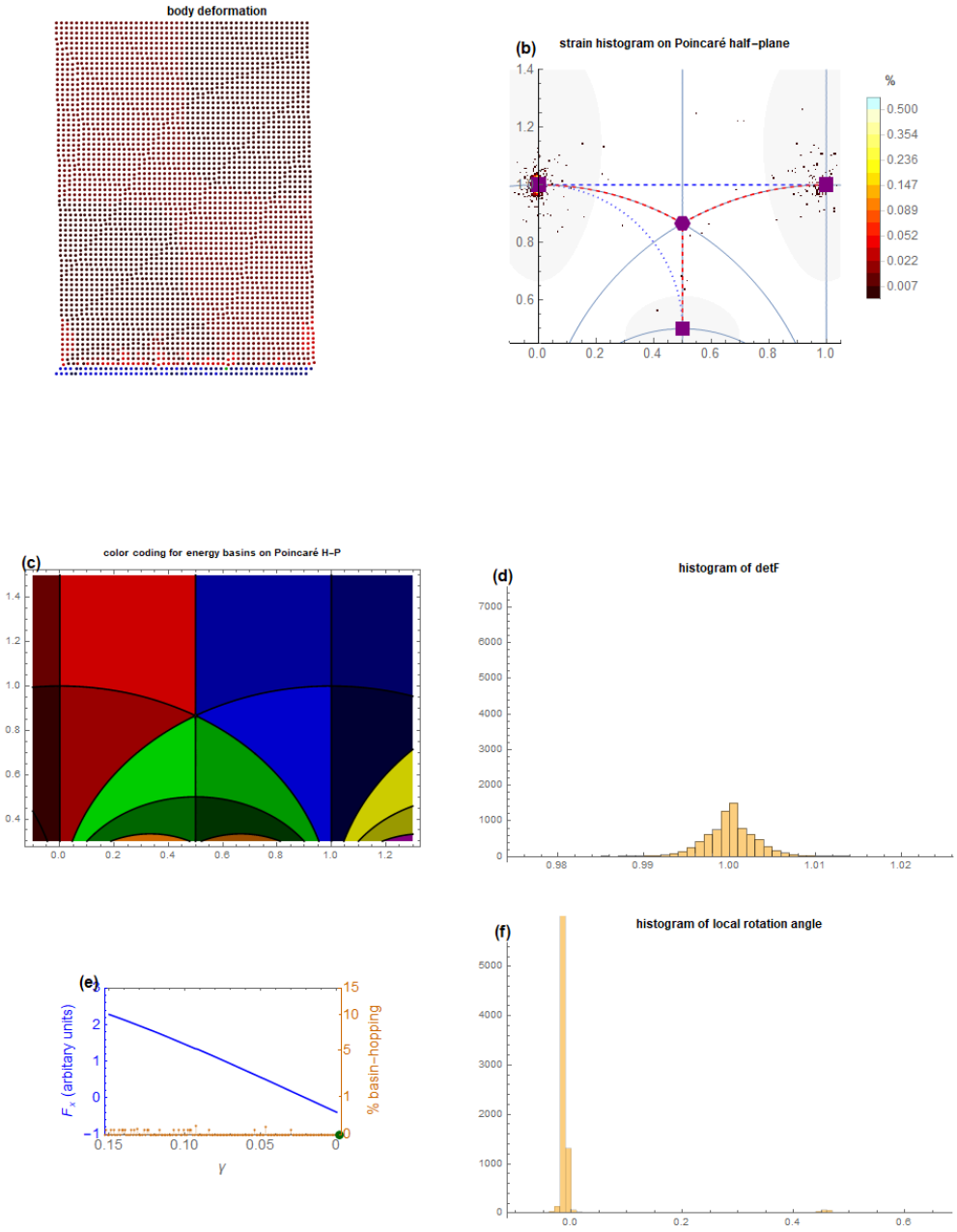

Figure 4.10: Results of the numerical simulation of plastic flow initiation of a square crystal with energy (4.46) when $\beta = -0.5$ and γ decreasing from 0.15 to 0: frame corresponding to $\gamma = 0$

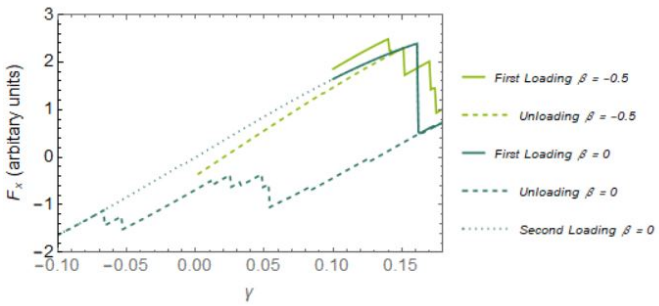

Figure 4.11: (Uncomplete) shear hysteresis for the case $\beta = -0.5$ and complete shear hysteresis for the case $\beta = 0$

Unloading From this point, the unloading phase starts as γ slowly decreases. The unloading phase is characterized by more, yet smaller, avalanches than the loading phase (represented by jumps in the stress-strain curve). In particular:

1. By observing Fig. 4.13 on page 109 we can appreciate that, as it happened in the case $\beta = -0.5$, the complete release of load, which coincides with $\gamma = 0$, does not allow to recover the strain; this implies that at $\gamma = 0$ there is still a residual stress as Fig 4.11 shows, which coherently represent the irreversible character of plastic deformations.

2. Then, γ is gradually decreased untill -0.10, which implies loading towards the opposite direction than the one considered in the first loading. Fig. 4.14 on page 110 shows that the slip band disappears as strains jump back to the basin around i. However few cells are stiffled in the basin around ζ. It should be noticed that the system is cleansed of the slip band as soon as the stress-strain curve of the unloading phase meets the straight line representing the elastic load up of the first loading phase (see Fig. 4.11). This happens at $\gamma \simeq -0.05$ (see Video V6 in the Supplementary Material) hence before γ reaches -0.10. Thus we can infer that the strain has been excessive because the system has lost its plastic deformation and we expect that the reloading phase will retrace the first loading phase.

Reloading As soon as γ starts increasing again (Video V7) untill the load is again released at $\gamma = 0$ (see Fig. 4.15 on page 111) the green cells also reach the basin around i (see the orange spikes in Panel (e) of the same Figure) and we recover the original defect-free reference configuration as: this is the reason why as announced we can observe in Fig. 4.11) that the reloading along the primary shear direction $i \to i + 1$ generates a stress-strain curve precisely coinciding with the first loading stress-strain curve. Video V7 also shows that the strain evolution during the reloading phase does not present any differences with respect to the loading phase.

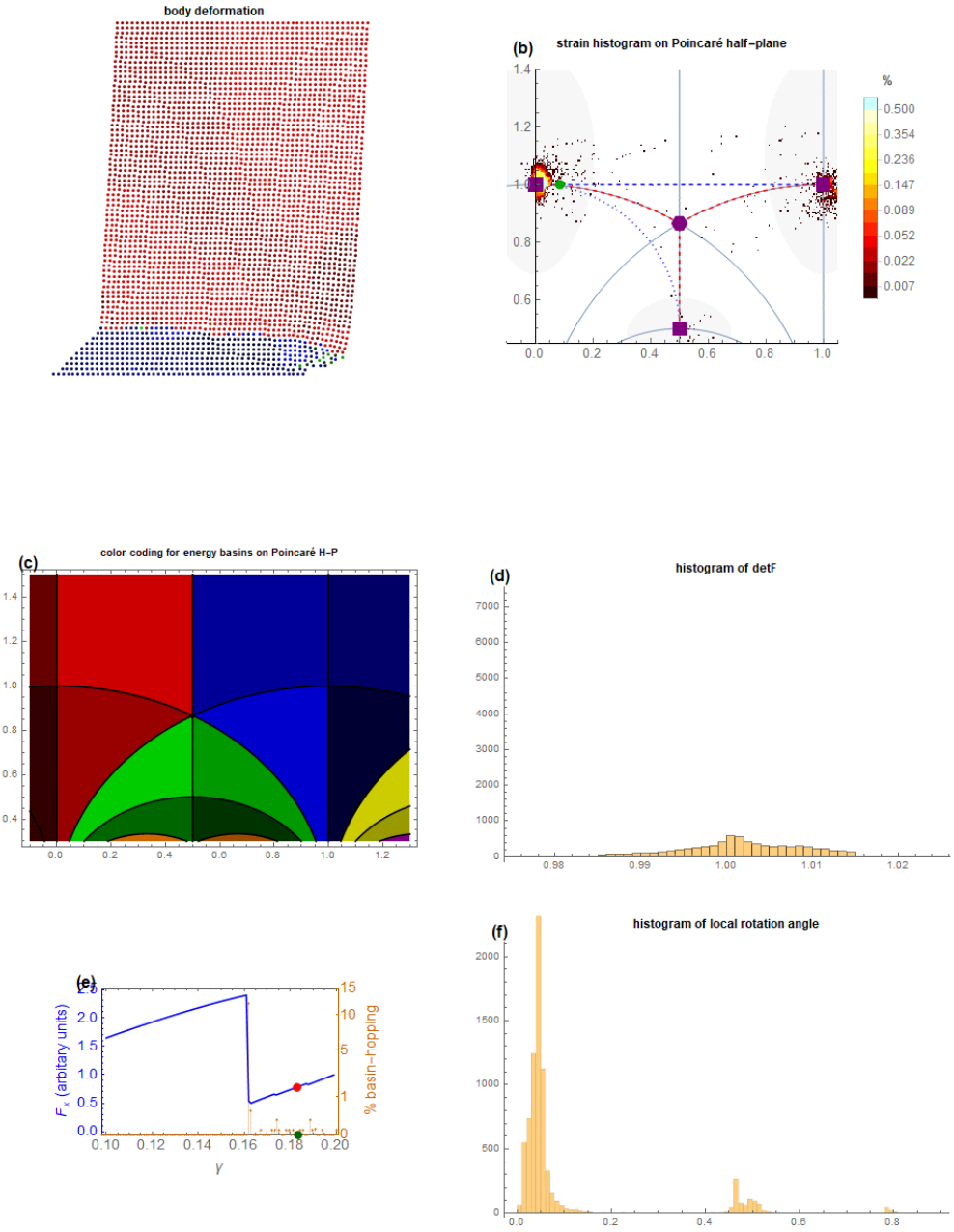

Figure 4.12: Results of the numerical simulation of plastic flow initiation of a square crystal with energy (4.46) when $\beta = 0$ and γ increasing from 0.1 to 0.2 (first loading phase): frame corresponding to $\gamma \simeq 0.18$

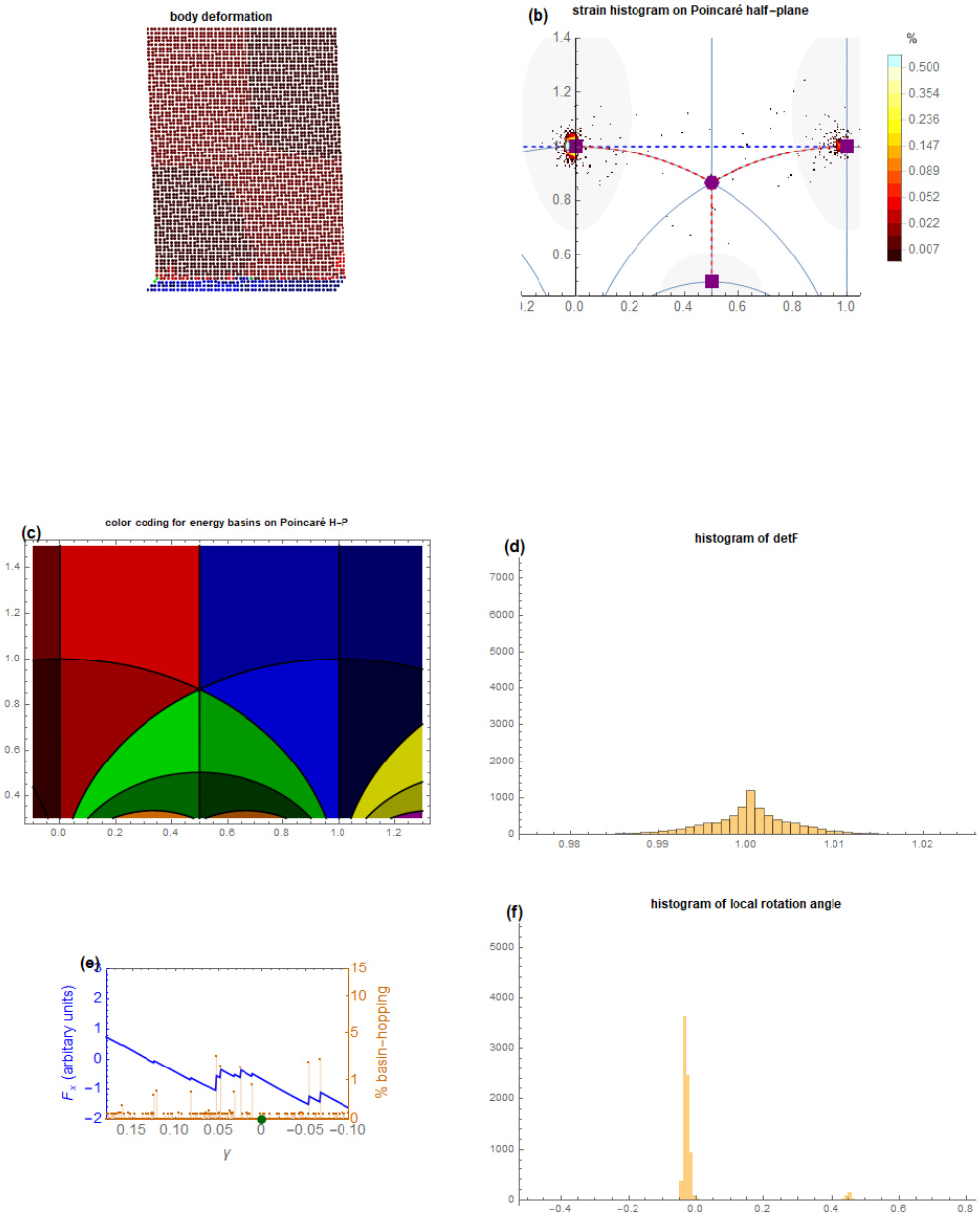

Figure 4.13: Results of the numerical simulation of plastic flow initiation of a square crystal with energy (4.46) when $\beta = 0$ and γ decreasing from 0.18 to -0.10 (unloading phase): frame corresponding to $\gamma \simeq 0$

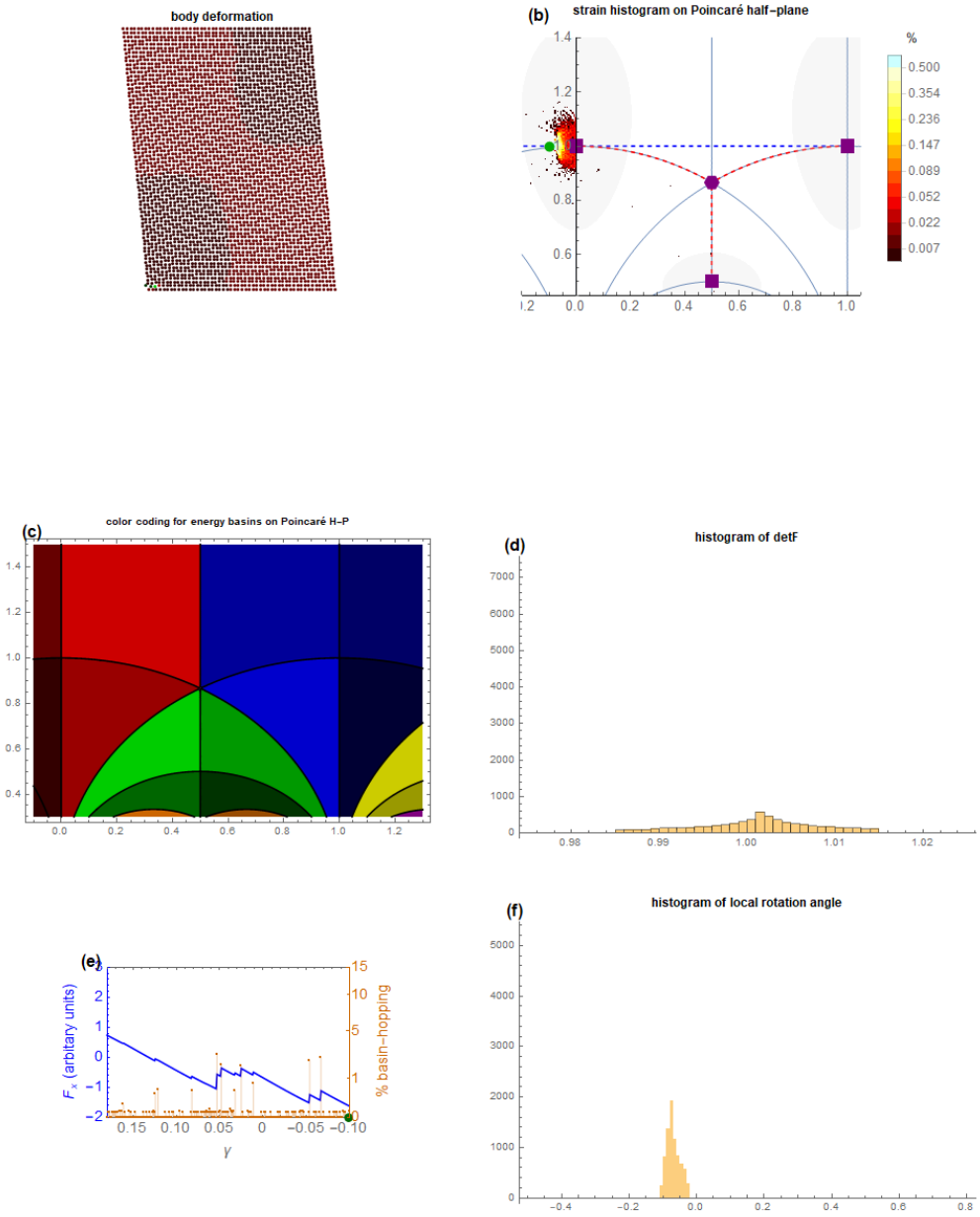

Figure 4.14: Results of the numerical simulation of plastic flow initiation of a square crystal with energy (4.46) when $\beta = 0$ and γ decreasing from 0.18 to -0.10 (unloading phase): frame corresponding to $\gamma = -0.10$

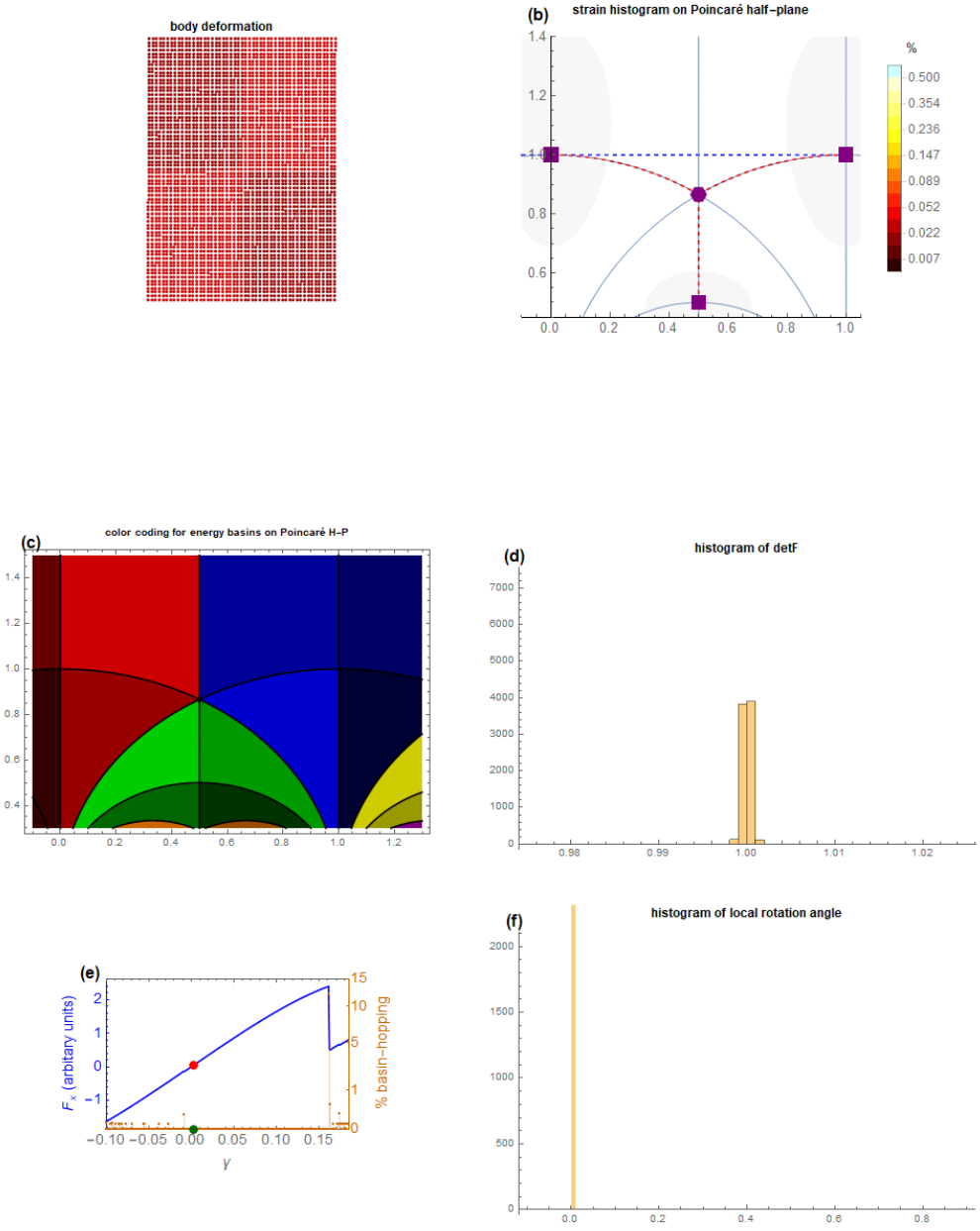

Figure 4.15: Results of the numerical simulation of plastic flow initiation of a square crystal with energy (4.46) when $\beta = 0$ and γ increasing from -0.10 to 0.18 (reloading phase): frame corresponding to $\gamma \simeq 0$

4.3.3 Solid-solid phase transitions: Two minimizers in the fundamental domain $\mathcal{D}$

In this section we repeat for positive β the analysis performed in the last section: first we study the behavior of the most significant quantities characterizing the deformation depending on β, then we explore the details of one particular simulation corresponding to $\beta = 1$, whose Video can be found on the Supplementary Material as V3. It has to be remarked that the computational time taken by the simulations corresponding to $\beta > 0$ is much more higher than the case $\beta \leq 0$. This can be explained in light of the fact that the presence of multiple minimizers of the strain (which is what characterizes the energy landscape when $\beta > 0$) increases the number of solutions for each γ. Hence, the maximum value of γ varies among the simulations but in each of them γ_{max} is chosen in order to at least ensure the subdivision of the body shape into two distinguishable regions, one undeformed and the other deformed in the direction of the complete shear.
The stress-strain relation on Fig. 4.16 on the facing page confirms what was already observed concerning Fig. 4.2 on page 95: the presence of a new basin around the hexagonal point reduces the magnitude of the stress as as the energy possesses two relative minima now (considering the restriction only on the fundamental domain $\mathcal{D}$). This trend was already announced from the plot of the theoretical energy barrier (see (d) in Fig. 4.2 on page 95), which also indicates in accordance with intuition that $\beta = 1$ is a rather significant value. When $\beta = 1$, i and ρ are minima of equal height and as soon as $\beta > 1$ the hexagonal point ρ gains the role of absolute minimum of the energy (4.46). Moreover the energetic landscape does not contemplate any alternative route that helps reaching the basin around $i + 1$, hence the energetically optimal barrier-crossing path dictates the passage through ρ; along the path a number of cells get trapped into this dip, which induces a more colourful plastification mechanism and a more complex defect microstructure with respect to the case $\beta < 0$.
Fig. 4.17 on page 114 suggests that:

- The value $\beta = 1$ unequivocally represents the frontier value as the panel (d) shows that the basin around ρ is lavishly involved only for $\beta \geq 1$.
- When $0 < \beta < 1$ at the first plastification event cells either swarm the basin around $i + 1$ by following the primary shear path $i \mapsto i + 1$ (this is the case of $\beta = 0.1$) or they follow the other primary shear path $i \mapsto \zeta$, but they are certainly not entangles in the dip corresponding to ρ.
- This latter subdivision in the plastification mechanism for $0 < \beta < 1$ could be explained in light of the fact that when $\beta = 0.1$ the convexity area around ρ is still narrow while the convexity boundaries around the square points are rather extended (see Fig. 4.3 on page 96): as soon as the system becomes unstable by approaching the convexity boundaries around i, the first scouting cells (more properly, strains) cross over directly to the well in i because they still do not perceive the dip in ρ.
- On the other hand, when $0.1 < \beta < 1$, strains follow the energetically optimal-barrier path that involves passing through ρ, whose convex boundaries have

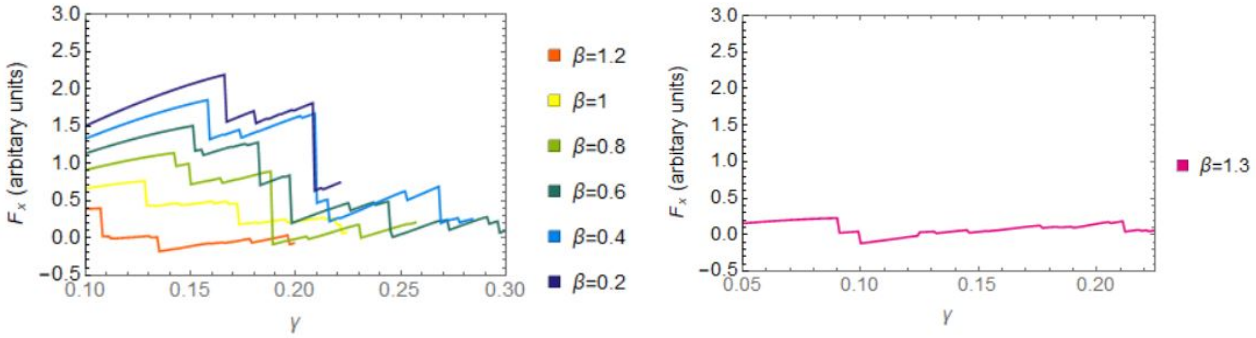

(a) **(b)**

Figure 4.16: The relation stress-strain for $\beta > 0$. Panel (b) represents the stress-strain for $\beta = 1.3$: in this case the end of elastic regime occurs before $\gamma = 0.10$. Panel (a) represents the cases where this event occurs later than $\gamma = 0.10$.

enlarged, but they do not linger and proceed towards the second symmetry-equivalent square energy-basin closest to i, i.e. ζ.

A deepened analysis of the case $\beta = 1$: hysteresis loop

Loading As we proceeded in the case $\beta = -0.5$ we present three significant moments of the deformation of the body through three frames of the Video V3 in the Supplementary Material. In particular:

1. Figure 4.18 on page 117 represent the results of the simulation of the case $\beta = 1$ paralyzed at $\gamma_{first\,aval}(1) \simeq 0.129$, right after the first large plastification event has occured as soon as the elastic load-up ended. We can observe that:

   - A portion of the strain cloud has quitted the reference configuration $z_0 = i$ and it walks along the energetically optimal path which now corresponds to the dashed-red curve in order to reach the equivalently convenient point of rest of the energy in ρ.
   - From panel (e) we infer that 10% of strains has jumped to the basin around ρ, inducing in the body the generation of two parallel bands in the hexagonal phase (panel (a)).

2. As in the previous cases, a large stress-relaxation triggers the initiation of a bursting plastic-flow during which other marked stress relaxations occur like the one represented in Fig. 4.19 on page 118. Here we observe that

   - The body separates into two regions, one almost undistorted (yet containing a non-homogeneus material in which the underlying lattice is both square and hexagonal) and the other deformed in the direction of the imposed boundary condition (the lower right part precisely to the highest shear value corresponding to the minimizer $i + 1$).

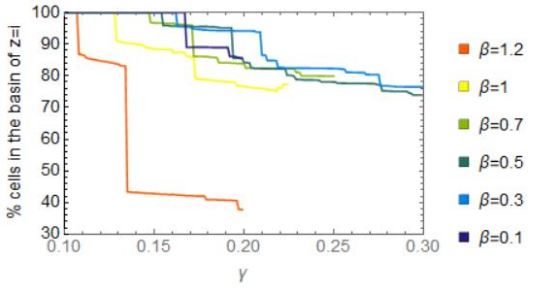

(a)

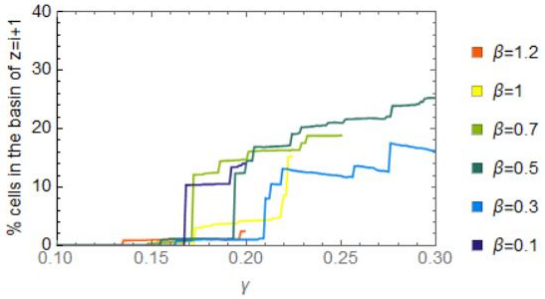

(b)

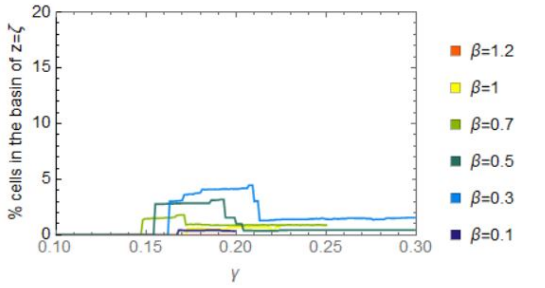

(c)

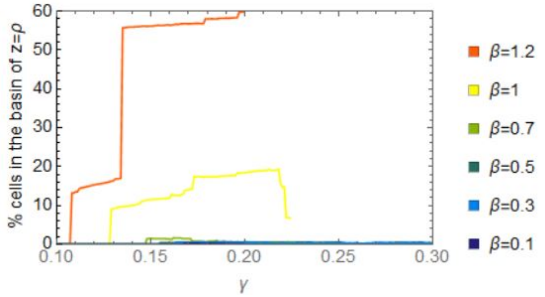

(d)

Figure 4.17: Percentage of cells in each basin during the loading at different values of $\beta > 0$

- Few cells also inevitably explore tha basin around ζ.

3. Finally, Fig. 4.20 on page 119 represents the strain condition right after the third marked stress relaxation:

   - The slip band thickens and prosecutes the distorsion in the direction of the highest shear; however, the underlying material is non-homogeneous as it contains an oblique band in the hexagonal phase.
   - Most interestingly the undeformed region has cleansed of the hexagonal phase as we could already observe from Fig. 4.17 on the facing page: the strains leaving the basin around ρ at this γ do not reach the well in $i+1$ but rather return to the original reference configuration $z_0 = i$, causing the percentage of cells in this well to slightly increase.

Unloading Figures 4.21 on page 120, 4.22 on page 121 and 4.23 on page 122 represent three frames of the Video V4 in the Supplementary Material, hence three moments of the return trip given by a decreasing shear stress condition in the case $\beta = 1$. From the previous paragraph we learnt that the first plastification event occurs at $\gamma \simeq 0.129$ when 10% of strains jumps in the basin around the second minimizer of (4.46), i.e. ρ. Only at the second marked stress relaxation, which takes place at $\gamma \simeq 0.173$, strains start reaching the square energy-basin imposed by the boundary condition, i.e. $i+1$ and in a small percentage the other symmetry-equivalent square basin closest to i, i.e. ζ. Hence the return trip starts right after the second marked avalanche at $\gamma \simeq 0.18$. The observation of the three mentioned figures let us infer that:

1. Through a discontinuous strain activity characterized by a ceaseless basin bouncing of local strains the body eventually re-absorb the deformation cleansing of all defects as Fig. 4.23 on page 122 shows (notice that the residual stress is null). In particular:

   - Fig. 4.22 on page 121 displays that the cleaning process first implies removing the dishomogeneity induced by the presence of the hexagonal phase in both the two main regions of the body (one almost undeformed and the other one distorted in the direction of $i+1$).
   - This behavior does not portrays faithfully the irreversibility of real plastic deformations but it is mainly due to the fact that the initial configuration was chosen to be homogeneus and defect free.

2. A second observation concerns the hysteresis cycle obtained from the stress-strain curve of both the loading and unloading phase (see Fig. 4.24 on page 123). As in the case $\beta = -0.5$ the cycle is uncomplete as the unloading phase directly started from $\gamma = 0.10$, skipping the elastic load-up. The aspect to remark though is that we can identify some ranges of these curves where to an increasing deformation it corresponds an almost constant stress and analogously it happens when recovering the deformation during the unloading. This effect is similar to the one characterizing a superelastic behavior; however,

superelasticity exhibits in the context of weak martensitic phase transformations as it requires reversibility, while this result was obtained minimizing the energy modelling reconstructive martensitic phase transformations (4.46).

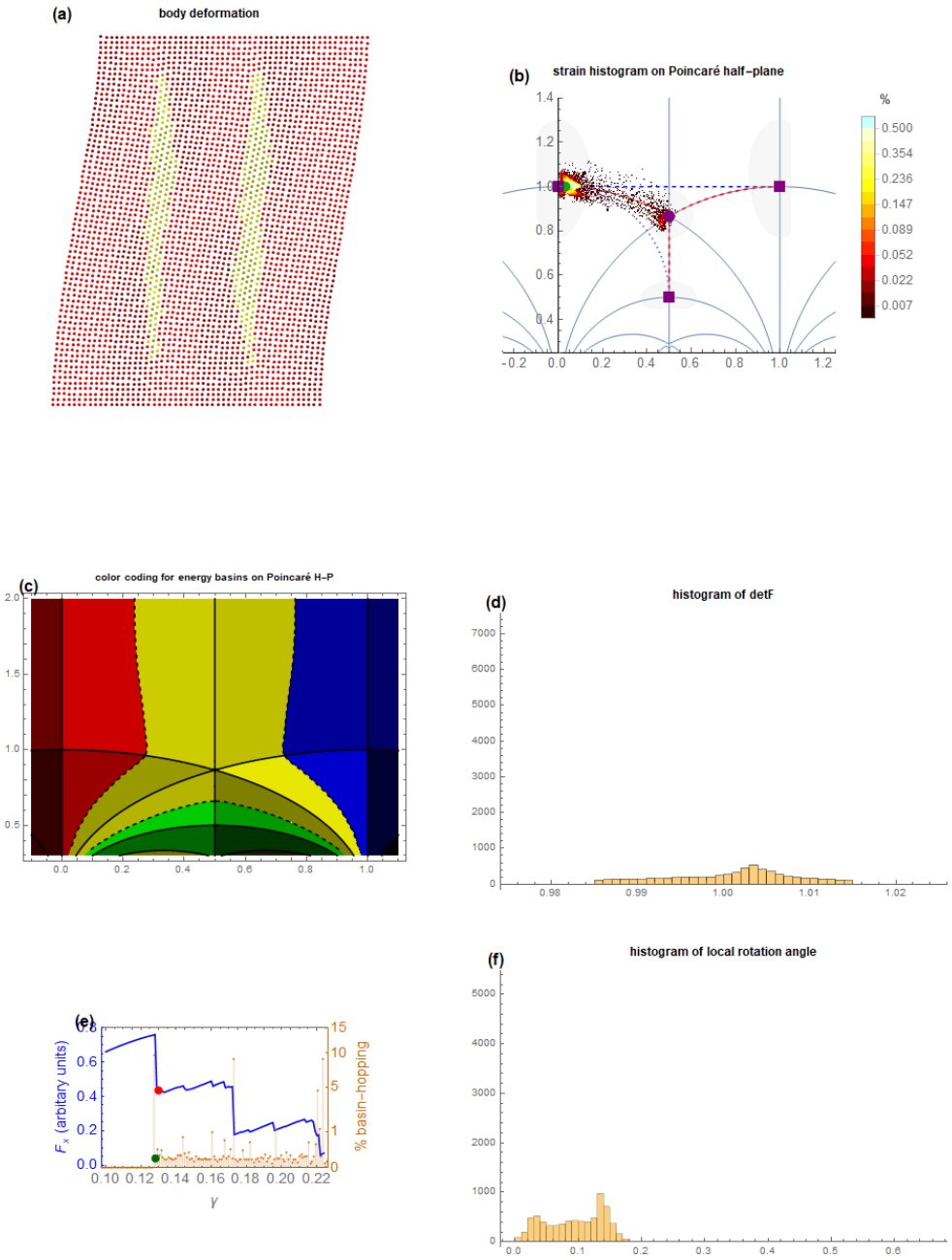

Figure 4.18: Results of the numerical simulation of plastic flow initiation of a square crystal with energy (4.46) when $\beta = 1$ and γ increasing from 0.1 to 0.225: frame corresponding to $\gamma \simeq 0.129$

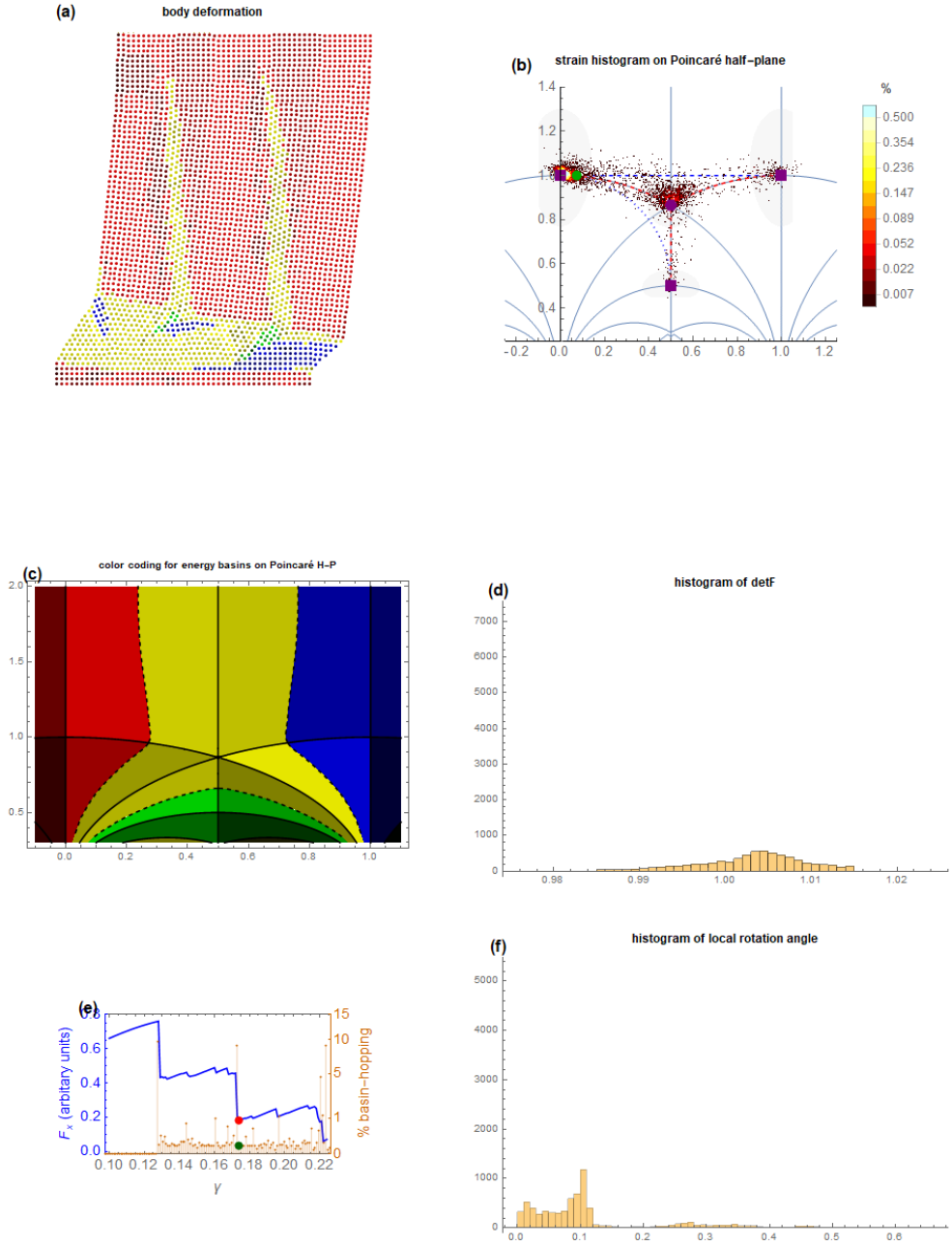

Figure 4.19: Results of the numerical simulation of plastic flow initiation of a square crystal with energy (4.46) when $\beta = 1$ and γ increasing from 0.1 to 0.225: frame corresponding to $\gamma \simeq 0.173$

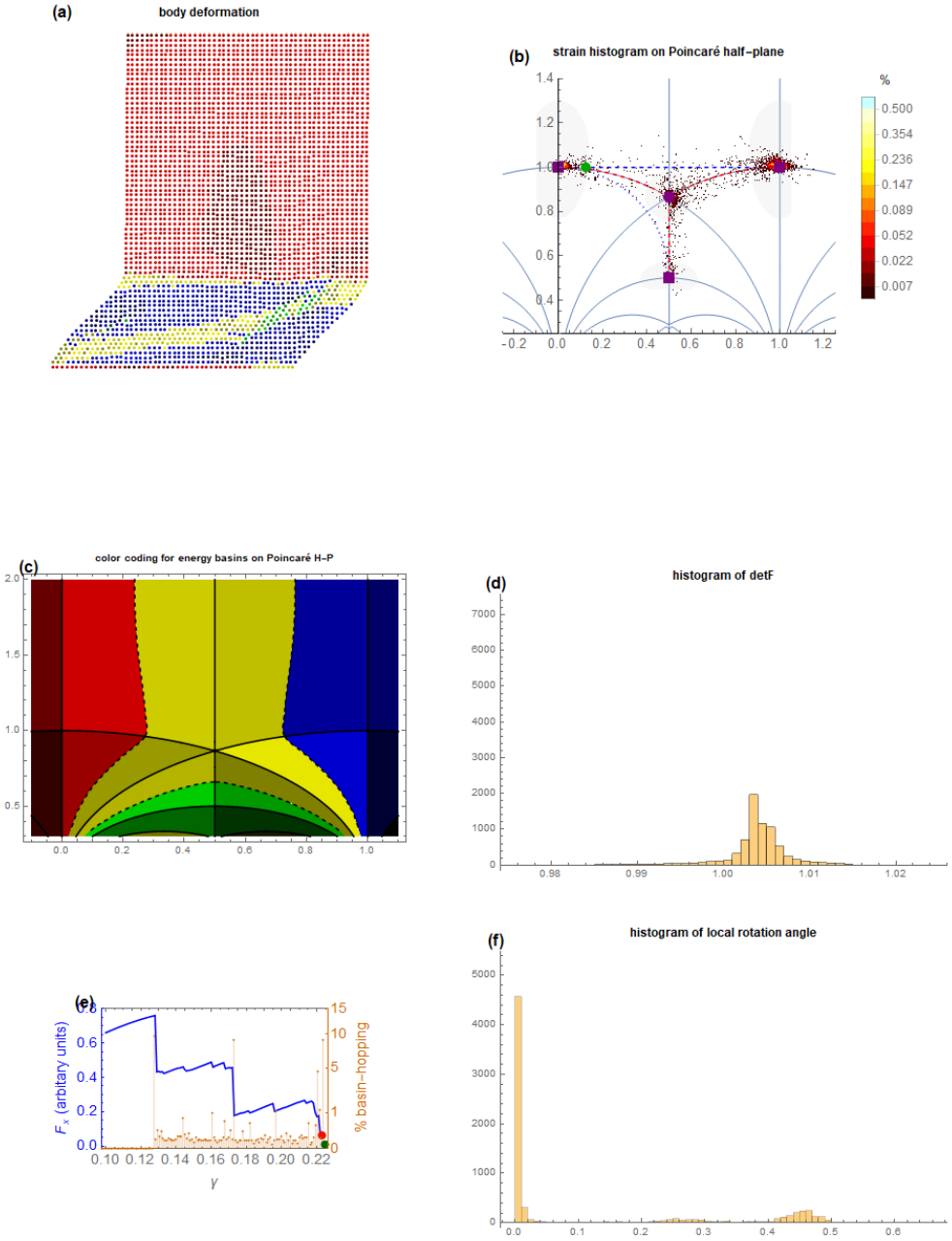

Figure 4.20: Results of the numerical simulation of plastic flow initiation of a square crystal with energy (4.46) when $\beta = 1$ and γ increasing from 0.1 to 0.225: frame corresponding to $\gamma \simeq 0.222$

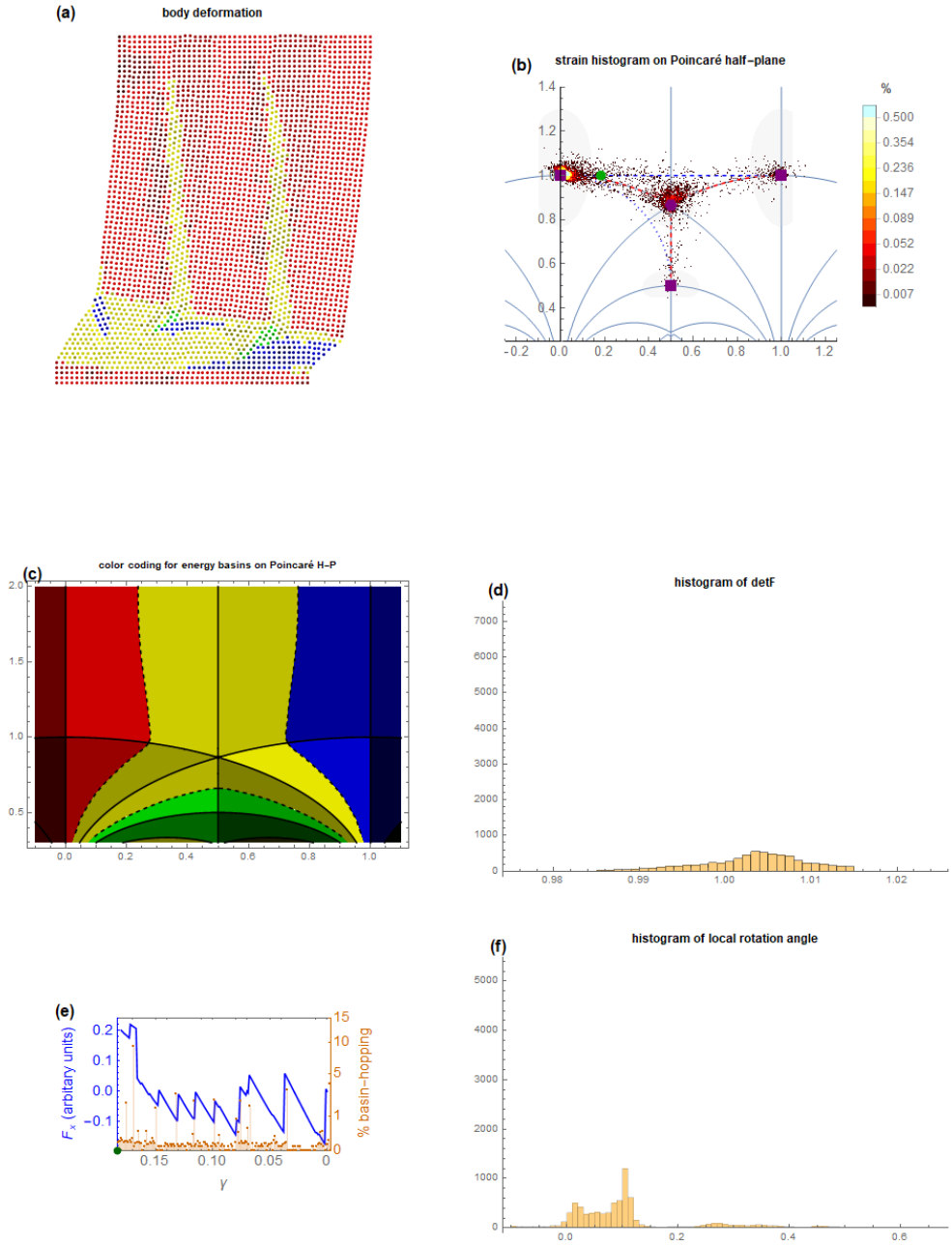

Figure 4.21: Results of the numerical simulation of plastic flow initiation of a square crystal with energy (4.46) when $\beta = 1$ and γ decreasing from 0.18 to 0: frame corresponding to $\gamma \simeq 0.18$

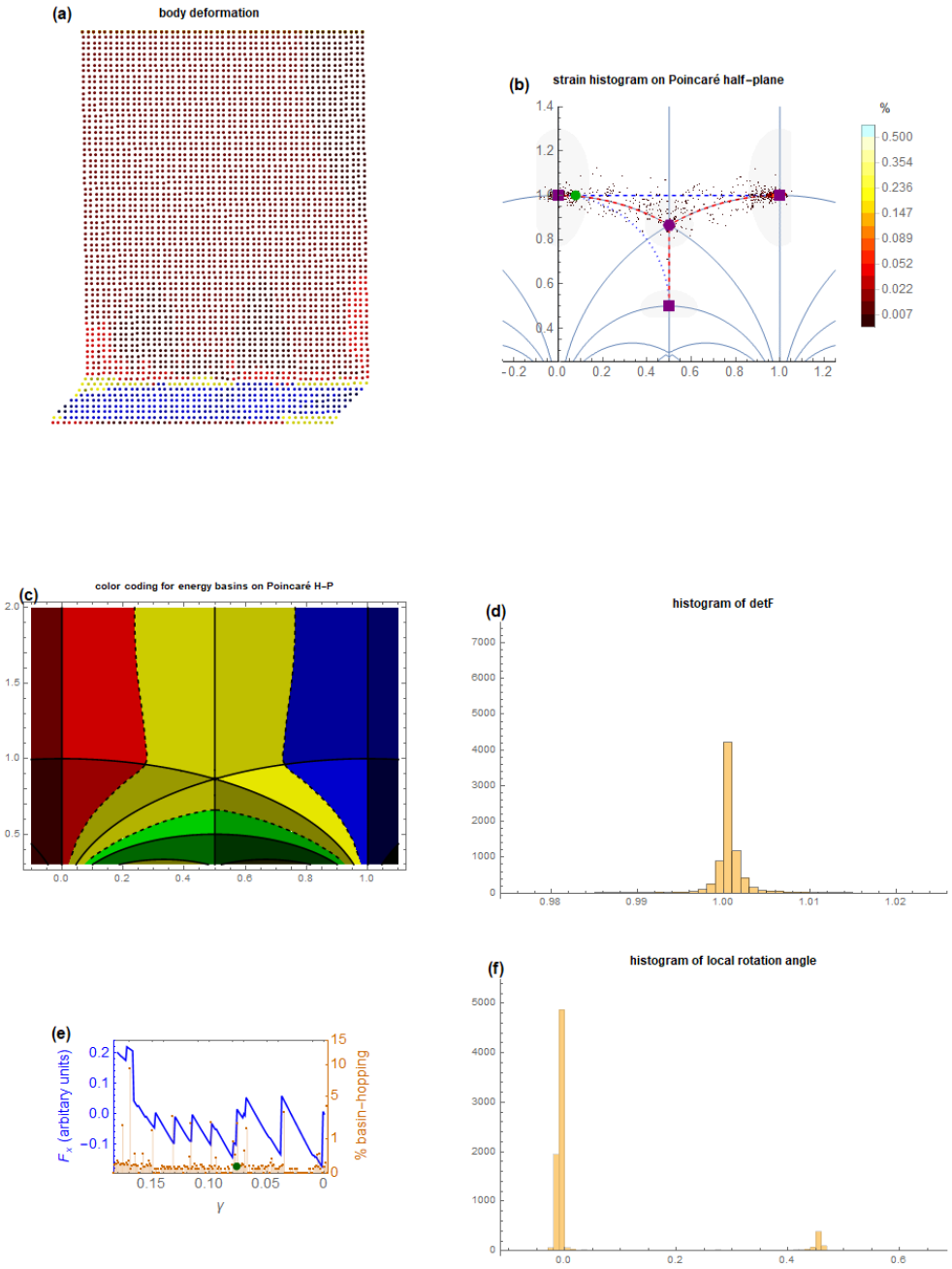

Figure 4.22: Results of the numerical simulation of plastic flow initiation of a square crystal with energy (4.46) when $\beta = 1$ and γ decreasing from 0.18 to 0: frame corresponding to $\gamma \simeq 0.08$

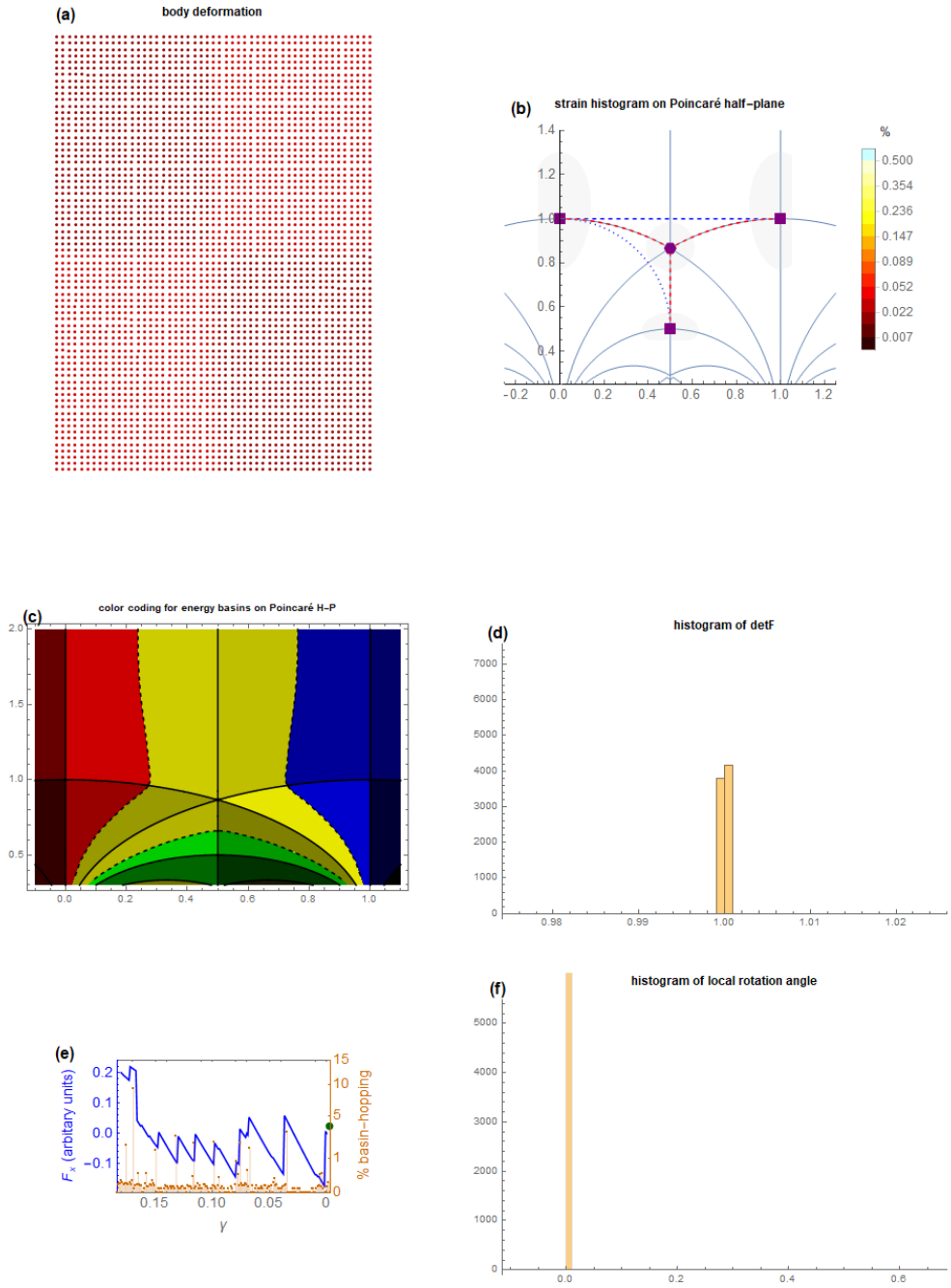

Figure 4.23: Results of the numerical simulation of plastic flow initiation of a square crystal with energy (4.46) when $\beta = 1$ and γ decreasing from 0.18 to 0: frame corresponding to $\gamma \simeq 0$

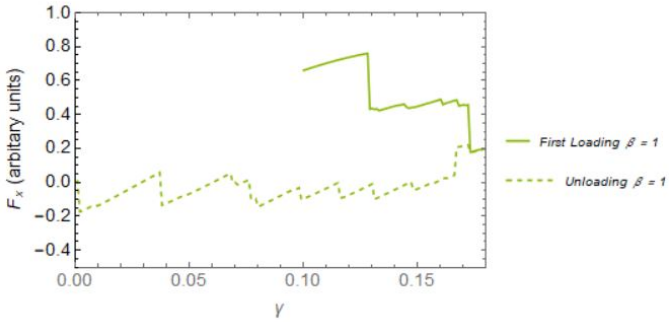

Figure 4.24: (Uncomplete) shear hysteresis for the case $\beta = 1$

Conclusions and Future Work

This work attemps to further demonstrate how the intuition originally conceived by Parry (1998) is remarkably fertile.
First, the transparent correspondance between the strain space and the Poincaré half-plane and then the possibility to draw from the classical theory of modular forms to build correctly-invariant strain energies for two-dimensional lattice allow to model not only phenomena related to crystal plasticity but also mechanically- or thermally-driven structural phase transformations in crystalline materials.
Structural phase transformations represent the core of this thesis as we have provided explicit strain energies both for reconstructive and weak (or symmetry-breaking) martensitic phase transformations.
The first model conceived suitably describes a square-to-hexagonal reconstructive transformation. After having explored the bifurcation patterns in the strain space generated by this model, the analysis proceeded towards the investigation of the energetically optimal barrier-crossing paths associated to plastic phenomena, whose description is also spontaneously contained in the model. The theoretical framework has been combined with the numerical analysis, through which it has been possible to prove the validity of the model when predicting relevant physical deformation processes.
The second model consists of a strain energy function able to describe a square-to-rhombic weak transformation. The reversibility characterizing this transformation leads to model both the shape-memory effect and superelasticity. The theoretical analysis of this second explicit expression has been rather involved as we have tried to present all the implications stemming from the choice of the values of the control parameters contained in the model.
As in the second case the theoretical framework has not been accompanied by a numerical validation, the first proposal for a future development becomes natural together with further future activities:

1. Numerical analysis of the model presented for martensitic phase tranformations of the weak type. This could lead to the direct observation of both the shape-memory effect when thermically driving the tranformation and superelasticity phenomena when mechanically driving it.

2. A more deepened analysis of the mechanisms leading to the generation of rich twinned microstructure of martensite during phase transformations.

3. The numerical implementation of a more effective algorithm able to identify gradient extremals and valley-ridge inflection points characterizing the energetic surfaces presented in the thesis.

4. The most important and most difficult development concerns the extension to the three-dimensional framework. It is the most important as it would allow to obtain direct applicable results, but concurrently it is very difficult to properly characterize modular forms so that they can reflect $GL(3, \mathbb{Z})$-invariance of three-dimensional crystalline lattices.

Bibliography

[1] M.Zanotti A. Ferrero F.Gazzola. *Elementi di Analisi Superiore per la Fisica e l'Ingegneria*. Esculapio, 2015.

[2] Tom M. Apostol. *Modular Functions and Dirichlet Series in Number theory*. Springer, 1976.

[3] Edoardo Arbib. *Parametri d'ordine modulari in elasticità non lineare*. MSc Thesis, 2016.

[4] Kaushik Bhattacharaya. *Microstructure of Martensite: Why it forms and it gives rise to the shape-memory effect*. Oxford University Press, 2004.

[5] Kaushik Bhattacharya et al. "Crystal Symmetry and the Reversibility of Martensitic Transformations". In: *Nature* 428 (May 2004). DOI: 10.1038/nature02378.

[6] Sergio Conti and Giovanni Zanzotto. "A Variational Model for Reconstructive Phase Transformations in Crystals, and their Relation to Dislocations and Plasticity". In: *Archive for Rational Mechanics and Analysis* 173.1 (July 2004), pp. 69–88. ISSN: 1432-0673. DOI: 10.1007/s00205-004-0311-z. URL: https://doi.org/10.1007/s00205-004-0311-z.

[7] Morton E. Gurtin. *An Introduction to Continuum Mechanics*. Academic Press, 1981.

[8] David K. Hoffman, Ross S. Nord, and Klaus Ruedenberg. "Gradient extremals". In: *Theoretica chimica acta* 69.4 (May 1986), pp. 265–279. ISSN: 1432-2234. DOI: 10.1007/BF00527704. URL: https://doi.org/10.1007/BF00527704.

[9] G. P. Parry. "Low-Dimensional Lattice Groups for the Continuum Mechanics of Phase Transitions in Crystals". In: *Archive for Rational Mechanics and Analysis* 145.1 (Nov. 1998), pp. 1–22. ISSN: 1432-0673. DOI: 10.1007/s002050050122. URL: https://doi.org/10.1007/s002050050122.

[10] Scott Peckham. "Monkey, Starfish and Octopus Saddles". In: 2011.

[11] M. Pitteri and G. Zanzotto. *Continuum Models for Phase Transitions and Twinning in Crystals*. Applied Mathematics. CRC Press, 2002. ISBN: 9781420036145. URL: https://books.google.it/books?id=u2JJCRt-oWYC.

[12] Wolfgang Quapp, Michael Hirsch, and Dietmar Heidrich. "An approach to reaction path branching using valley–ridge inflection points of potential-energy surfaces". In: *Theoretical Chemistry Accounts* 112.5 (Apr. 2004), pp. 40–51. DOI: 10.1007/s002140050389. URL: 10.1007/s00214-003-0558-8.

[13] Wolfgang Quapp, Michael Hirsch, and Dietmar Heidrich. "Bifurcation of reaction pathways: the set of valley ridge inflection points of a simple three-dimensional potential energy surface". In: *Theoretical Chemistry Accounts* 100.5 (Dec. 1998), pp. 285–299. ISSN: 1432-2234. DOI: 10.1007/s002140050389. URL: https://doi.org/10.1007/s002140050389.

[14] Alfio Quarteroni. *Modellistica Numerica per Problemi Differenziali*. 6th ed. Springer, 2016.

[15] Bruno Schoeneberg. *Elliptic Modular Functions: An Introduction*. Springer, 1974.

[16] Alex Shtyk, Garry Goldstein, and Claudio Chamon. "Electrons at the monkey saddle: A multicritical Lifshitz point". In: *Physical Review B* 95 (June 2016). DOI: 10.1103/PhysRevB.95.035137.

[17] Brigitte Vallée and Antonio Vera. "Probabilistic behaviour of lattice reduction algorithms". In: (Jan. 2010).

[18] Wikipedia. *Poincaré disk model*. 2013. URL: https://en.wikipedia.org/wiki/Poincar%C3%A9_disk_model.